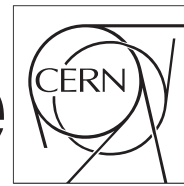


The Compact Muon Solenoid Experiment

# CMS Draft Note

Mailing address: CMS CERN, CH-1211 GENEVA 23, Switzerland



2016/03/03

Head Id: 329780

Archive Id: 329905M

Archive Date: 2016/03/02

Archive Tag: trunk

## Search for ttH in multilepton final states at 13 TeV

Anne-Catherine Le Bihan<sup>6</sup>, Benjamin Stieger<sup>4</sup>, Binghuan Li<sup>5</sup>, Charlie Mueller<sup>3</sup>, Cristina Botta<sup>1</sup>, Daniel Bloch<sup>6</sup>, Francesco Romeo<sup>5</sup>, Geoffrey Smith<sup>3</sup>, Giovanni Petrucciani<sup>1</sup>, Huaqiao Zhang<sup>5</sup>, Jan Steggemann<sup>1</sup>, Jeremy Andrea<sup>6</sup>, Kevin Lannon<sup>3</sup>, Kirill Skovpen<sup>6</sup>, Marco Peruzzi<sup>1</sup>, Milos Dordevic<sup>1</sup>, Nicolas Chanon<sup>6</sup>, Predrag Cirkovic<sup>2</sup>, Rami Kamalieddin<sup>4</sup>, Rebeca Gonzalez Suarez<sup>4</sup>, and Xavier Coubez<sup>6</sup>

<sup>1</sup> CERN<sup>2</sup> University of Belgrade<sup>3</sup> University of Notre Dame<sup>4</sup> University of Nebraska<sup>5</sup> IHEP<sup>6</sup> IPHC

### Abstract

A search for the standard model Higgs boson produced in association with a top quark pair is presented, using  $2.3 \text{ fb}^{-1}$  of 13 TeV pp collision data collected by the CMS experiment at the LHC. Final states with a Higgs boson that decays to either  $ZZ^*$ ,  $WW^*$ , or  $\tau\tau$  are required to have a top quark pair that decays to either lepton plus jets ( $t\bar{t} \rightarrow \ell\nu jj b\bar{b}$ ) or dileptons ( $t\bar{t} \rightarrow \ell\ell\nu\nu bb$ ), where  $\ell$  represents an electron or a muon. The following signatures are selected: two isolated same-sign leptons (electrons or muons) plus b-tagged jets, three isolated leptons plus b-tagged jets, or four isolated leptons plus b-tagged jets. The presence of an hadronic  $\tau$  reconstructed in the event is also considered in the event categorization. The expected 95% confidence level upper limit on the Higgs boson production cross section for a Higgs boson mass of 125 GeV/c<sup>2</sup> is 2.6 times the standard model expectation, compared to an observed limit of 3.5. The signal strength  $\mu$ , relative to the expectation for the standard model Higgs boson, is measured to be  $0.8^{+1.4}_{-1.2}$ .

This box is only visible in draft mode. Please make sure the values below make sense.

PDFAuthor: The ttH multilepton group  
PDFTitle: Search for ttH in multilepton final states at 13 TeV  
PDFSubject: CMS  
PDFKeywords: CMS, physics, higgs, top

Please also verify that the abstract does not use any user defined symbols

DRAFT

## 1 Contents

|    |     |  |    |
|----|-----|--|----|
| 2  | 1   | Introduction . . . . .   | 2  |
| 3  | 2   | Data and MC Samples . . . . .  | 4  |
| 4  | 2.1 | Data Samples . . . . .   | 4  |
| 5  | 2.2 | Signal Samples . . . . .   | 4  |
| 6  | 2.3 | Background Samples . . . . .   | 4  |
| 7  | 2.4 | Triggers . . . . .   | 8  |
| 8  | 2.5 | Trigger efficiency in data and simulation . . . . .                  | 8  |
| 9  | 3   | Event reconstruction and object identification . . . . .             | 12 |
| 10 | 3.1 | Jets and B-tagging . . . . .   | 12 |
| 11 | 3.2 | Missing Energy . . . . .   | 12 |
| 12 | 3.3 | Lepton Identification . . . . .                                      | 13 |
| 13 | 3.4 | Validation of lepton identification variables . . . . .              | 17 |
| 14 | 3.5 | Taus . . . . .   | 21 |
| 15 | 4   | Event selection . . . . .  | 23 |
| 16 | 4.1 | Two lepton same-sign category . . . . .                              | 23 |
| 17 | 4.2 | Three lepton category . . . . .                                      | 23 |
| 18 | 5   | Signal extraction . . . . .  | 30 |
| 19 | 5.1 | Event subcategories . . . . .  | 33 |
| 20 | 6   | Signal modeling . . . . .  | 39 |
| 21 | 6.1 | Correction factors and experimental uncertainties . . . . .          | 39 |
| 22 | 6.2 | Theoretical uncertainties . . . . .                                  | 40 |
| 23 | 7   | Background predictions . . . . .                                     | 41 |
| 24 | 7.1 | Irreducible backgrounds . . . . .                                    | 41 |
| 25 | 7.2 | Di-bosons backgrounds . . . . .                                      | 43 |
| 26 | 7.3 | Charge misassignment background . . . . .                            | 47 |
| 27 | 7.4 | Fake lepton background . . . . .                                     | 51 |
| 28 | 8   | Results . . . . .  | 62 |
| 29 | A   | Control region plots . . . . .                                       | 65 |
| 30 | A.1 | Lepton MVA sideband region . . . . .                                 | 65 |
| 31 | A.2 | Jet multiplicity sideband region . . . . .                           | 68 |
| 32 | A.3 | $t\bar{t} \rightarrow e^\pm \mu^\mp b\bar{b} \nu\bar{\nu}$ . . . . . | 71 |
| 33 | A.4 | $WZ \rightarrow 3\ell$ . . . . .                                     | 72 |
| 34 | A.5 | $t\bar{t}Z \rightarrow 3\ell$ . . . . .                              | 73 |
| 35 | B   | Post-fit distributions . . . . .                                     | 75 |
| 36 | C   | Cross checks on the fit . . . . .                                    | 81 |
| 37 | C.1 | Alternative fit: separately for 2lss and 3l . . . . .                | 81 |

## 38 1 Introduction

39 The LHC Run I data have been exploited to measure all the accessible properties of the newly-  
 40 discovered Higgs boson [1, 2]. ATLAS and CMS have combined their effort in order to reach  
 41 an already very precise measurement of the boson mass,  $125.09 \pm 0.21$  (stat.)  $\pm 0.11$  (syst.)  
 42 GeV [3]. This precise mass result has created an opportunity to test the predictions of the stan-  
 43 dard model by measuring the other properties of the Higgs boson. Measurements of the Higgs  
 44 boson production and decay rates and constraints on its couplings have been performed by  
 45 both experiments [4, 5], and in general agreement with the SM predictions given the current  
 46 uncertainties (10-30 %) have been found. It is of course of great interest to use the 13 TeV LHC  
 47 data to further constrain these measurements as any deviation from expectation could be a sign  
 48 of new physics.

49

50 Among these measurements, it is of particular interest to measure the coupling of the Higgs  
 51 boson to the top quark ( $t\bar{t}H$ ) because the top quark could play a special role in the context  
 52 of electroweak symmetry breaking due to its large mass. The Higgs boson does not decay to  
 53 top quarks. The  $t\bar{t}H$  interaction vertex, however, is present in a rare production mechanism  
 54 where the Higgs boson is produced in association with a top quark-antiquark pair as shown  
 55 in Fig. 1. At LHC energies the largest contribution to standard model Higgs boson production  
 56 is a gluon-gluon induced loop dominated by virtual top exchange. The comparison of a direct  
 57 measurement of the  $t\bar{t}H$  coupling with the one inferred from the cross section measurement  
 58 can put limits on the contribution of new physics to the gluon-gluon loop.

59

60 The  $t\bar{t}H$  process has been used by both experiments to directly measure the top-Higgs coupling  
 61 at tree level with the  $20 \text{ fb}^{-1}$  of 8 TeV collisions of LHC Run I. Via this process both experiments  
 62 reached a 30% accuracy on the top Yukawa coupling, a great achievement given that the pro-  
 63 duction cross section (130 fb at 8 TeV at next-to-leading order (NLO) [6]) was two orders of  
 64 magnitude lower with respect to the dominant Higgs production mode (gluon-gluon fusion).  
 65 In order to achieve this result several decay channels of the Higgs boson have been considered  
 66 by both experiments, and three main searches have been designed by both experiments. The  
 67 first channel searches for  $t\bar{t}H$  in events where the Higgs boson decays to  $b\bar{b}$ ; the best fit value  
 68 for the combined signal strength obtained by the CMS experiment is  $0.7^{+1.9}_{-1.9}$  (95% CL)) [7].  
 69 The second channel searches for  $t\bar{t}H$  in events where the Higgs boson decays to  $\gamma\gamma$ ; the best fit  
 70 value for the combined signal strength obtained by the CMS experiment is  $2.7^{+2.6}_{-1.8}$  (95% CL)) [7].

71

72 We designed the third search to probe  $t\bar{t}H$  events where the Higgs boson decays into  $ZZ^*$ ,  
 73  $WW^*$ , or  $\tau\tau$ , with at least one Z, W or  $\tau$  decaying leptonically. Despite the small branching  
 74 ratio, the presence of one or two additional leptons from the top quark pair decays leads to the  
 75 following clean experimental signatures:

- 76 • two same-sign leptons (electrons or muons) plus b-tagged jets;
- 77 • three leptons plus b-tagged jets;
- 78 • four leptons plus b-tagged jets.

79 Examples of Feynman diagrams for  $t\bar{t}H$ , followed by the decays of the top quark and the Higgs  
 80 boson that lead to the signatures described above are shown in Fig. 1. With this search we ob-  
 81 tained the most precise measurement of the  $t\bar{t}H$  signal strength:  $3.7^{+1.9}_{-1.9}$  (95%CL)) [8].

82

83 The combined best-fit signal strength obtained assuming a Higgs boson mass of 125 GeV was  
 84  $\mu = 2.9^{+1.1}_{-0.9}$ . This result corresponds to a 3.5 standard deviation excess over the background-  
 85 only ( $\mu = 0$ ) hypothesis, and represents a 2.1 standard deviation upward fluctuation on the SM  
 86  $t\bar{t}H$  ( $\mu = 1$ ) expectation. Although the combined observed signal strength is consistent with  
 87 SM expectations, with a roughly 2 standard deviation upward fluctuation, it is interesting to  
 88 point out that the excess was mainly driven by the multilepton analysis, and in particular by  
 89 the same-sign di-muon subsample [8].

90

91 In this note we repeat the multilepton search with the first  $2.3 \text{ fb}^{-1}$  of 13 TeV data collected by  
 92 the CMS experiment during the 2015 LHC Run II. The  $t\bar{t}H$  cross section increases by a factor  
 93 4 with the higher center of mass energy. The cross sections of the main backgrounds  $t\bar{t}W$ ,  $t\bar{t}Z$ ,  
 94  $t\bar{t}+\text{jets}$  increase by roughly a factor 3. Thus, in this analysis we may achieve sensitivity not too  
 95 different from what was obtained in Run I.

96

97 The general strategy remains similar to the 8 TeV search. Multivariate analysis techniques are  
 98 used to identify objects with high purity and to distinguish background from signal events.  
 99 The amount of signal is fit to the multivariate discriminant output distribution in all the final  
 100 states simultaneously.

101

102 Several aspects of the analysis have been updated. The object selections have been adapted to  
 103 the 13 TeV running conditions, the dedicated lepton identification technique has been further  
 104 improved, new event kinematic variables have been considered in the multivariate approach  
 105 for the signal extraction, and the presence of hadronically-decaying  $\tau$  leptons has also been  
 106 considered in the event categorization.

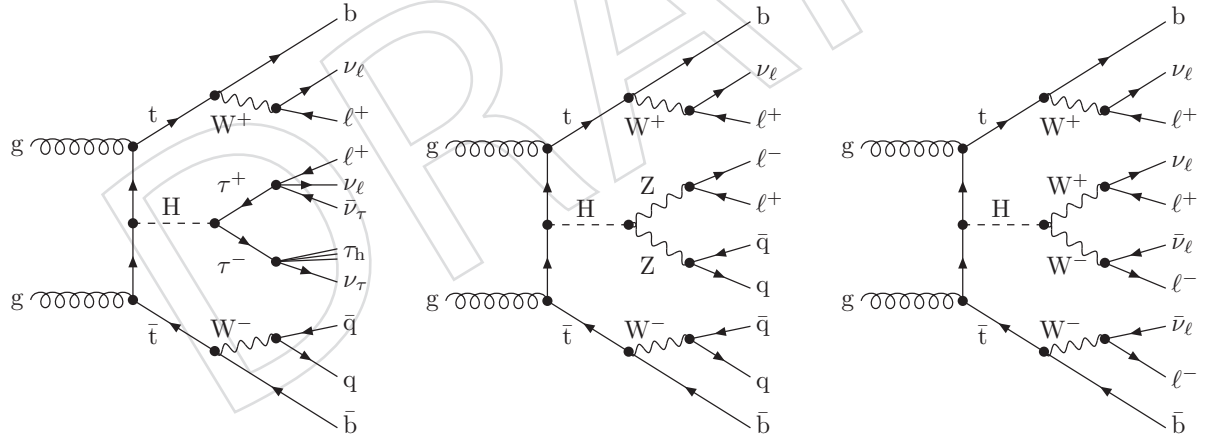


Figure 1: Example leading order Feynman diagrams for  $t\bar{t}H$  production at pp colliders, with the Higgs boson decaying to  $\tau\tau$ ,  $ZZ^*$  and  $WW^*$  (from left to right). The first, second, and third diagrams are examples of the two same-sign lepton signature, the three lepton signature, and the four lepton signature, respectively.

## 107 2 Data and MC Samples

108 In the following we list as reference the set of samples of the RunIISpring15MiniAODv2 (CMSSW  
 109 74X) campaign used for the studies and results presented in this version of the note, as well as  
 110 the one of the RunIIFall15MiniAODv2 (CMSSW 76X) campaign that we will use in the next  
 111 updates.

### 112 2.1 Data Samples

113 The data used in this analysis was collected with the CMS detector in 2015. We use data col-  
 114 lected only during periods when the CMS magnet was on, corresponding to a total integrated  
 115 luminosity of  $2.26 \text{ fb}^{-1}$  [9]. Details on the various datasets contributing to our analysis are  
 116 given in table 1 and table 2.

| Dataset  | Run Range       | Int. Lumi ( $\text{fb}^{-1}$ ) |
|--|-----------------|--------------------------------|
| /DoubleMuon/Run2015C_25ns-05Oct2015-v1/MINIAOD     | 254227 - 254914 | 0.02                           |
| /DoubleMuon/Run2015D-05Oct2015-v1/MINIAOD          | 256630 - 260627 | 2.24                           |
| /DoubleMuon/Run2015D-PromptReco-v4/MINIAOD         |                 | 2.26                           |
| Total DoubleMuon                                   |                 | 2.26                           |
| /DoubleEG/Run2015C_25ns-05Oct2015-v1/MINIAOD       | 254227 - 254914 | 0.02                           |
| /DoubleEG/Run2015D-05Oct2015-v1/MINIAOD            | 256630 - 260627 | 2.24                           |
| /DoubleEG/Run2015D-PromptReco-v4/MINIAOD           |                 | 2.26                           |
| Total DoubleEG                                     |                 | 2.26                           |
| /MuonEG/Run2015C_25ns-05Oct2015-v1/MINIAOD         | 254227 - 254914 | 0.02                           |
| /MuonEG/Run2015D-05Oct2015-v1/MINIAOD              | 256630 - 260627 | 2.24                           |
| /MuonEG/Run2015D-PromptReco-v4/MINIAOD             |                 | 2.26                           |
| Total MuonEG                                       |                 | 2.26                           |
| /SingleMuon/Run2015C_25ns-05Oct2015-v1/MINIAOD     | 254227 - 254914 | 0.02                           |
| /SingleMuon/Run2015D-05Oct2015-v1/MINIAOD          | 256630 - 260627 | 2.24                           |
| /SingleMuon/Run2015D-PromptReco-v4/MINIAOD         |                 | 2.26                           |
| Total SingleMuon                                   |                 | 2.26                           |
| /SingleElectron/Run2015C_25ns-05Oct2015-v1/MINIAOD | 254227 - 254914 | 0.02                           |
| /SingleElectron/Run2015D-05Oct2015-v1/MINIAOD      | 256630 - 260627 | 2.24                           |
| /SingleElectron/Run2015D-PromptReco-v4/MINIAOD     |                 | 2.26                           |
| Total SingleElectron                               |                 | 2.26                           |

Table 1: The datasets used in this analysis (CMSSW 74X), with corresponding run ranges and integrated luminosities. Luminosities listed here are derived using the brilcalc tool [10].

### 117 2.2 Signal Samples

118 We use simulated Monte-Carlo events to model both the ttH signal and the various standard  
 119 model backgrounds. The ttH events are simulated at next-to-leading-order (NLO) accuracy  
 120 using aMC@NLO [11], and matched to PYTHIA [12] for the parton shower. An additional  
 121 POWHEG [13] ttH sample provides more statistics when training boosted descision trees dur-  
 122 ing the signal extraction phase, but is not used in computing the final result of the analysis.  
 123 More details on the samples and the NLO cross section are reported in Table 3 and Table 4. We  
 124 have also used additional Higgs signal samples to check that the overlap with the ttH event  
 125 selection can be considered negligible at this stage; these are listed in Table 5 and Table 6.

### 126 2.3 Background Samples

127 In this section, we list the Monte-Carlo samples used to model our backgrounds. A variety of  
 128 methods are used to produce these samples: for our dominant backgrounds (ttbar, ttW, ttZ), we

| Dataset  | Run Range       | Int. Lumi (fb <sup>-1</sup> ) |
|--|-----------------|-------------------------------|
| /DoubleMuon/Run2015C_25ns-16Dec2015-v1/MINIAOD     | 254227 - 254914 | 0.02                          |
| /DoubleMuon/Run2015D-16Dec2015-v1/MINIAOD          | 256630 - 260627 | 2.24                          |
| Total DoubleMuon                                   |                 | 2.26                          |
| /DoubleEG/Run2015C_25ns-16Dec2015-v1/MINIAOD       | 254227 - 254914 | 0.02                          |
| /DoubleEG/Run2015D-04Dec2015-v2/MINIAOD            | 256630 - 260627 | 2.24                          |
| Total DoubleEG                                     |                 | 2.26                          |
| /MuonEG/Run2015C_25ns-16Dec2015-v1/MINIAOD         | 254227 - 254914 | 0.02                          |
| /MuonEG/Run2015D-16Dec2015-v1/MINIAOD              | 256630 - 260627 | 2.24                          |
| Total MuonEG                                       |                 | 2.26                          |
| /SingleMuon/Run2015C_25ns-16Dec2015-v1/MINIAOD     | 254227 - 254914 | 0.02                          |
| /SingleMuon/Run2015D-16Dec2015-v1/MINIAOD          | 256630 - 260627 | 2.24                          |
| Total SingleMuon                                   |                 | 2.26                          |
| /SingleElectron/Run2015C_25ns-16Dec2015-v1/MINIAOD | 254227 - 254914 | 0.02                          |
| /SingleElectron/Run2015D-04Dec2015-v2/MINIAOD      | 256630 - 260627 | 2.24                          |
| Total SingleElectron                               |                 | 2.26                          |

Table 2: The datasets used in this analysis (CMSSW 76X), with corresponding run ranges and integrated luminosities. Luminosities listed here are derived using the brilcalc tool [10].

| Sample   | Xsec (pb) |
|--|-----------|
| /tHJjetToNonbb_M120_13TeV_amcatnloFXFX_madspin_pythia8_mWCutfix/RunIISpring15MiniAODv2-74X_mcRun2_asymptotic_v2-v1/MINIAODSIM      |           |
| /tHJjetToNonbb_M120_13TeV_amcatnloFXFX_madspin_pythia8_mWCutfix/RunIISpring15MiniAODv2-74X_mcRun2_asymptotic_v2_ext1-v1/MINIAODSIM |           |
| /tHJjetToNonbb_M125_13TeV_amcatnloFXFX_madspin_pythia8_mWCutfix/RunIISpring15MiniAODv2-74X_mcRun2_asymptotic_v2-v1/MINIAODSIM      | 0.2586    |
| /tHJjetToNonbb_M125_13TeV_amcatnloFXFX_madspin_pythia8_mWCutfix/RunIISpring15MiniAODv2-74X_mcRun2_asymptotic_v2_ext1-v1/MINIAODSIM | 0.2586    |
| /tHJjetToNonbb_M130_13TeV_amcatnloFXFX_madspin_pythia8_mWCutfix/RunIISpring15MiniAODv2-74X_mcRun2_asymptotic_v2-v1/MINIAODSIM      |           |
| /tHJjetToNonbb_M130_13TeV_amcatnloFXFX_madspin_pythia8_mWCutfix/RunIISpring15MiniAODv2-74X_mcRun2_asymptotic_v2_ext1-v1/MINIAODSIM |           |
| /tHToNonbb_M125_13TeV_powheg_pythia8_RunIIISpring15MiniAODv2-74X_mcRun2_asymptotic_v2-v2/MINIAODSIM                                | 0.2586    |

Table 3: Signal samples used in this analysis (CMSSW 74X).

use the same aMC@NLO→PYTHIA chain used for the ttH signal and the NLO cross sections.  
Other minor backgrounds may use other generators, such as PYTHIA or POWHEG matched to PYTHIA. See tables 7 and 8 for more details.

132

In the context of the RunIIFall15MiniAODv2 (CMSSW 76X) campaign we privately produced ttW and ttZ inclusive leading-order MadGraph samples with up to two extra partons for ttW or one extra for ttZ. Moreover, since the nominal ttZ MC sample is generated with the requirement  $m_{\ell^+\ell^-} > 10 \text{ GeV}$ , we also use LO Madgraph to generate the remaining part of the phase space ( $1 < m_{\ell^+\ell^-} < 10 \text{ GeV}$ ). This private sample was produced both in the context of the RunIIFall15MiniAODv2 (CMSSW 76X) and RunIISpring15MiniAODv2 (CMSSW 74X) campaigns. Another sample not yet available both campaigns is the t̄WW. Nevertheless in RunI analysis we proved that in all the analysed final states, the contribution of the process is found to be at least an order of magnitude smaller than t̄W and t̄Z.

133

134

135

136

137

138

139

140

141

| Sample  | Xsec (pb) |
|---|-----------|
| /tHJetToNonbb_M120_13TeV_amcatnloFXFX_madspin_pythia8_mcWCutfix/RunIIFall15MiniAODv2-PU25nsData2015v1_76X_mcRun2_asymptotic_v12-v2/MINIAODSIM |           |
| /tHJetToNonbb_M125_13TeV_amcatnloFXFX_madspin_pythia8_mcWCutfix/RunIIFall15MiniAODv2-PU25nsData2015v1_76X_mcRun2_asymptotic_v12-v1/MINIAODSIM | 0.2586    |
| /tHJetToNonbb_M130_13TeV_amcatnloFXFX_madspin_pythia8_mcWCutfix/RunIIFall15MiniAODv2-PU25nsData2015v1_76X_mcRun2_asymptotic_v12-v1/MINIAODSIM | 0.01561   |
| /tHToNonbb_M125_13TeV_powheg_pythia8/RunIIFall15MiniAODv2-PU25nsData2015v1_76X_mcRun2_asymptotic_v12-v1/MINIAODSIM                            | 0.2586    |

Table 4: Signal samples used in this analysis (CMSSW 76X).

| Sample  | Xsec (pb) |
|---|-----------|
| /THQ_Hincl_13TeV-madgraph-pythia8_TuneCUETP8M1/RunIISpring15MiniAODv2-74X_mcRun2_asymptotic_v2-v1/MINIAODSIM    | 0.07096   |
| /THW_Hincl_13TeV-madgraph-pythia8_TuneCUETP8M1/RunIISpring15MiniAODv2-74X_mcRun2_asymptotic_v2-v1/MINIAODSIM    | 0.01561   |
| /GluGluHToZZTo4L_M125_13TeV_powheg_JHUGen_pythia8/RunIISpring15MiniAODv2-74X_mcRun2_asymptotic_v2-v1/MINIAODSIM | 0.01191   |

Table 5: Additional signal samples that have potential overlap with the ttH event selection (CMSSW 74X).

| Sample  | Xsec (pb) |
|---|-----------|
| THQ (not yet available)   |           |
| /THW_Hincl_13TeV-madgraph-pythia8_TuneCUETP8M1/RunIIFall15MiniAODv2-PU25nsData2015v1_76X_mcRun2_asymptotic_v2-v1/MINIAODSIM | 0.07096   |
| /GluGluHToZZTo4L_M125_13TeV_powheg_JHUGenV6_pythia8/RunIIFall15MiniAODv2-74X_mcRun2_asymptotic_v2-v1/MINIAODSIM             | 0.01191   |

Table 6: Additional signal samples that have potential overlap with ttH event selection (CMSSW 76X).

| Sample  | Xsec (pb) |
|---|-----------|
| /TTWJetsToLNu_TuneCUETP8M1_13TeV-amcatnloFXFX-madspin-pythia8_RunIISpring15MiniAODv2-74X_mcRun2_asymptotic_v2-v1/MINIAODSIM           | 0.2043    |
| /TTZToLLNuNu_M-10_TuneCUETP8M1_13TeV-amcatnlo_pythia8_RunIISpring15MiniAODv2-74X_mcRun2_asymptotic_v2-v1/MINIAODSIM                   | 0.2529    |
| /store/cmst3/group/susy/gpetrucc/13TeV/RunIISpring15MiniAODv2/TTLJjets_m1to10_LO_NoMS/  | 0.0283    |
| /TTGJets_TuneCUETP8M1_13TeV-amcatnloFXFX-madspin-pythia8_RunIISpring15MiniAODv2-74X_mcRun2_asymptotic_v2-v1/MINIAODSIM                | 3.697     |
| /WGTtoLNuG_TuneCUETP8M1_13TeV-madgraphMLM-pythia8_RunIISpring15MiniAODv2-74X_mcRun2_asymptotic_v2-v1/MINIAODSIM                       | 585.8     |
| /ZGTo2LG_TuneCUETP8M1_13TeV-amcatnloFXFX_pythia8_RunIISpring15MiniAODv2-74X_mcRun2_asymptotic_v2-v1/MINIAODSIM                        | 131.3     |
| /TGJets_TuneCUETP8M1_13TeV_amcatnlo_madspin_pythia8_RunIISpring15MiniAODv2-74X_mcRun2_asymptotic_v2-v1/MINIAODSIM                     | 2.967     |
| /WpWpJJ_EWK-QCD_TuneCUETP8M1_13TeV-madgraph-pythia8_RunIISpring15MiniAODv2-74X_mcRun2_asymptotic_v2-v1/MINIAODSIM                     | 0.03711   |
| Rares /ZZZ_TuneCUETP8M1_13TeV-amcatnlo_pythia8_RunIISpring15MiniAODv2-74X_mcRun2_asymptotic_v2-v1/MINIAODSIM                          | 0.01398   |
| Rares /WZZ_TuneCUETP8M1_13TeV-amcatnlo_pythia8_RunIISpring15MiniAODv2-74X_mcRun2_asymptotic_v2-v1/MINIAODSIM                          | 0.05565   |
| Rares /WWZ_TuneCUETP8M1_13TeV-amcatnlo_pythia8_RunIISpring15MiniAODv2-74X_mcRun2_asymptotic_v2-v1/MINIAODSIM                          | 0.1651    |
| Rares /WW_DoubleScattering_13TeV_pythia8_RunIISpring15MiniAODv2-74X_mcRun2_asymptotic_v2-v1/MINIAODSIM                                | 1.64      |
| Rares /Zq_ll_4f_13TeV-amcatnlo_pythia8_TuneCUETP8M1_RunIISpring15MiniAODv2-74X_mcRun2_asymptotic_v2-v1/MINIAODSIM                     | 0.0758    |
| Rares /TTT_TuneCUETP8M1_13TeV-amcatnlo_pythia8_RunIISpring15MiniAODv2-74X_mcRun2_asymptotic_v2-v1/MINIAODSIM                          | 0.009103  |
| Rares /TTT_TuneCUETP8M1_13TeV-amcatnlo_pythia8_RunIISpring15MiniAODv2-74X_mcRun2_asymptotic_v2-ext1-v1/MINIAODSIM                     | 0.009103  |
| /TTJets_TuneCUETP8M1_13TeV-amcatnloFXFX_pythia8_RunIISpring15MiniAODv2-74X_mcRun2_asymptotic_v2-v1/MINIAODSIM                         | 832       |
| /DYJetsToLL_M-10to50_TuneCUETP8M1_13TeV-amcatnloFXFX_pythia8_RunIISpring15MiniAODv2-74X_mcRun2_asymptotic_v2-v1/MINIAODSIM            | 18610     |
| /DYJetsToLL_M-50_TuneCUETP8M1_13TeV-amcatnloFXFX_pythia8_RunIISpring15MiniAODv2-74X_mcRun2_asymptotic_v2-v3/MINIAODSIM                | 6025.2    |
| /WJetsToLNu_TuneCUETP8M1_13TeV-amcatnloFXFX_pythia8_RunIISpring15MiniAODv2-74X_mcRun2_asymptotic_v2-v1/MINIAODSIM                     | 61526.7   |
| /ZZTo4L_13TeV_powheg_pythia8_RunIISpring15MiniAODv2-74X_mcRun2_asymptotic_v2-v1/MINIAODSIM  | 1.256     |
| /WZTo3LNu_TuneCUETP8M1_13TeV-powheg_pythia8_RunIISpring15MiniAODv2-74X_mcRun2_asymptotic_v2-v1/MINIAODSIM                             | 4.102     |
| /WWTo2L2Nu_13TeV-powheg_RunIISpring15MiniAODv2-74X_mcRun2_asymptotic_v2-v1/MINIAODSIM   | 10.481    |
| /ST_tW_top_5f_inclusiveDecays_13TeV-powheg_pythia8_TuneCUETP8M1_RunIISpring15MiniAODv2-74X_mcRun2_asymptotic_v2-v2/MINIAODSIM         | 35.6      |
| /ST_tW_antitop_5f_inclusiveDecays_13TeV-powheg_pythia8_TuneCUETP8M1_RunIISpring15MiniAODv2-74X_mcRun2_asymptotic_v2-v1/MINIAODSIM     | 35.6      |
| /ST_t-channel_4f_leptonDecays_13TeV-amcatnlo_pythia8_TuneCUETP8M1_RunIISpring15MiniAODv2-74X_mcRun2_asymptotic_v2-v1/MINIAODSIM       | 70.69     |
| /ST_t-channel_antitop_4f_leptonDecays_13TeV-powheg_pythia8_TuneCUETP8M1_RunIISpring15MiniAODv2-74X_mcRun2_asymptotic_v2-v1/MINIAODSIM | 26.71     |
| /ST_s-channel_4f_leptonDecays_13TeV-amcatnlo_pythia8_TuneCUETP8M1_RunIISpring15MiniAODv2-74X_mcRun2_asymptotic_v2-v1/MINIAODSIM       | 3.75      |

Table 7: List of background samples used in this analysis (CMSSW 74X). In the first section of the table are listed the samples of the processes for which we use the simulation to extract the final yields and shapes, in the second section the samples of the processes we will estimate from data. The MC simulation is used to design the data driven methods and derive the associated systematics.

| Sample   | Xsec (pb) |
|--|-----------|
| /TTWJetsToLNu.TuneCUETP8M1.13TeV-amcatnloFXFX-madspin-pythia8/RunIIFall15MiniAOdv2-PU25nsData2015v1.76X.mcRun2_asymptotic.v12-v1/MINIAODSIM          | 0.2043    |
| Additional privately-produced Madgraph LO ttW  | 0.2043    |
| ttZin10 (not yet available)  | 0.2529    |
| Additional privately-produced Madgraph LO ttZ  | 0.2529    |
| /store/cmst3/group/susy/gpeterucci/13TeV/RunIIFall15MiniAOdv2/TTLL_m1to10_LO_NoMS_for76X/  | 0.0283    |
| /WGToLNuG_TuneCUETP8M1_13TeV-madgraphMLM-pythia8/RunIIFall15MiniAOdv2-PU25nsData2015v1.76X.mcRun2_asymptotic.v12-v1/MINIAODSIM                       | 585.8     |
| /ZGTo2L_G_TuneCUETP8M1_13TeV-amcatnloFXFX-pythia8/RunIIFall15MiniAOdv2-PU25nsData2015v1.76X.mcRun2_asymptotic.v12-v1/MINIAODSIM                      | 131.3     |
| /TGGjets_TuneCUETP8M1_13TeV-amcatnlo_madspin_pythia8/RunIIFall15MiniAOdv2-PU25nsData2015v1.76X.mcRun2_asymptotic.v12-v1/MINIAODSIM                   | 2.967     |
| /TTGJets_TuneCUETP8M1_13TeV-amcatnloFXFX-madspin-pythia8/RunIIFall15MiniAOdv2-PU25nsData2015v1.76X.mcRun2_asymptotic.v12-v1/MINIAODSIM               | 3.697     |
| /WpWpj_EWK_QCD_TuneCUETP8M1_13TeV-madgraph-pythia8/RunIIFall15MiniAOdv2-PU25nsData2015v1.76X.mcRun2_asymptotic.v12-v1/MINIAODSIM                     | 0.03711   |
| Rares_ZZZ (not yet available)  |           |
| Rares_WWZ (not yet available)  |           |
| Rares_WZZ_TuneCUETP8M1_13TeV-amcatnlo_pythia8/RunIIFall15MiniAOdv2-PU25nsData2015v1.76X.mcRun2_asymptotic.v12-v1/MINIAODSIM                          | 0.05565   |
| Rares_WW_DoubleScattering_13TeV_pythia8_RunIIFall15MiniAOdv2-PU25nsData2015v1.76X.mcRun2_asymptotic.v12-v1/MINIAODSIM                                | 1.64      |
| Rares_tZq_ll_Af_13TeV_amcatnlo_pythia8_TuneCUETP8M1_RunIIFall15MiniAOdv2-PU25nsData2015v1.76X.mcRun2_asymptotic.v12-v1/MINIAODSIM                    | 0.0758    |
| Rares_TTTT_TuneCUETP8M1_13TeV-amcatnlo_pythia8_RunIIFall15MiniAOdv2-PU25nsData2015v1.76X.mcRun2_asymptotic.v12-v1/MINIAODSIM                         | 0.009103  |
| Rares_TTTT_TuneCUETP8M1_13TeV-amcatnlo_pythia8_RunIIFall15MiniAOdv2-PU25nsData2015v1.76X.mcRun2_asymptotic.v12_ext1-v1/MINIAODSIM                    | 0.009103  |
| /TTJets_SingleLeptFromTau_TuneCUETP8M1_13TeV-madgraphMLM_pythia8_RunIIFall15MiniAOdv2-PU25nsData2015v1.76X.mcRun2_asymptotic.v12-v1/MINIAODSIM       | 182       |
| /TTJets_SingleLeptFromT_TuneCUETP8M1_13TeV-madgraphMLM_pythia8_RunIIFall15MiniAOdv2-PU25nsData2015v1.76X.mcRun2_asymptotic.v12-v1/MINIAODSIM         | 182       |
| /TTJets_DisLept_TuneCUETP8M1_13TeV-madgraphMLM_pythia8_RunIIFall15MiniAOdv2-PU25nsData2015v1.76X.mcRun2_asymptotic.v12-v1/MINIAODSIM                 | 87.3      |
| /DYJetsToLL_M-10to50_TuneCUETP8M1_13TeV-amcatnloFXFX_pythia8_RunIIFall15MiniAOdv2-PU25nsData2015v1.76X.mcRun2_asymptotic.v12-v1/MINIAODSIM           | 18610     |
| /DYJetsToLL_M-50_TuneCUETP8M1_13TeV-madgraphMLM_pythia8_RunIIFall15MiniAOdv2-PU25nsData2015v1.76X.mcRun2_asymptotic.v12-v1/MINIAODSIM                | 6025.2    |
| /WJetsToLNu_TuneCUETP8M1_13TeV-amcatnloFXFX_pythia8_RunIIFall15MiniAOdv2-PU25nsData2015v1.76X.mcRun2_asymptotic.v12-v1/MINIAODSIM                    | 61526.7   |
| /ST_FW_top_5f_inclusiveDecays_13TeV_powheg_pythia8_TuneCUETP8M1_RunIIFall15MiniAOdv2-PU25nsData2015v1.76X.mcRun2_asymptotic.v12-v1/MINIAODSIM        | 35.6      |
| /ST_FW_antitop_5f_inclusiveDecays_13TeV_powheg_pythia8_TuneCUETP8M1_RunIIFall15MiniAOdv2-PU25nsData2015v1.76X.mcRun2_asymptotic.v12-v1/MINIAODSIM    | 35.6      |
| /ST_t-channel_4f_leptonDecays_13TeV_amcatnlo_pythia8_TuneCUETP8M1_RunIIFall15MiniAOdv2-PU25nsData2015v1.76X.mcRun2_asymptotic.v12-v1/MINIAODSIM      | 70.69     |
| /ST_t-channel_4f_leptonDecays_13TeV_amcatnlo_pythia8_TuneCUETP8M1_RunIIFall15MiniAOdv2-PU25nsData2015v1.76X.mcRun2_asymptotic.v12_ext1-v1/MINIAODSIM | 70.69     |
| ST_t-channel_antitop (not yet available)   |           |
| /ST_s-channel_4f_leptonDecays_13TeV_amcatnlo_pythia8_TuneCUETP8M1_RunIIFall15MiniAOdv2-PU25nsData2015v1.76X.mcRun2_asymptotic.v12-v2/MINIAODSIM      | 3.75      |
| /WZTo3LNu_TuneCUETP8M1_13TeV-powheg_pythia8_RunIIFall15MiniAOdv2-PU25nsData2015v1.76X.mcRun2_asymptotic.v12-v1/MINIAODSIM                            | 4.102     |
| /WWTo2L2Nu_13TeV-powheg_RunIIFall15MiniAOdv2-PU25nsData2015v1.76X.mcRun2_asymptotic.v12-v1/MINIAODSIM  | 10.481    |
| /ZZTo4L_13TeV_powheg_pythia8_RunIIFall15MiniAOdv2-PU25nsData2015v1.76X.mcRun2_asymptotic.v12-v1/MINIAODSIM   | 1.256     |

Table 8: List of background samples used in this analysis (CMSSW 76X). In the first section of the table are listed the samples of the processes for which we use the simulation to extract the final yields and shapes, in the second section the samples of the processes we will estimate from data. The MC simulation is used to design the data driven methods and derive the associated systematics.

## 142 2.4 Triggers

143 In this analysis, we consider online-reconstructed events triggered on one, two or three leptons.  
 144 The inclusion of single-lepton triggers boosts acceptance by including events where the  $p_T$  of  
 145 the subleading lepton falls below the threshold of the double-lepton triggers. In addition, by  
 146 including double-lepton triggers in the  $\geq 3$  lepton category, as well as single-lepton triggers in  
 147 all categories, we increase efficiency by considering the logical “or” of the trigger decisions of  
 148 all the individual triggers in a given category. Table 9 shows the lowest-threshold unprescaled  
 149 triggers present in the High-Level Trigger (HLT) menus for both Monte-Carlo and data in 2015.

|  |
|--|
| Same-sign dilepton ( $=2$ muons)                   |
| HLT_Mu17.TrkIsoVVL_Mu8.TrkIsoVVL.DZ.v*             |
| HLT_Mu17.TrkIsoVVL_TkMu8.TrkIsoVVL.DZ.v*           |
| HLT_IsoMu20.v*                                     |
| HLT_IsoTkMu20.v*                                   |
| Same-sign dilepton ( $=2$ electrons)               |
| HLT_Ele17_Ele12_CaloIdL_TrackIdL_IsoVL.DZ.v*       |
| HLT_Ele23_WP Loose_Gsf.v*                          |
| Same-sign dilepton ( $=1$ muon, $=1$ electron)     |
| HLT_Mu17.TrkIsoVVL_Ele12.CaloIdL_TrackIdL_IsoVL.v* |
| HLT_Mu8.TrkIsoVVL_Ele17.CaloIdL_TrackIdL_IsoVL.v*  |
| HLT_IsoMu20.v*                                     |
| HLT_IsoTkMu20.v*                                   |
| HLT_Ele23_WP Loose_Gsf.v*                          |
| Three lepton and Four lepton                       |
| HLT_DiMu9_Ele9_CaloIdL_TrackIdL.v*                 |
| HLT_Mu8_DiEle12_CaloIdL_TrackIdL.v*                |
| HLT_TripleMu_12_10_5.v*                            |
| HLT_Ele16_Ele12_Ele8_CaloIdL_TrackIdL.v*           |
| HLT_Mu17.TrkIsoVVL_Ele12.CaloIdL_TrackIdL_IsoVL.v* |
| HLT_Mu8.TrkIsoVVL_Ele17.CaloIdL_TrackIdL_IsoVL.v*  |
| HLT_Ele17_Ele12_CaloIdL_TrackIdL_IsoVL.DZ.v*       |
| HLT_Mu17.TrkIsoVVL_Mu8.TrkIsoVVL.DZ.v*             |
| HLT_Mu17.TrkIsoVVL_TkMu8.TrkIsoVVL.DZ.v*           |
| HLT_IsoMu20.v*                                     |
| HLT_IsoTkMu20.v*                                   |
| HLT_Ele23_WP Loose_Gsf.v*                          |

Table 9: Table of high-level triggers that we consider in the analysis.

## 150 2.5 Trigger efficiency in data and simulation

151 Figures 2, 3, 4, and 5 show a comparison of the trigger efficiency between data and Monte-  
 152 Carlo in each of the analysis categories. In general, we find that the trigger efficiencies in the  
 153 data agree well with simulation. Measuring the efficiency in simulated events is straightfor-  
 154 ward because there is no trigger bias with simulated events. To measure the efficiency in data  
 155 we follow the procedure described here [14], which was also the same procedure used in the  
 156 Run I multilepton analysis. We first select a set of events that were recorded on a trigger that is  
 157 uncorrelated with the lepton triggers. We use events recorded on a MET trigger as a unbiased  
 158 sample. We then look for candidate events with exactly two good leptons. We measure the ef-  
 159 ficiency for the candidate events to pass the logical “or” of triggers being considered in a given  
 160 event category (i.e., the triggers listed by category in table 9).

161

162 We use scale factors to correct for small differences in the trigger efficiency between data and  
 163 Monte-Carlo. Due to a lack of statistics, for events with  $\geq 3$  leptons we do not apply a correc-  
 164 tion factor to the simulation, but instead apply an uncertainty of 9% to all processes modeled

with simulation in this channel that is large enough to accommodate any differences in performance. For two-lepton events, we do apply correction factors to the simulation that correct for small differences in performance compared to the data. These correction factors are the ratio of the efficiency in data to the efficiency in simulation, and are summarized in table 10.

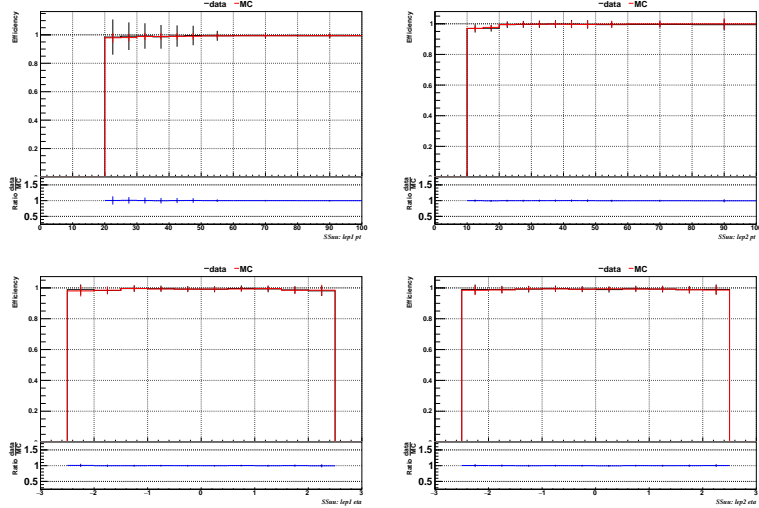


Figure 2: Comparison of the trigger efficiency in the same-sign dimuon category before corrections, shown as a function of the  $p_T$  and  $\eta$  of the leading lepton (left) and the sub-leading lepton (right).

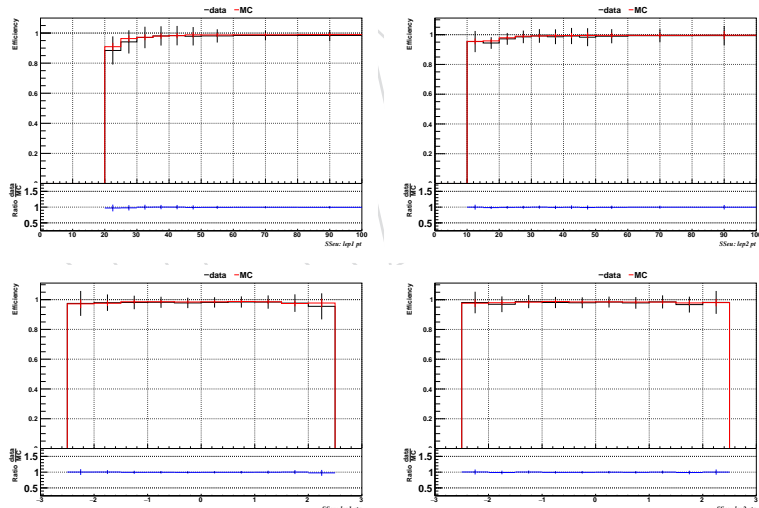


Figure 3: Comparison of the trigger efficiency in the same-sign muon+electron category before corrections, shown as a function of the  $p_T$  and  $\eta$  of the leading lepton (left) and the sub-leading lepton (right).

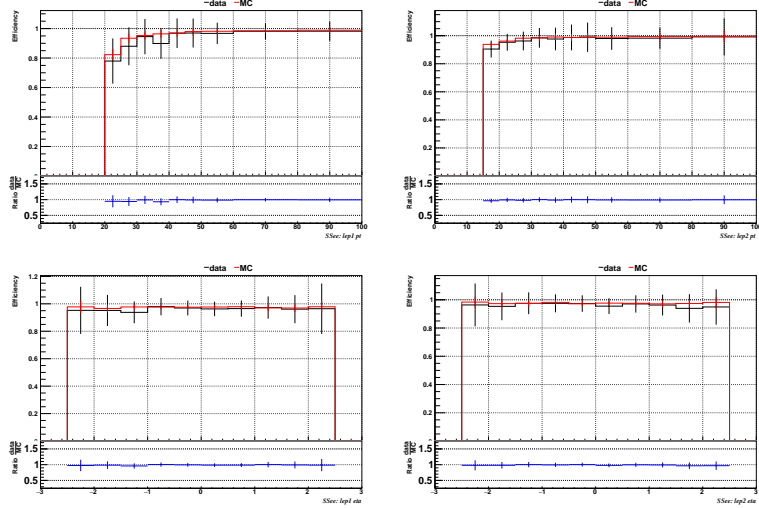


Figure 4: Comparison of the trigger efficiency in the same-sign dielectron category before corrections, shown as a function of the  $p_T$  and  $\eta$  of the leading lepton (left) and the sub-leading lepton (right).

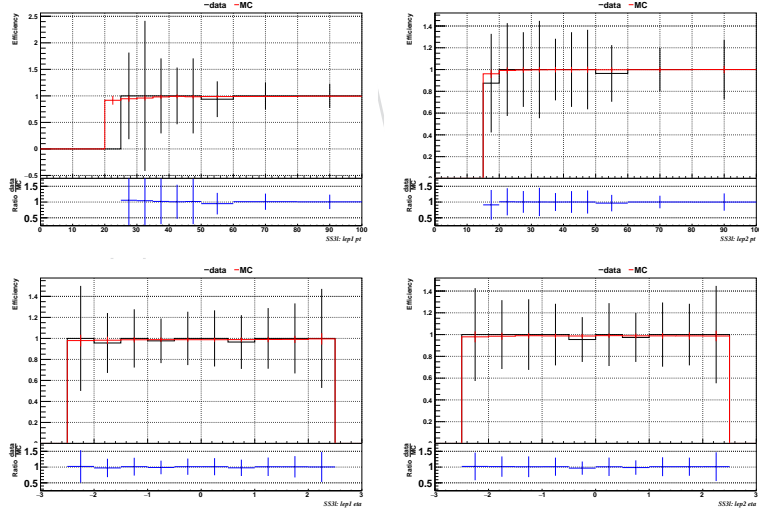


Figure 5: Comparison of the trigger efficiency in the  $\geq 3$ -lepton category before corrections, shown as a function of the  $p_T$  and  $\eta$  of the leading lepton (left) and the sub-leading lepton (right). Due to the low statistics in data, for these events we do not attempt to calculate a scale factor but instead assign an uncertainty that is large enough to cover differences in performance between data and simulation.

| Region                            | Scale Factor    |
|-----------------------------------|-----------------|
| 2e (20-40 GeV leading electron)   | $0.95 \pm 0.07$ |
| 2e ( $> 40$ GeV leading electron) | $0.99 \pm 0.03$ |
| e+mu                              | $0.98 \pm 0.01$ |
| 2mu                               | $1.00 \pm 0.01$ |
| 3 and 4l                          | $(1) \pm 0.09$  |

Table 10: Trigger efficiency scale factors and associated uncertainties, shown here rounded to the nearest percent. Because of the good agreement in trigger efficiency between data and Monte-Carlo, we apply a single small, flat correction factor for each category, with the exception of 2-electron events, where we see slightly lower efficiency at low  $p_T$  in data than we do in simulation. To account for this, we separate the 2e events into two regions: one where the leading electron has  $20 \text{ GeV} < p_T \leq 40 \text{ GeV}$ , and another where the leading electron has  $p_T > 40 \text{ GeV}$ , and apply a different flat correction factor in each region.

### 169 3 Event reconstruction and object identification

170 A complete reconstruction of the individual particles emerging from each collision event is  
 171 obtained via a particle-flow (PF) technique. The technique uses the information from all CMS  
 172 sub-detectors to identify and reconstruct individual particles in the collision event [15, 16]. The  
 173 particles are classified into mutually exclusive categories: charged hadrons, neutral hadrons,  
 174 photons, muons, and electrons.

#### 175 3.1 Jets and B-tagging

176 Jets are reconstructed by clustering PF candidates using the anti- $k_T$  algorithm with distance  
 177 parameter  $\Delta R = 0.4$  as implemented in the FASTJET package [17, 18]. The charged hadrons not  
 178 coming from the primary vertices are subtracted from the PF candidates considered in the clus-  
 179 tering. The primary vertex is chosen as the vertex with the highest sum of  $p_T^2$  of its constituent  
 180 tracks. The prescribed jet energy corrections are applied as a function of the jet  $E_T$  and  $\eta$  [19]. In  
 181 addition, a multivariate discriminator is applied to distinguish between jets coming from the  
 182 primary vertex and jets coming from pile-up vertices. The discrimination is based on the dif-  
 183 ferences in the jet shapes, in the relative multiplicity of charged and neutral components, and  
 184 in the different fraction of transverse momentum which is carried by the hardest components.  
 185 Within the tracker acceptance the jet tracks are also required to be compatible with the primary  
 186 vertex. Jets are only considered if they have a transverse energy above 25 GeV and  $|\eta| < 2.4$ .  
 187 In addition, they have to be separated from any lepton candidates passing the Fakeable Object  
 188 selection by requiring  $\Delta R = \sqrt{(\eta^\ell - \eta^{jet})^2 + (\phi^\ell - \phi^{jet})^2} > 0.4$ .

189 The CSV b-tagging algorithm [20] is used to identify jets that are likely to originate from the  
 190 hadronization of bottom quarks. This algorithm combines both secondary vertex information  
 191 and track impact parameter information together in a likelihood discriminant. The discrimi-  
 192 nant output value ranges from zero to one. It distinguishes between  $b$ -jets and jets originating  
 193 from light quarks, gluons and charm quarks. The efficiency to tag  $b$ -jets and the rate of misiden-  
 194 tification of non- $b$  jets depend on the operating point chosen. Both the efficiency and the fake  
 195 rate are parameterised as a function of the transverse momentum and pseudorapidity of the  
 196 jets. These performance measurements are obtained directly from data in samples that can be  
 197 enriched in  $b$  jets, such as  $t\bar{t}$  and multijet events where a muon can be found inside the one of  
 198 jets. Two working points for the CSV output discriminant are used in the analysis. The *loose*  
 199 one ( $\text{CSV} > 0.605$ ) has approximately 85% efficiency to tag jets with  $b$  quarks and a 10% chance  
 200 to tag jets with only light quarks or gluons. The *medium* working point ( $\text{CSV} > 0.890$ ) has ap-  
 201 proximately 70% efficiency for tagging jets with  $b$  quarks and 1.5% efficiency to tag jets with  
 202 only light quarks or gluons [20].

203 We correct for data/sim differences in the b-tagging performance by applying to the simula-  
 204 tion per-jet weights dependent on the jet pt, eta, b-tagging discriminator and flavour (from  
 205 simulation truth). The weights are derived on  $t\bar{t}$  and  $Z+jets$  events. The per-event weight  
 206 is taken as the product of the per-jet weight, including those of the jets associated to the leptons.

207

#### 208 3.2 Missing Energy

The missing transverse energy vector is calculated offline as the negative of the vector sum of transverse momenta of all PF candidates identified in the event. The magnitude of this vector is referred to as  $E_T^{\text{miss}}$ . In order to recover from the degradation of performances of the missing transverse energy due to the pile-up interactions, we consider also the  $H_T^{\text{miss}}$  variable computed in the same way as the  $E_T^{\text{miss}}$ , but using only the selected jets and leptons (the lepton selection

will be described in the following paragraphs). The  $H_T^{miss}$  variable has worse resolution than  $E_T^{miss}$  but it is more robust as it does not rely on the soft part of the event. In this analysis the event selection makes use of a linear discriminator based on the two variables,  $E_T^{miss}LD$ , exploiting the fact that  $E_T^{miss}$  and  $H_T^{miss}$  are less correlated in events with instrumental missing energy with respect to events with real missing energy. The  $E_T^{miss}LD$  is defined as

$$E_T^{miss}LD = E_T^{miss} * 0.00397 + H_T^{miss} * 0.00265 \quad (1)$$

and the working point used is  $E_T^{miss}LD > 0.2$ . Fig. 6 shows the correlation between  $H_T^{miss}$  and  $E_T^{miss}$  in signal events and DY+jets events and the comparison between the performances of the two variables and the linear discriminator.

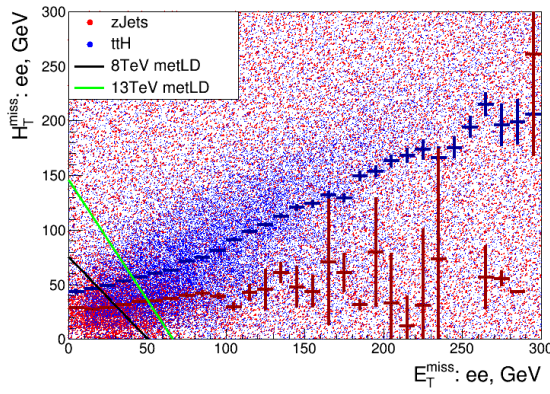


Figure 6: The figure shows the correlation between the  $H_T^{miss}$  and  $E_T^{miss}$  variables in signal events (blue) and DY+jets events (red). In the current version of the analysis the cut called *8 TeV met LD* is used.

### 3.3 Lepton Identification

Throughout this note we will call *background leptons* those coming from b-hadrons decays, from the misidentification of light jets, and from photon conversions. We consider as *signal leptons* the isolated leptons coming from W, Z, and  $\tau$  decays.

We first describe the reconstruction and identification of electron and muon candidates, and then the advanced identification criteria we used in this analysis to retain with highest possible efficiency the signal leptons while rejecting the background ones.

#### 3.3.1 Muons reconstruction and identification

Muon candidates are reconstructed combining the information from both the silicon tracker and the muon spectrometer in a global fit [21]. An identification selection is performed using the quality of the geometrical matching between the tracker and the muon system measurements.

Two working points are considered for the muon identification. The loose working point, "POG Loose ID" described in [22], and a tighter working point given by the list of requirements on the muon segment-compatibility variable, known as the "POG Medium Id", defined in [23]. The usage of each working point will be described in Table 12. Only muons within the muon system acceptance  $|\eta| < 2.4$  and minimum  $p_T$  cuts of 5 GeV are considered.

230 **3.3.2 Electron reconstruction and identification**

231 Electrons are reconstructed using tracking and electromagnetic calorimeter information by  
 232 combining ECAL superclusters and gaussian sum filter (GSF) tracks. We require electrons to  
 233 have  $|\eta| < 2.5$  to ensure that they are within the tracking volume and a minimum  $p_T$  of 7 GeV.  
 234 The electron identification is performed using a multivariate discriminant built with shower-  
 235 shape variables ( $\sigma_{i\eta i\eta}, \sigma_{i\phi i\phi}$ , the cluster circularity, widths along  $\eta$  and  $\phi$ ,  $R_9$ ,  $H/E$ ,  $E_{inES}/E_{raw}$ ),  
 236 track-cluster matching variables ( $E_{tot}/p_{in}$ ,  $E_{Ele}/p_{out}$ ,  $\Delta\eta_{in}$ ,  $\Delta\eta_{out}$ ,  $\Delta\phi_{in}$ ,  $1/E - 1/p$ ) and track  
 237 quality variables ( $\chi^2$  of the KF and GSF tracks, the number of hits used by the KF/GSF fil-  
 238 ters, fbrem). A complete description of the multivariate discriminant (MVA ID) and training  
 239 used can be found in [24]. A loose selection based on eta-dependent cuts on this discriminant  
 240 is used to preselect our electron candidates, the full shape of the discriminant is used in the  
 241 lepton multivariate selection to separate signal leptons from background leptons. Additional  
 242 identification criteria are applied for electrons with  $p_T$  greater than 30 GeV to mimic the identi-  
 243 fication applied at trigger level in order to ensure consistency between the *measurement* region  
 244 and *application* region of the fake-rate (as it will be described in dedicated sections).

245 All the selection criteria will be described in Table 13.

246 **3.3.3 Lepton vertexing**

247 With the goal of rejecting pile-up or mis-reconstructed tracks, and more importantly to reject  
 248 background leptons from b-hadron decays impact parameter variables are also considered:  
 249 impact parameter in the transverse plane  $d_0$ , impact parameter along the z axis  $d_z$ , and the  
 250 impact parameter significance in the detector space  $SIP_{3D}$ .  
 251 Loose cuts are applied on this variables to achieve the first goal, while the full shape of the same  
 252 variables is used in a multivariate approach to reach the best separation between the signal and  
 253 the background leptons.  
 254 The details of the selections are provided in Table 13, Table 12.

255 **3.3.4 Lepton isolation**

The charged leptons produced in decays of heavy particles, such as W and Z bosons, are typically spatially isolated from the hadronic activity in the event, while the leptons produced in the decays of hadrons or misidentified leptons are usually embedded in jets. This distinction become less evident moving to highly boosted systems where decay products tend to overlap. Therefore, given the higher collision energy, instead of using the standard PF Isolation where all the neutral, charged hadrons and photons are considered in a cone of  $\Delta R = \sqrt{(\eta^\ell - \eta^i)^2 + (\phi^\ell - \phi^i)^2} < 0.3$  around the leptons, a new isolation variable is constructed: the mini isolation  $I_{\text{mini}}$ .

Requiring  $I_{\text{mini}}$  below a given threshold ensures that the lepton is locally isolated, even in boosted topologies. The impact of pileup is mitigated using the so-called effective area correction:

$$I_{\text{mini}} = \frac{\sum_R p_T(h^\pm) - \max(0, \sum_R p_T(h^0) + p_T(\gamma) - \rho \mathcal{A} (\frac{R}{0.3})^2)}{p_T(\ell)}. \quad (2)$$

where  $\rho$  is the pileup energy density, where  $\sum_R p_T(h^\pm)$ ,  $\sum_R p_T(h^0)$  and  $\sum_R p_T(\gamma)$  refers to the sum of the transverse momentum of the charged hadrons, neutral hadrons and photons, respectively, within a cone  $R$ , dependent of the lepton  $p_T$ :

$$R = \frac{10}{\min(\max(p_T(\ell), 50), 200)} \quad (3)$$

| $ \eta $ range | $\mathcal{A}(e)$ neutral/charged | $\mathcal{A}(\mu)$ neutral/charged |
|----------------|----------------------------------|------------------------------------|
| 0.0 – 0.8      | 0.1607 / 0.0188                  | 0.1322 / 0.0191                    |
| 0.8 – 1.3      | 0.1579 / 0.0188                  | 0.1137 / 0.0170                    |
| 1.3 – 2.0      | 0.1120 / 0.0135                  | 0.0883 / 0.0146                    |
| 2.0 – 2.2      | 0.1228 / 0.0135                  | 0.0865 / 0.0111                    |
| 2.2 – 2.5      | 0.2156 / 0.0105                  | 0.1214 / 0.0091                    |

Table 11: Effective areas, for muons and electrons

256 The effective areas  $\mathcal{A}$  used are listed in Table 11. A very loose cut on this variable is applied  
 257 to pre-select the muon and electron candidates, while the full shape is used in the multivariate  
 258 discriminator for the signal lepton selection. Again, details of the selections are provided in in  
 259 Table 13, Table 12.

### 260 3.3.5 Jet-related variables

In this analysis the most important source of misidentified leptons comes from the decay of b-hadrons (from  $t\bar{t}$ +jets, DY+jets, and W+jets events). We therefore want to use in addition to the vertexing and isolation variables described above additional handles to target the rejection of this particular type of background leptons. These additional variables are related to the jet reconstructed in the event closest to the lepton. In particular we use the PF jets reconstructed around the leptons, requiring  $\Delta R = \sqrt{(\eta^\ell - \eta^{jet})^2 + (\phi^\ell - \phi^{jet})^2} < 0.5$ ; charged hadrons from pile-up primary vertices are not removed prior to the jet clustering. The four considered variables are the ratio between the  $p_T$  of the lepton and the  $p_T$  of the jet, the CSV b-tagging discriminator value of the jet, the number of charged tracks of the jet, and the  $p_T^{\text{rel}}$  variable:

$$p_T^{\text{rel}} = \frac{(\vec{p}(\text{jet}) - \vec{p}(\ell)) \cdot \vec{p}(\ell)}{||\vec{p}(\text{jet}) - \vec{p}(\ell)||}. \quad (4)$$

261 In order to avoid an over-correction on prompt leptons, the application of the jet energy cor-  
 262 rection is only applied on the hadronic part of the jet, using the following formula  $\text{jet} = \ell + (\text{jet-PU}-\ell) * \text{JEC} - \text{PU}$ , where  $\ell$  is the lepton, PU the pileup energy clustered into the jet,  
 263 and JEC the jet energy scale correction to be applied to any jet.  
 264

### 265 3.3.6 Lepton MVA discriminator

266 In order to profit from all these handles together, we first preselect our leptons candidates with  
 267 the *Loose* selection that will be described in the following, and we then developed a multivari-  
 268 ate discriminator based on boosted decision tree (BDT) techniques to distinguish signal leptons  
 269 (from W, Z, or  $\tau$  decays) from background leptons (mostly from b-hadron decays). We refer to  
 270 it as the *lepton MVA discriminator* throughout this document. The multivariate discriminator is  
 271 trained using simulated signal Loose leptons from the  $t\bar{t}H$  MC sample and fake leptons from  
 272 the  $t\bar{t}$ +jets MC sample, separately for muons and electrons. It uses as input variables the ver-  
 273 texing, isolation and jet-related variables described so far, the  $p_T$  and  $\eta$  of the lepton and two  
 274 additional variables that contribute to make it robust also in the rejection of leptons from light  
 275 jets mis-identification: the electron MVA ID discriminator and the muon segment-compatibility  
 276 variables.

277 In Fig. 7 the performances of the lepton MVA are described comparing the efficiency on sig-  
 278 nals lepton from  $t\bar{t}H$  to the one on background leptons from  $t\bar{t}$  that pass the preselection. The  
 279 performances are compared with what we would obtained simply using the  $I_{\text{mini}}$ , and with  
 280 the identification working point choose by the same-sign dilepton SUSY analysis (SUS-15-008),

which is a cut based algorithm based on  $I_{\text{mini}}$ ,  $p_T^{\text{ratio}}$ ,  $p_T^{\text{rel}}$ ,  $\text{SIP}_{3D}$  on top of the Muon Medium ID and a tight working point for the electron MVA ID.

283

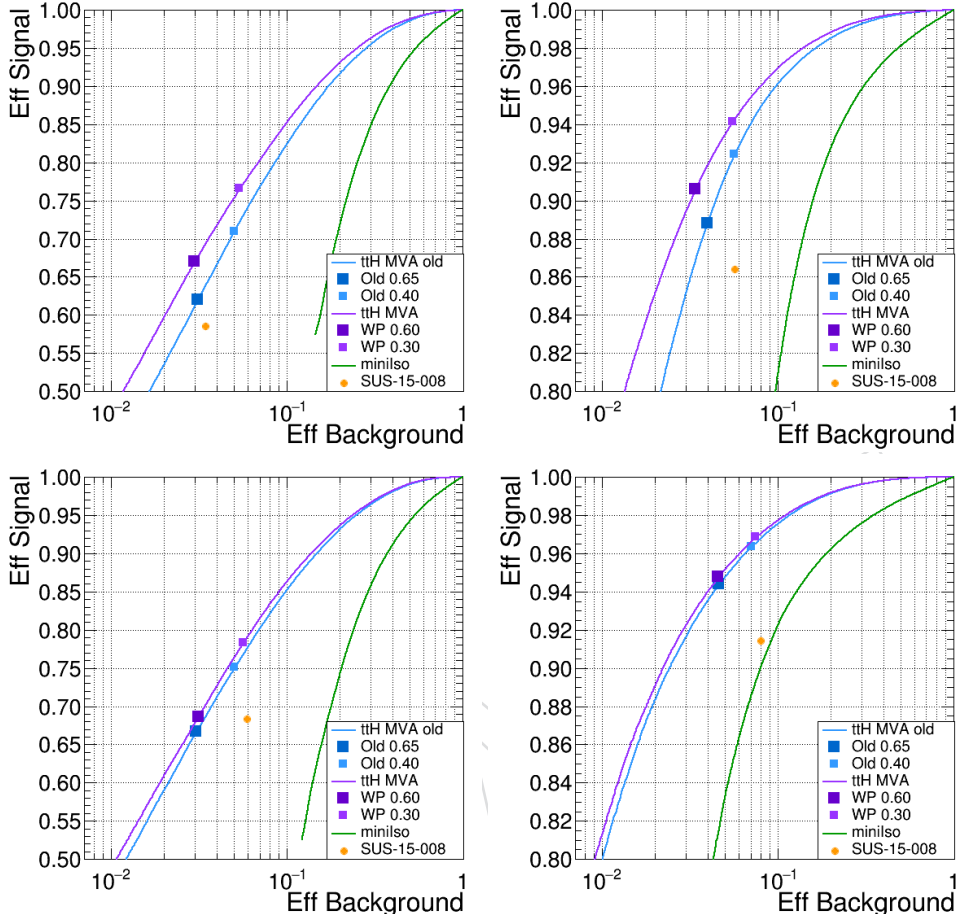


Figure 7: The lepton MVA ROCs are shown from top left to bottom right for electrons with  $10 < p_T < 25$ , electrons with  $p_T > 25$ , muons with  $10 < p_T < 25$ , muons with  $p_T > 25$

### 284 3.3.7 Additional requirements

In the dilepton final state additional requirements on the quality of the charge assignment are applied to suppress opposite-sign events in which the charge of one of the leptons is mismeasured. For the electrons we require consistency between the independent measurements of the charge from the ECAL supercluster and the tracker, while for the muons we require the track transverse momentum to be well measured ( $\Delta p_T / p_T < 0.2$ ). We will refer to these cuts as *tight-charge*

Moreover in order to suppress as much as possible background electrons from photon conversions we reject electrons with missing hits in the innermost layer or associated with a successfully reconstructed conversion vertex [25].

### 294 3.3.8 Loose, *Fakeable Object*, Tight definitions

Three different selections are used both for the electron and the muon objects identification: the *Loose*, the *Fakeable Object*, the *Tight* selection. In the description of the analysis strategy it will be explained for which purposes the different criteria are used.

For reasons that will explained in the data-driven background prediction session, for the Fakeable Object selections the lepton  $p_T$  is intended to  $0.85 * p_T(jet)$  with the jet being the one associated to the lepton as defined for the jet-related variables computation.

In Table 12 and Table 13 all the criteria on the variables previously described are listed.

Table 12: Requirements on each of the three muon selections. In the cases where the cut values change between the selections, those values are listed in the table. Otherwise, whether the cut is applied is indicated. For the two  $p_T^{\text{ratio}}$  and CSV rows, the cuts marked with † are applied to leptons that fail the lepton MVA cut, while the loose cut value to those that pass the lepton MVA cut.

| Cut                            | Loose | Fakeable Object     | Tight    |
|--------------------------------|-------|---------------------|----------|
| $ \eta  < 2.4$                 | ✓     | ✓                   | ✓        |
| $p_T$                          | $> 5$ | $> 10$              | $> 10$   |
| $ d_{xy}  < 0.05 \text{ (cm)}$ | ✓     | ✓                   | ✓        |
| $ d_z  < 0.1 \text{ (cm)}$     | ✓     | ✓                   | ✓        |
| $\text{SIP}_{3D} < 8$          | ✓     | ✓                   | ✓        |
| $I_{\text{mini}} < 0.4$        | ✓     | ✓                   | ✓        |
| is Loose Muon                  | ✓     | ✓                   | ✓        |
| $p_T^{\text{ratio}}$           | —     | $> 0.3† / -$        | —        |
| jet CSV                        | —     | $< 0.605† / < 0.89$ | $< 0.89$ |
| is Medium Muon                 | —     | —                   | ✓        |
| tight-charge                   | —     | —                   | ✓        |
| lepMVA $> 0.75$                | —     | —                   | ✓        |

### 3.4 Validation of lepton identification variables

We validate the modelling of the lepton identification variables in simulation by looking at two control regions, one enriched in prompt leptons from dileptonic  $t\bar{t}$ , and one enriched in non-prompt leptons from semi-leptonic  $t\bar{t}$ . The first control region is obtained selecting opposite-sign dilepton events with at least two jets and at least one medium b-tagged jet or two loose ones; events with more than two leptons are vetoed. The second control region is obtained

Table 13: Requirements on each of the three electron selections. In the cases where the cut values change between the selections, those values are listed in the table. Otherwise, whether the cut is applied is indicated. In some cases, the cut values change for different  $\eta$  ranges. These ranges are  $0 < |\eta| < 0.8$ ,  $0.8 < |\eta| < 1.479$ , and  $1.479 < |\eta| < 2.5$  and the respective cut values are given in the form (value<sub>1</sub>, value<sub>2</sub>, value<sub>3</sub>).

| Cut   | Loose                     | Fakeable Object           | Tight                       |
|---|---------------------------|---------------------------|-----------------------------|
| $ \eta  < 2.5$                              | ✓                         | ✓                         | ✓                           |
| $p_T$                                       | $> 7$                     | $> 10$                    | $> 15(10) \text{ 2lss}(3l)$ |
| $ d_{xy}  < 0.05 \text{ (cm)}$              | ✓                         | ✓                         | ✓                           |
| $ d_z  < 0.1 \text{ (cm)}$                  | ✓                         | ✓                         | ✓                           |
| $\text{SIP}_{3D} < 8$                       | ✓                         | ✓                         | ✓                           |
| $I_{\text{mini}} < 0.4$                     | ✓                         | ✓                         | ✓                           |
| MVA ID                                      | $> (-0.70, -0.83, -0.92)$ | $> (-0.70, -0.83, -0.92)$ | $> (-0.70, -0.83, -0.92)$   |
| $\sigma_{inj} < (0.011, 0.011, 0.030)$      | —                         | for $p_T > 30$            | for $p_T > 30$              |
| $H/E < (0.10, 0.10, 0.07)$                  | —                         | for $p_T > 30$            | for $p_T > 30$              |
| $\Delta\eta_{in} < (0.01, 0.01, 0.008)$     | —                         | for $p_T > 30$            | for $p_T > 30$              |
| $\Delta\phi_{in} < (0.04, 0.04, 0.07)$      | —                         | for $p_T > 30$            | for $p_T > 30$              |
| $-0.05 < 1/E - 1/p < (0.010, 0.010, 0.005)$ | —                         | for $p_T > 30$            | for $p_T > 30$              |
| $p_T^{\text{ratio}}$                        | —                         | $> 0.3† / -$              | —                           |
| jet CSV                                     | —                         | $< 0.605† / < 0.89$       | $< 0.89$                    |
| tight-charge                                | —                         | —                         | ✓                           |
| conversion rejection                        | —                         | —                         | ✓                           |
| Number of missing hits                      | $< 2$                     | $== 0$                    | $== 0$                      |
| lepMVA $> 0.75$                             | —                         | —                         | ✓                           |

308 selecting same-sign dilepton events with at exactly three or four jets, and exactly one medium  
 309 b-tagged jet, in order to suppress the contributions from  $t\bar{t}V$  and  $t\bar{t}H$ , and similarly events with  
 310 more than two leptons are vetoed. In both control regions, the trailing lepton is required only  
 311 to pass the loose selection, not the lepMVA requirement, so that its properties can be studied  
 312 in an unbiased way. A data to simulation comparison is done for the lepton MVA discriminant  
 313 and some of the more important inputs: the mini-isolation,  $SIP_{3D}$ ,  $p_T^{\text{ratio}}$ ,  $p_T^{\text{rel}}$  and the b-tagging  
 314 discriminator of the associated jet (Fig. 8 and 9). In all cases, the simulation is normalized to  
 315 data, scaling all contributions by the same factor. The contribution from  $t\bar{t}$  is split according to  
 316 the origin of the lepton in the simulation: prompt, non-prompt from B hadron decays ( $b \rightarrow l_{\text{np}}$ ),  
 317 or non-prompt from other origins ( $j \rightarrow l_{\text{np}}$ ). A good agreement between data and simulations is  
 318 observed overall. Some small discrepancy is visible mainly for extreme values of the b-tagging  
 319 discriminator and small  $SIP_{3D}$  for non-prompt leptons, which could be also be partially from  
 320 different relative abundances of leptons from heavy flavour vs light flavour processes in data  
 321 with respect to simulations, or a slightly different levels of prompt lepton contamination.

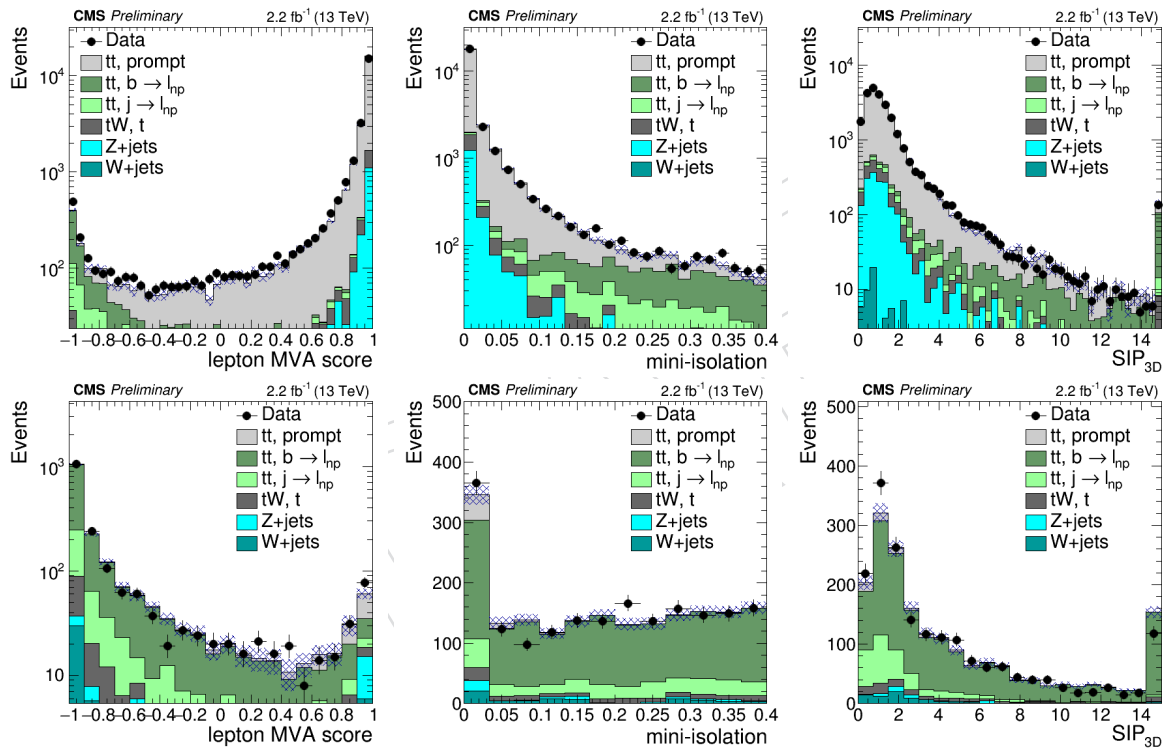


Figure 8: Comparison of the distributions for the lepton MVA (left), mini-isolation (center), and  $SIP_{3D}$  (right) between data and simulations in control regions enriched in prompt leptons (top) or non-prompt leptons (bottom), as described in the text. The uncertainty shown on the simulation is only statistical. These plots currently the ones from the DPS approved for the December Jamboree, but will be updated with the final lepton definitions.

### 322 3.4.1 Loose selection efficiency

The reconstruction and Loose identification efficiency are computed both for muons and electrons using the Tag and Probe technique with  $Z \rightarrow \ell^+\ell^-$  events, in data and in simulation separately. The efficiency scale factor is therefore defined as:

$$\rho(p_T, \eta) = \frac{\varepsilon_{\text{data}}(p_T, \eta)}{\varepsilon_{\text{MC}}(p_T, \eta)}, \quad (5)$$

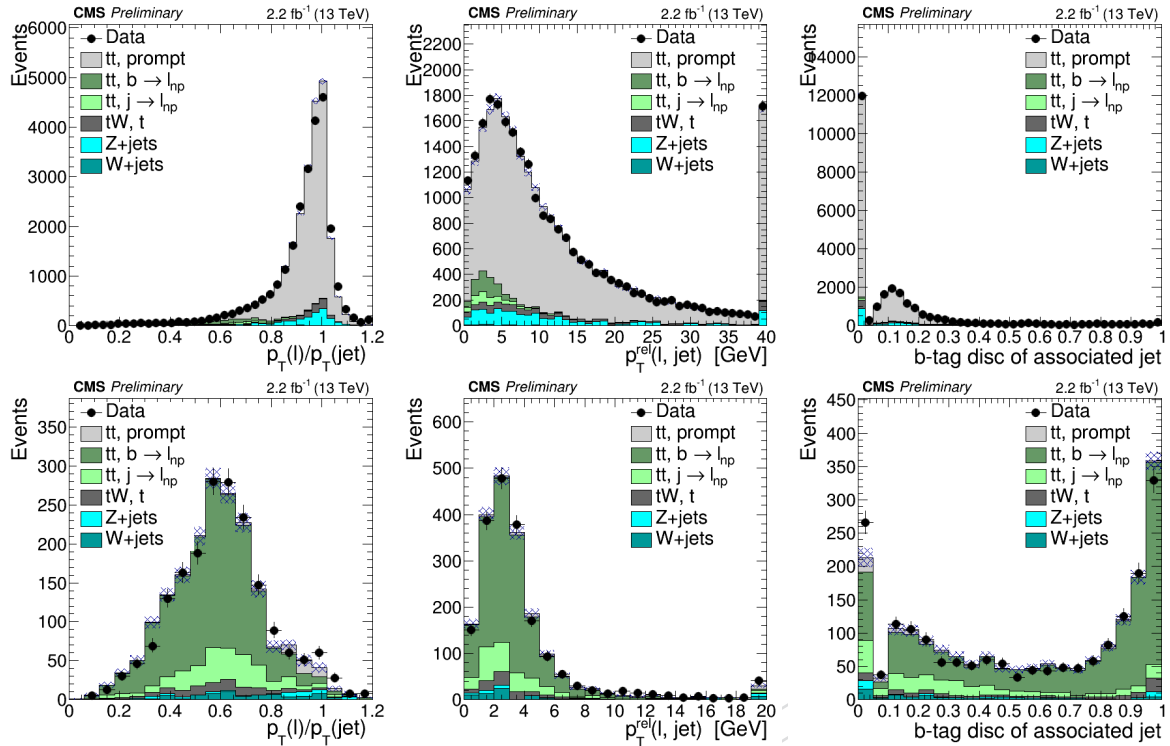


Figure 9: Comparison of the distributions for the lepton  $p_T^{\text{ratio}}$  (left),  $p_T^{\text{rel}}$  (center) and the b-tagging discriminator of the associated jet (right), between data and simulations in control regions enriched in prompt leptons (top) or non-prompt leptons (bottom), as described in the text. The uncertainty shown on the simulation is only statistical. These plots currently the ones from the DPS approved for the December Jamboree, but will be updated with the final lepton definitions.

where  $\epsilon_i(p_T, \eta)$  is the efficiency measured for a given lepton in the process i (data or simulation). The scale factor is used afterward to correct the weight of the simulated event. The full simulation correction from the lepton side is thus given by the product of all scale factors :

$$\rho = \prod_{j \in \text{leptons}} \prod_{i \in \text{efficiencies}} \rho_i(p_T(j), \eta_j) \quad (6)$$

In Fig. 11 the scale factors for the Loose Muon selection are shown. In Fig. 10 the scale factors for the Loose Electron selection (with the Electron ID Emulation cuts) are shown. Few of the tight selections cuts have also been measured with the same procedure: the muon Medium ID with respect to the Loose selection , the electron conversion rejection and missing hits cuts with respect to the Loose selection.

Systematics on these scale-factors related to the method have been evaluated and are of the order of 2% for both lepton flavors, in all the considered kinematic range. These results have derived with Muon POG and EGamma official tools and are described in details here[26].

331

### 332 3.4.2 Tight vs Loose selection efficiency

The efficiencies of applying the tight selection as defined in Tables 12 and 13, on the loose leptons are determined using a tag and probe method on a sample of DY-enriched events. The denominator definitions for these efficiencies includes the  $SIP_{3D} < 8$  as it is already included in the loose lepton efficiencies described in Section 3.4.1. Numerator cuts for the same-sign dilepton efficiencies include the tight-charge requirement.

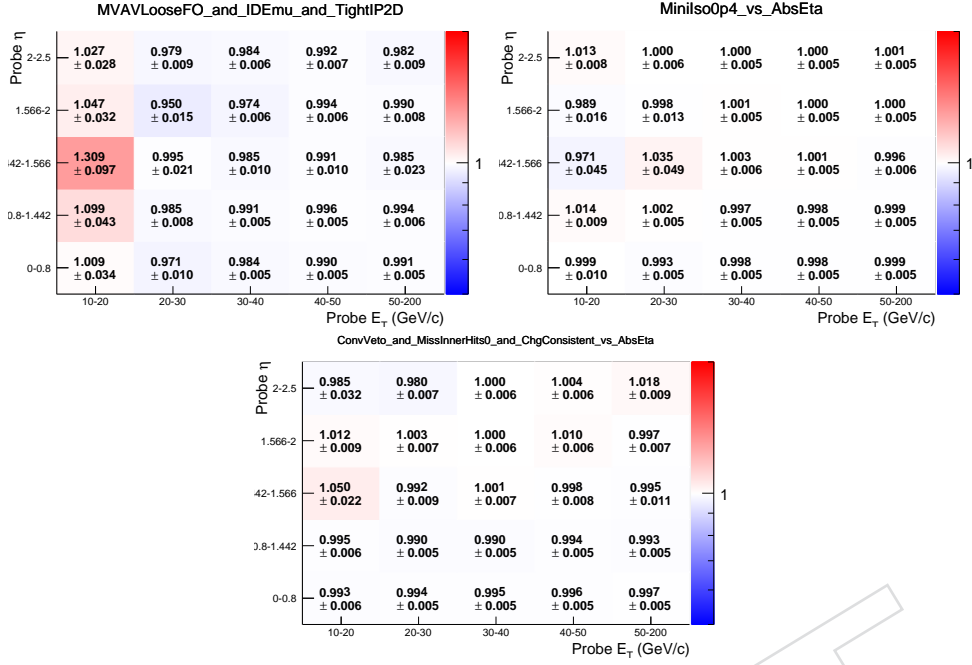


Figure 10: From left to right: electron data to simulation scale factors for the Loose WP of the Electron MVA ID together with the Loose IP cuts and HLT ID Emulation requirements, for the Loose  $I_{\text{mini}}$ , for the Tight cuts on the conversion veto and the missing inner hits

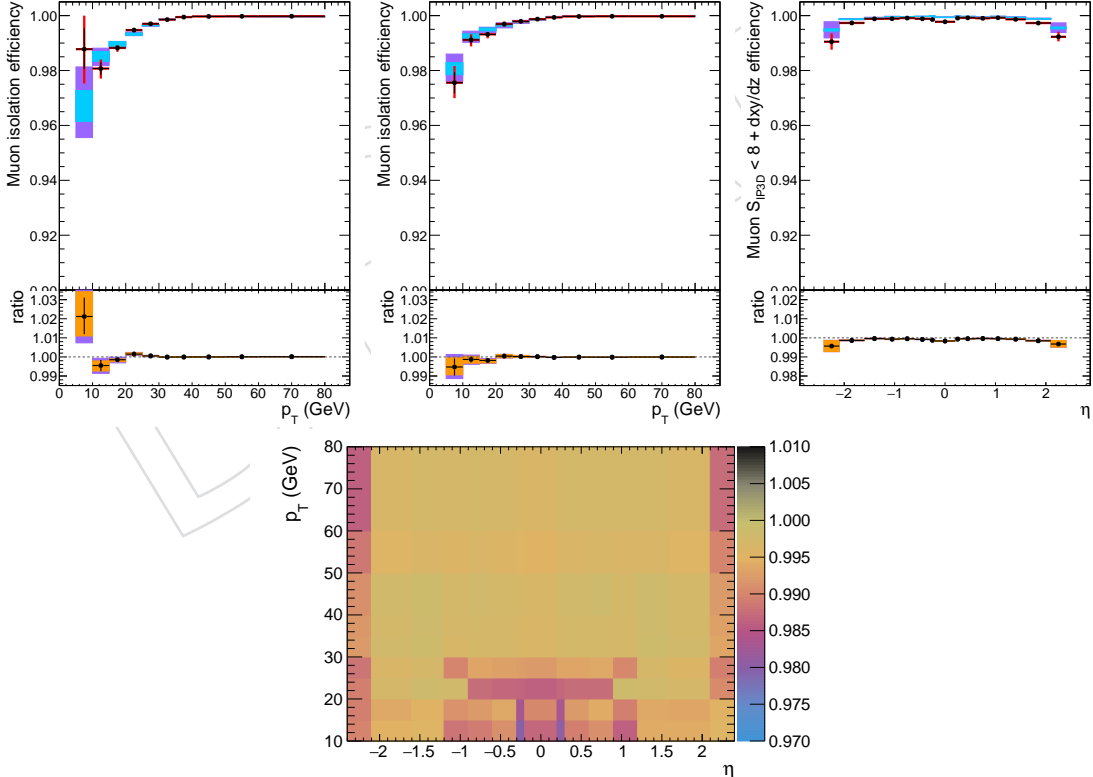


Figure 11: From left to right: muon data and simulation efficiency for the loose isolation requirement in the barrel and endcap regions, muon data and simulation efficiency for the loose impact parameters cuts, and the data to simulation scale factors for the loose selection.

338 Number of passed and failed probes are determined from a fit to the invariant mass of the  
 339 dilepton system. The resulting efficiencies are shown in Figures 12, 13, 14, and 15.

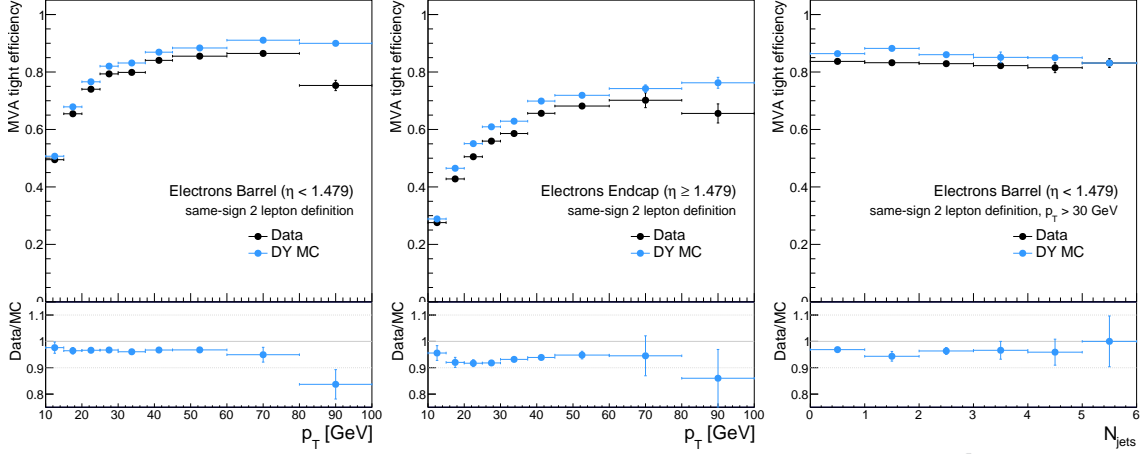


Figure 12: Tight vs loose selection efficiencies for electrons, for the same-sign dilepton lepton definition (i.e. including the tight-charge requirement).

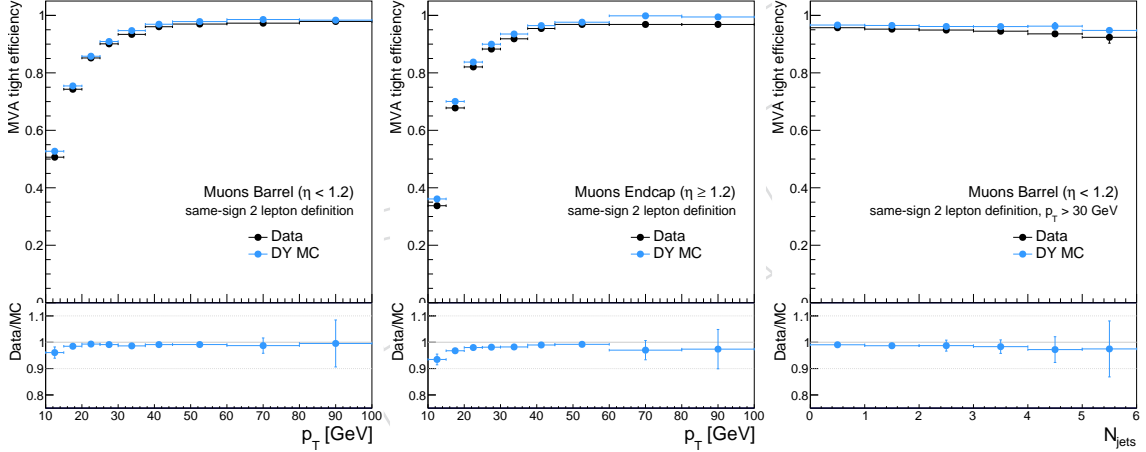


Figure 13: Tight vs loose selection efficiencies for muons, for the same-sign dilepton lepton definition (i.e. including the tight-charge requirement).

340 We use these  $(\eta, p_T)$  dependent scale factors to correct the simulation. A flat uncertainty of 3%  
 341 which is of the order of the current statistical uncertainty is assigned to these scale factors.

### 342 3.5 Taus

343 Hadronically decaying taus ( $\tau_h$ ) are reconstructed using the hadron-plus-strips algorithm [27].  
 344  $\tau_h$  candidates are required to pass the “decay mode finding” discriminator, either being recon-  
 345 structed in 1- or 3-prong decay modes with or without additional  $\pi^0$ s. In addition, they have  
 346 to fulfill  $p_T > 20$  GeV and  $|\eta| < 2.3$  per recommendation from the tau POG.

347 As described below, all event categories with at least one  $\tau_h$  candidate also have the require-  
 348 ment of a same-sign light-lepton pair. This implies that the only relevant backgrounds where  
 349 jets misidentified as  $\tau_h$  are backgrounds with real same-sign lepton pairs, which are overall a  
 350 small contribution. For this reason, loose tau identification criteria are deployed with jet-to- $\tau_h$

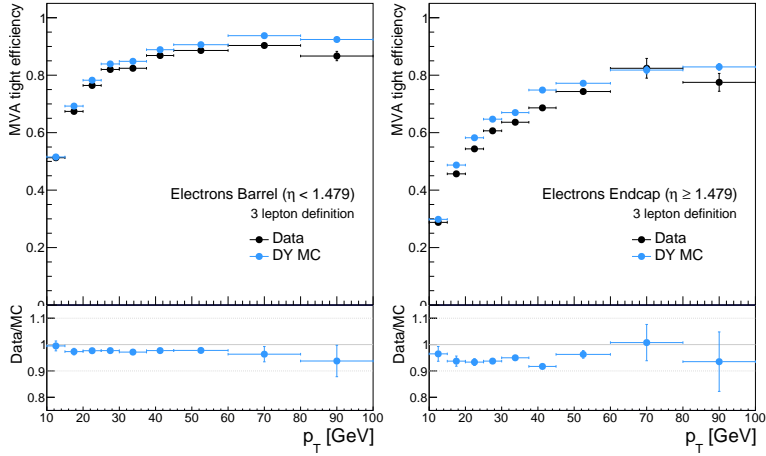


Figure 14: Tight vs loose selection efficiencies for electrons, for the three lepton channel (i.e. not including the tight-charge requirement).

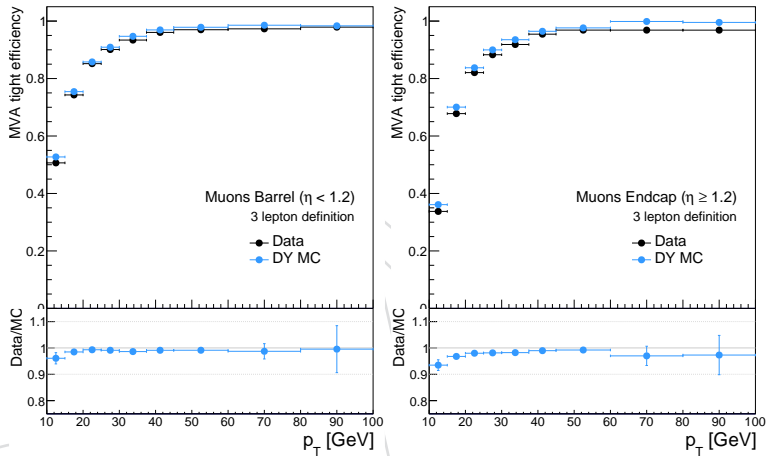


Figure 15: Tight vs loose selection efficiencies for muons, for the three lepton channel (i.e. not including the tight-charge requirement).

misidentification rates of the order of 1% (as opposed to tighter criteria that bring this down by one additional order of magnitude).

For the current version of the analysis with CMSSW 74X, a loose cutoff-based tau identification is applied (“byLooseCombinedIsolationDeltaBetaCorr3Hits”). For the updated version of the analysis with CMSSW 76X, an improved MVA-based identification criterion will be used that was specifically trained using  $t\bar{t}$  and  $t\bar{t}h$  decays and makes use of a smaller isolation cone size of 0.3 than other identification criteria (“byLooseIsolationMVArun2v1DBdR03oldDMwLT”) [28]. This update is expected to significantly increase the selection efficiency for generated  $\tau_h$ .

Reconstructed  $\tau_h$  candidates are removed if they overlap within  $\Delta R = 0.5$  with *loose* electrons and muons. This discards less than 1% of the generated  $\tau_h$  decays after the final event selection. No dedicated discriminators against background from prompt electrons and muons are applied since the contribution from background events with additional prompt electrons and muons passing the  $\tau_h$  selection criteria but not the muon and electron pre-selection requirements is negligible.

## 365 4 Event selection

366 The event selection aims at rejecting events that do not match the decay signatures targeted  
 367 by this analysis. We require that at least two leptons passing the tight selection are present in  
 368 the event. Moreover, events where a pair of loose leptons with an invariant mass smaller than  
 369 12 GeV is found are rejected, as they are not modeled by the simulation.

370 As in signal events a pair of top quarks that decay into b-jets is present, we require that at  
 371 least two jets with transverse momentum greater than 25 GeV are reconstructed in the  $|\eta| < 2.4$   
 372 region. We also require that both satisfy the loose working point of the CSV b-tag algorithm, or  
 373 that at least one of them satisfies the medium working point of that tagger.

### 374 4.1 Two lepton same-sign category

375 In events where no additional tight lepton with a transverse momentum greater than 10 GeV is  
 376 present, we require that the two tight leptons have the same charge and transverse momenta  
 377 greater than 20 GeV and 10 GeV respectively. These events constitute the two lepton same-sign  
 378 ( $2l_{ss}$ ) category of the analysis. If the sub-leading lepton is an electron, and only for this category,  
 379 its transverse momentum requirement is tightened to 15 GeV.

380 In addition to the requirements described above, we discard  $2l_{ss}$  events that contain less than  
 381 four jets with transverse momentum greater than 25 GeV and  $|\eta| < 2.4$  in the final state.

382 The event is also rejected if the two selected leptons do not pass the requirements aimed at re-  
 383 jecting leptons from conversions and those on the quality of the charge measurement described  
 384 in Section 3. The background from electrons from Z decays, where the charge of one electron  
 385 is mismeasured, is further reduced by vetoing events where the di-electron invariant mass dif-  
 386 fers by less than 10 GeV from the Z mass. For the same reason, we also require that the  $E_T^{\text{miss}} LD$   
 387 variable is larger than 0.2 in di-electron events.

### 388 4.2 Three lepton category

389 The three lepton ( $3l$ ) category consists of events that contain three tight leptons with a trans-  
 390 verse momenta greater than 20, 10 and 10 GeV respectively. No requirement is applied on the  
 391 possible presence of an even larger number of leptons; i.e., this category implicitly includes  
 392 events with four or more leptons.

393 In order to reject backgrounds from processes with Z bosons in the final state, we require that  
 394 no pair of same-flavor opposite-sign loose leptons has an invariant mass closer than 10 GeV to  
 395 the mass of the Z boson. We then add an  $E_T^{\text{miss}} LD > 0.2$  requirement. The  $E_T^{\text{miss}} LD$  threshold  
 396 is tighter (0.3) if the event has a pair of leptons with the same flavor and opposite sign. For  
 397 events with large jet multiplicity ( $\geq 4$  jets), where the contamination from the Z background is  
 398 smaller, no requirement on  $E_T^{\text{miss}} LD$  is applied. The event is also rejected if the three selected  
 399 leptons do not pass the conversion veto requirements, or if the sum of their charges is not equal  
 400 to +1 or -1.

401 The observed event yields in data for each final state and the expectations from the different  
 402 physical processes are summarised in table 14.

403 Figures 16-26 and 27-30 show the main event observables (lepton and jet multiplicities and  
 404 spectra, energy sums) for events passing the  $2\ell$  and  $3\ell$  selections.

|                 | $\mu\mu$        | $ee$            | $e\mu$           | $3\ell$          |
|-----------------|-----------------|-----------------|------------------|------------------|
| tH              | $1.49 \pm 0.08$ | $0.67 \pm 0.05$ | $2.21 \pm 0.09$  | $2.07 \pm 0.09$  |
| tW              | $3.14 \pm 0.16$ | $1.44 \pm 0.11$ | $4.82 \pm 0.19$  | $2.50 \pm 0.13$  |
| tZ/ $\gamma^*$  | $0.80 \pm 0.03$ | $1.11 \pm 0.14$ | $2.36 \pm 0.16$  | $3.65 \pm 0.18$  |
| WZ              | $0.09 \pm 0.05$ | $0.06 \pm 0.06$ | $0.24 \pm 0.11$  | $0.32 \pm 0.11$  |
| rare SM bkg.    | $0.28 \pm 0.07$ | $0.11 \pm 0.10$ | $0.42 \pm 0.13$  | $0.81 \pm 0.19$  |
| WW same-sign    | $0.06 \pm 0.03$ | $0.04 \pm 0.04$ | $0.09 \pm 0.06$  | $0.00 \pm 0.00$  |
| non-prompt      | $3.56 \pm 0.35$ | $2.85 \pm 0.53$ | $6.66 \pm 0.70$  | $5.22 \pm 0.55$  |
| charge mis-ID   | $0.12 \pm 0.09$ | $1.04 \pm 0.19$ | $1.97 \pm 0.27$  |                  |
| signal          | $1.49 \pm 0.08$ | $0.67 \pm 0.05$ | $2.21 \pm 0.09$  | $2.07 \pm 0.09$  |
| all backgrounds | $8.04 \pm 0.42$ | $6.64 \pm 0.60$ | $16.56 \pm 0.80$ | $12.49 \pm 0.89$ |
| data            | 9               | 11              | 11               | 28               |

Table 14: Expected and observed yields after the selection in all final states. The rare SM backgrounds include triboson production, tbZ,  $W^\pm W^\pm qq$ , and WW produced in double-parton interactions. Uncertainties are statistical only.

|                      | $\mu\mu$        | $ee$            | $e\mu$           | $3\ell$          |
|----------------------|-----------------|-----------------|------------------|------------------|
| tH                   | $1.49 \pm 0.08$ | $0.67 \pm 0.05$ | $2.21 \pm 0.09$  | $2.07 \pm 0.09$  |
| tW                   | $3.14 \pm 0.16$ | $1.44 \pm 0.11$ | $4.82 \pm 0.19$  | $2.50 \pm 0.13$  |
| tZ/ $\gamma^*$       | $0.80 \pm 0.03$ | $1.11 \pm 0.14$ | $2.36 \pm 0.16$  | $3.65 \pm 0.18$  |
| WZ                   | $0.09 \pm 0.05$ | $0.06 \pm 0.06$ | $0.24 \pm 0.11$  | $0.32 \pm 0.11$  |
| rare SM bkg.         | $0.28 \pm 0.07$ | $0.11 \pm 0.10$ | $0.42 \pm 0.13$  | $0.81 \pm 0.19$  |
| WW same-sign         | $0.06 \pm 0.03$ | $0.04 \pm 0.04$ | $0.09 \pm 0.06$  | $0.00 \pm 0.00$  |
| non-prompt (data)    | $3.99 \pm 0.38$ | $3.58 \pm 0.38$ | $10.10 \pm 0.65$ | $8.08 \pm 0.67$  |
| charge mis-ID (data) |                 | $1.11 \pm 0.05$ | $1.65 \pm 0.05$  |                  |
| signal               | $1.49 \pm 0.08$ | $0.67 \pm 0.05$ | $2.21 \pm 0.09$  | $2.07 \pm 0.09$  |
| all backgrounds      | $8.36 \pm 0.42$ | $7.44 \pm 0.44$ | $19.69 \pm 0.72$ | $15.36 \pm 0.93$ |
| data                 | 9               | 11              | 11               | 28               |

Table 15: Expected and observed yields after the selection in all final states. The rare SM backgrounds include triboson production, tbZ,  $W^\pm W^\pm qq$ , and WW produced in double-parton interactions. Uncertainties are statistical only. The backgrounds from non-prompt leptons and charge flips are extracted from data.

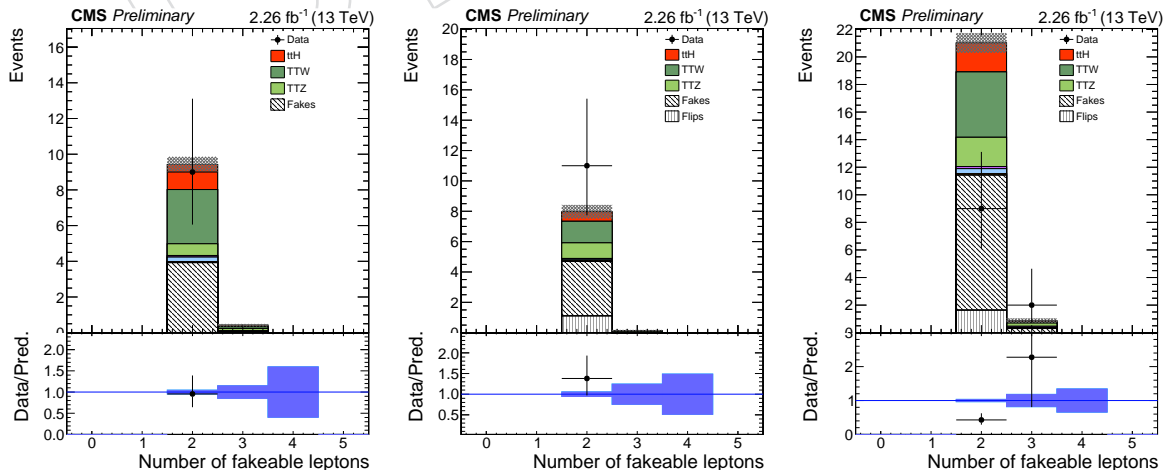


Figure 16: Number of leptons passing the fakeable object requirements in the  $2\ell$  ( $\mu\mu$ ,  $ee$ ,  $e\mu$ ) selections.

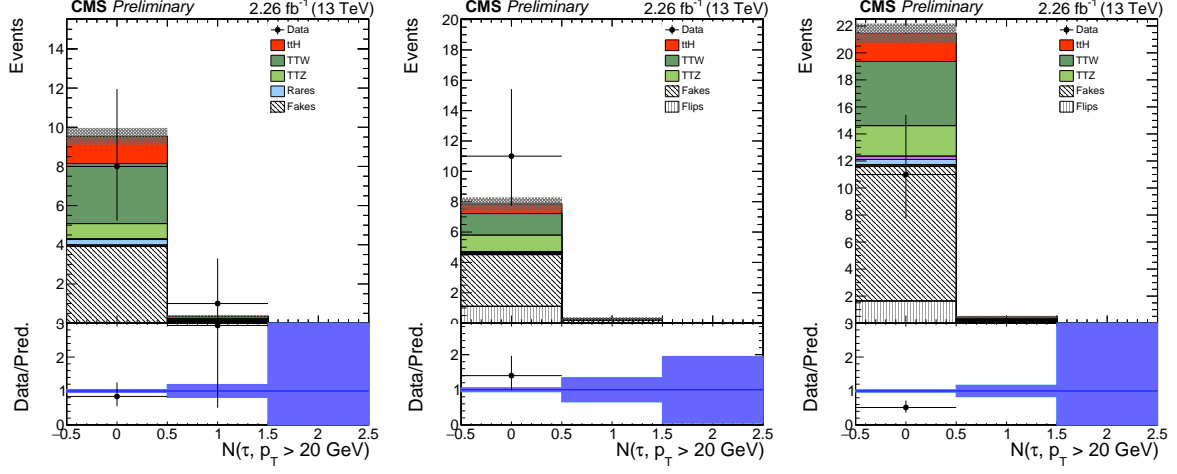


Figure 17: Number of reconstructed  $\tau_h$  leptons passing the requirements described in Section 3.5 in the  $2\ell$  ( $\mu\mu$ ,  $ee$ ,  $e\mu$ ) selections.

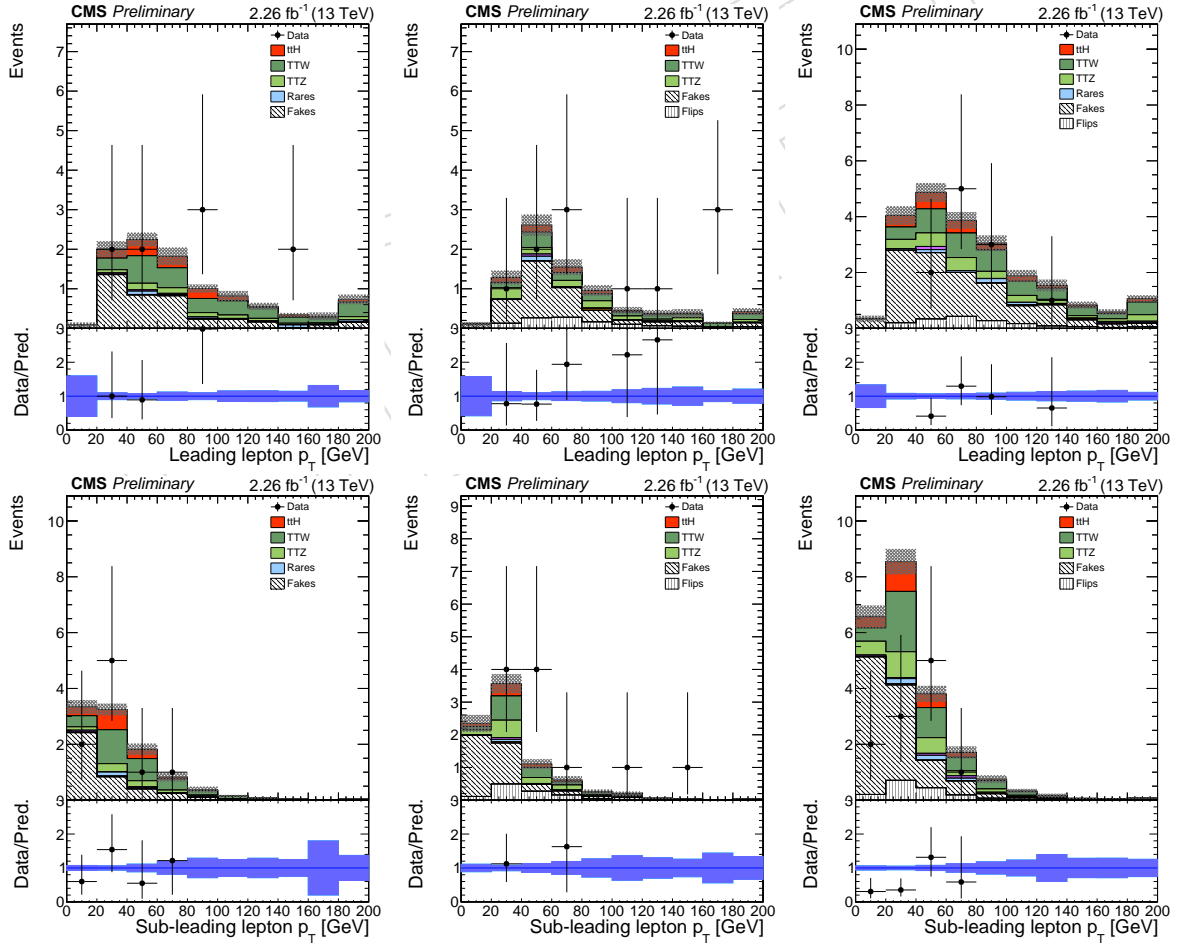
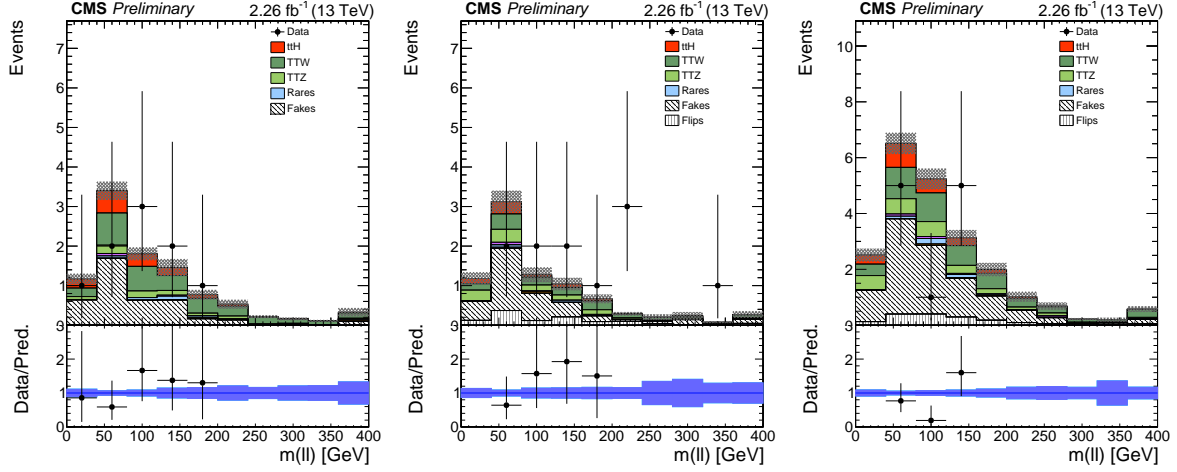
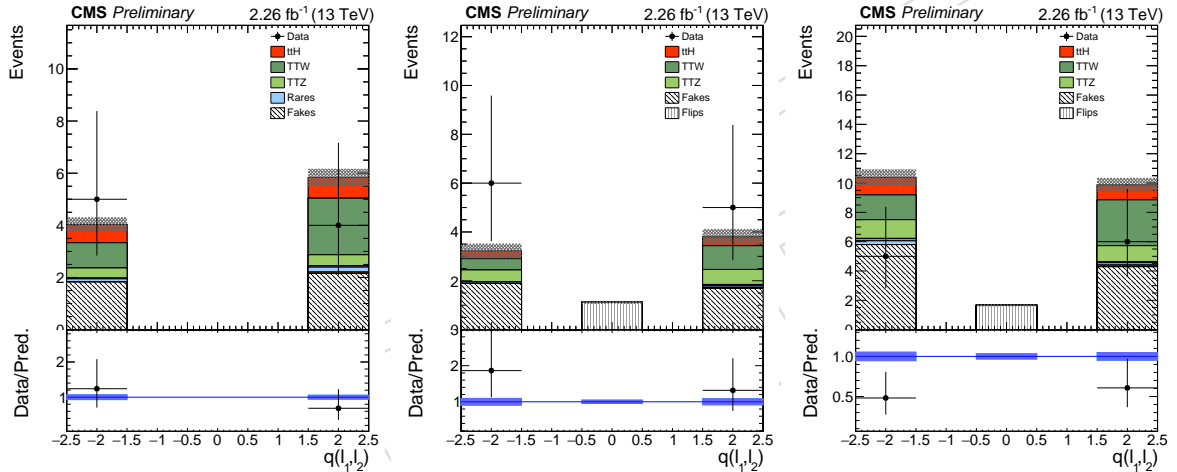
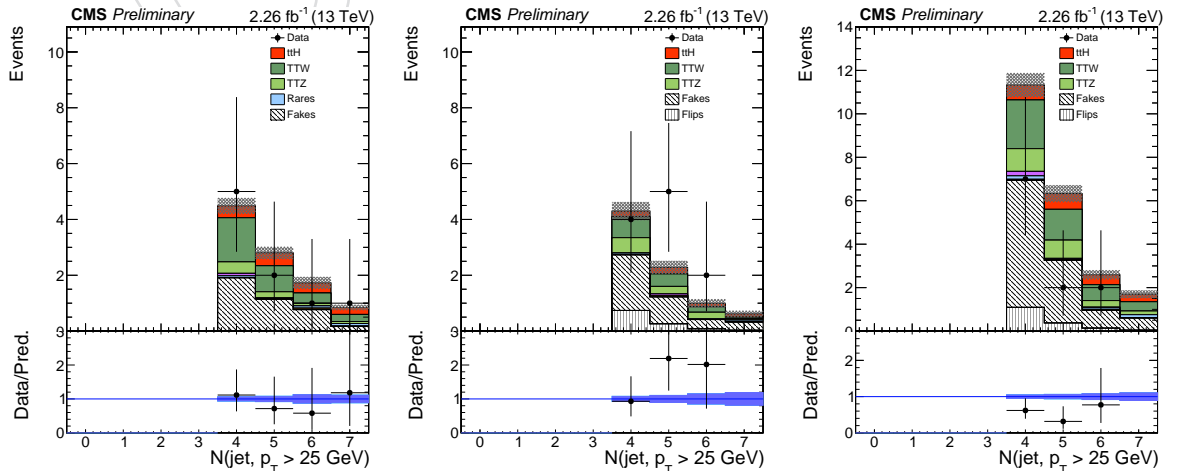


Figure 18: Lepton transverse momentum spectra in the  $2\ell$  ( $\mu\mu$ ,  $ee$ ,  $e\mu$ ) selections.

Figure 19: Di-lepton invariant mass spectra in the  $2\ell$  ( $\mu\mu$ ,  $ee$ ,  $e\mu$ ) selections.Figure 20: Sum of lepton charges in the  $2\ell$  ( $\mu\mu$ ,  $ee$ ,  $e\mu$ ) selections.Figure 21: Jet multiplicity in the  $2\ell$  ( $\mu\mu$ ,  $ee$ ,  $e\mu$ ) selections.

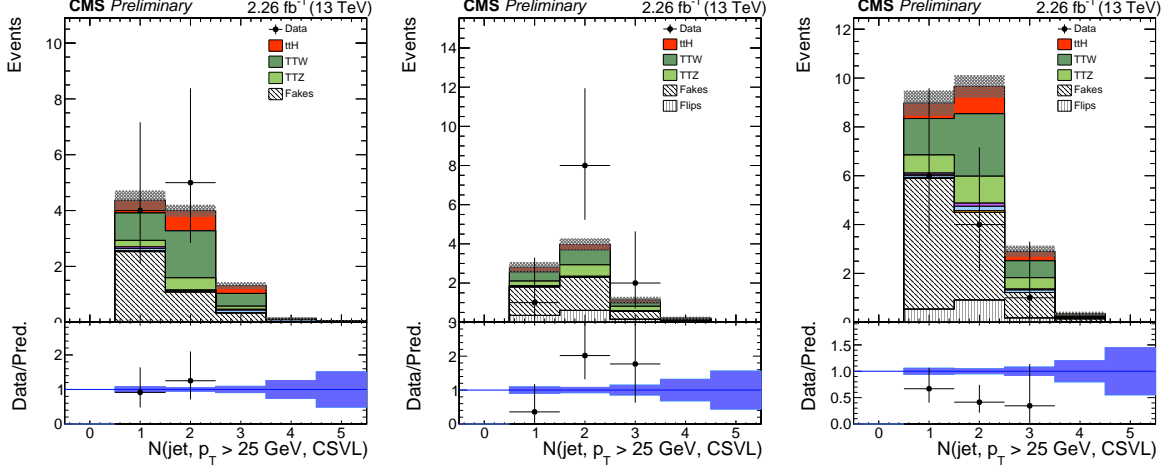


Figure 22: Multiplicity of jets passing the loose working point of the CSV tagger in the  $2\ell$  ( $\mu\mu$ ,  $ee$ ,  $e\mu$ ) selections.

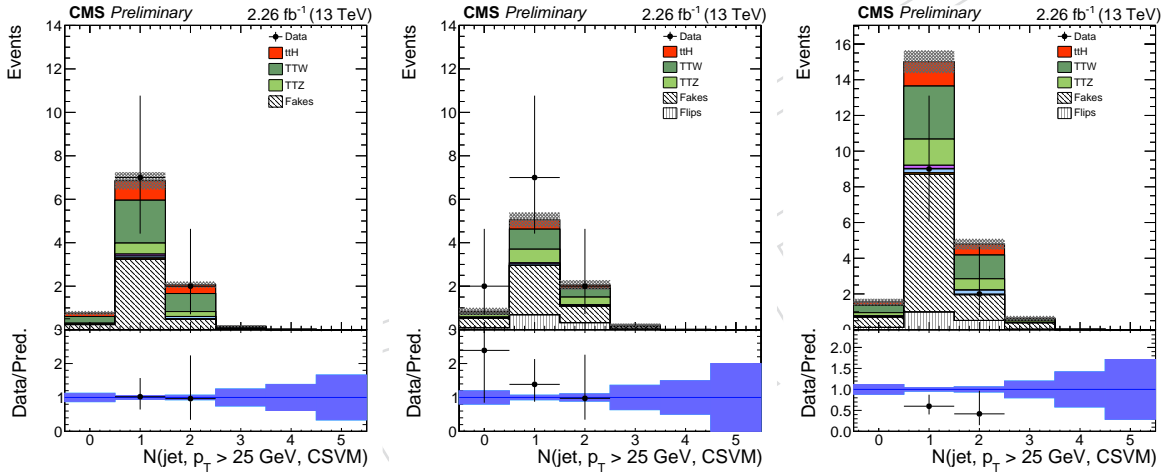


Figure 23: Multiplicity of jets passing the medium working point of the CSV tagger in the  $2\ell$  ( $\mu\mu$ ,  $ee$ ,  $e\mu$ ) selections.

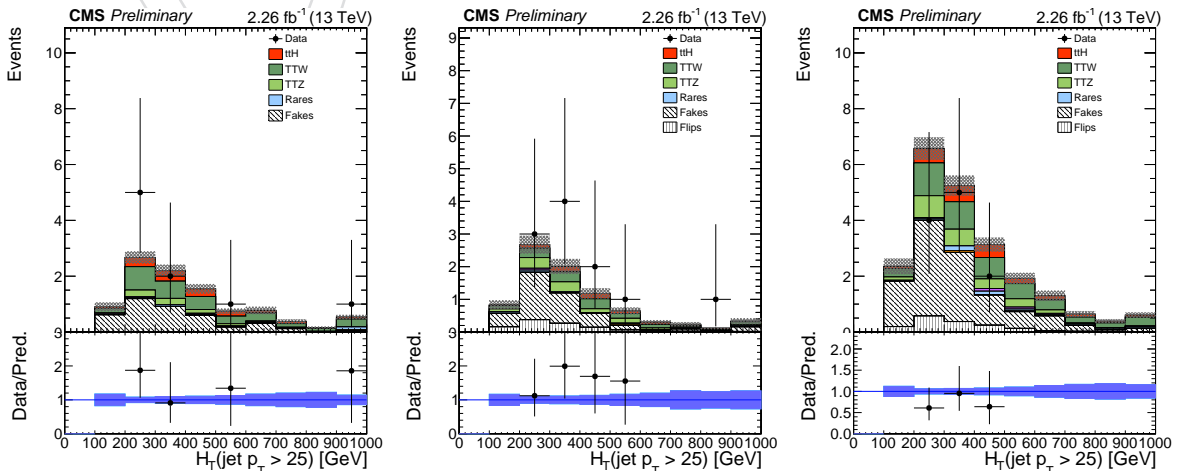
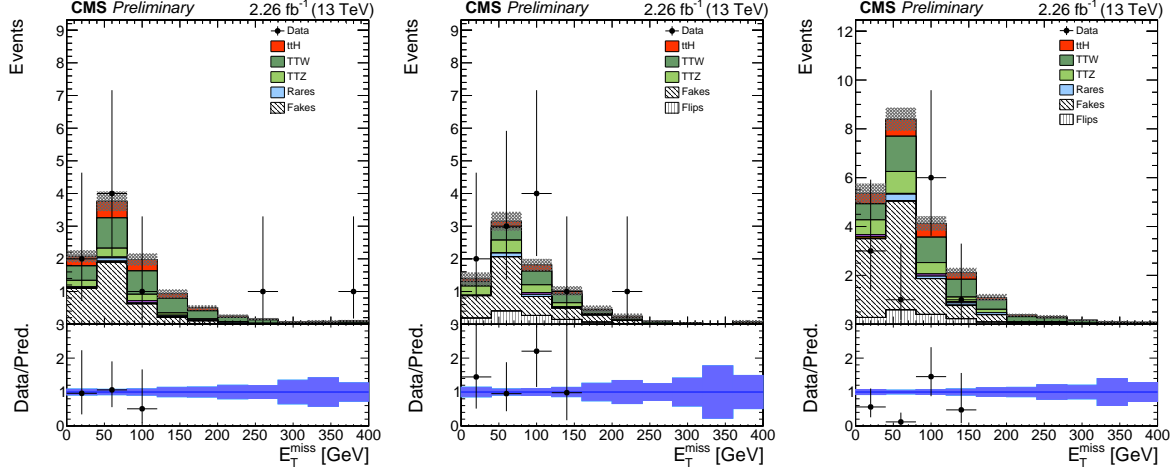
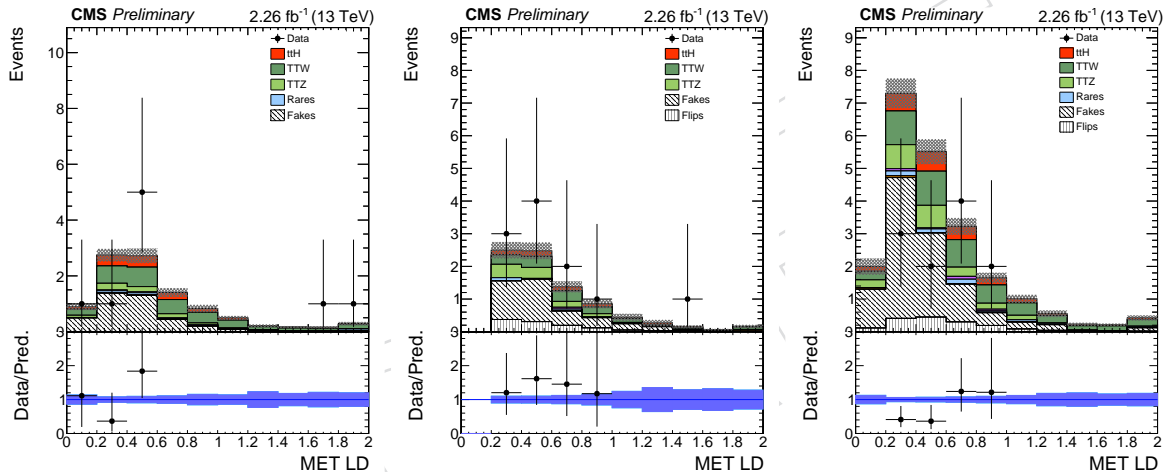
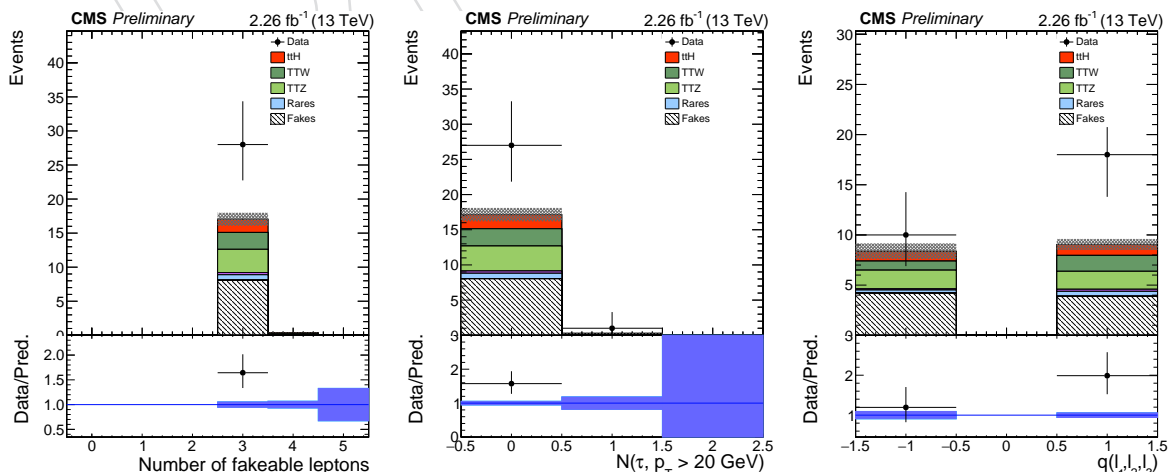
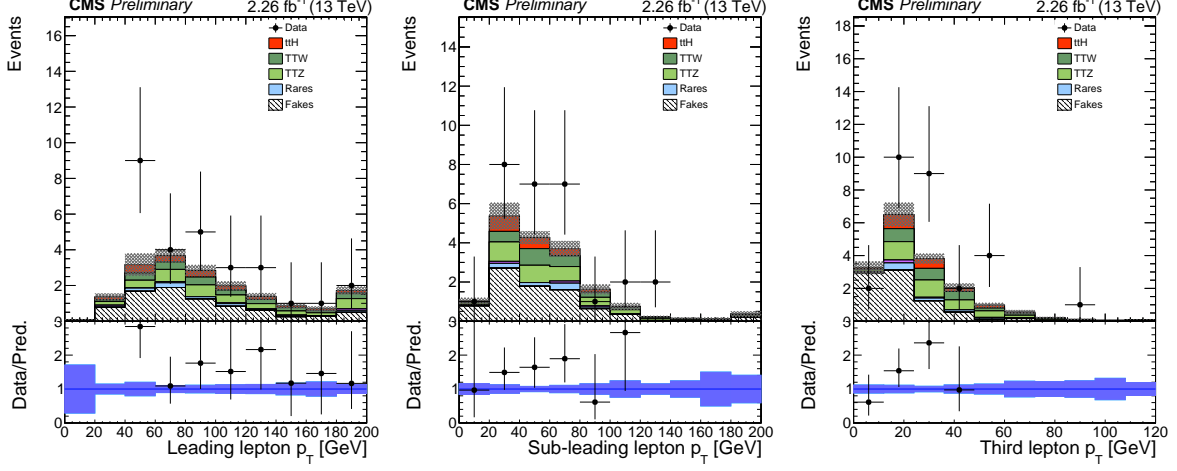
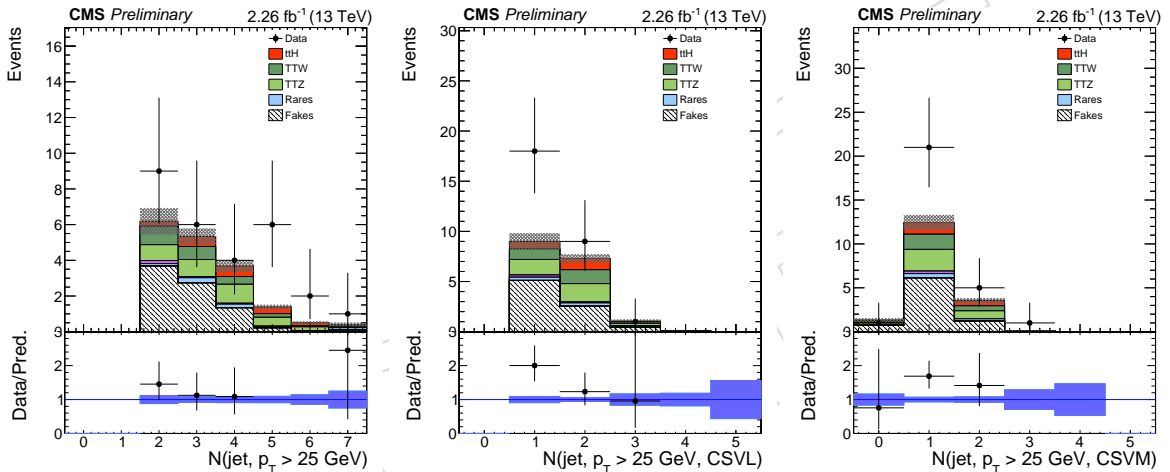
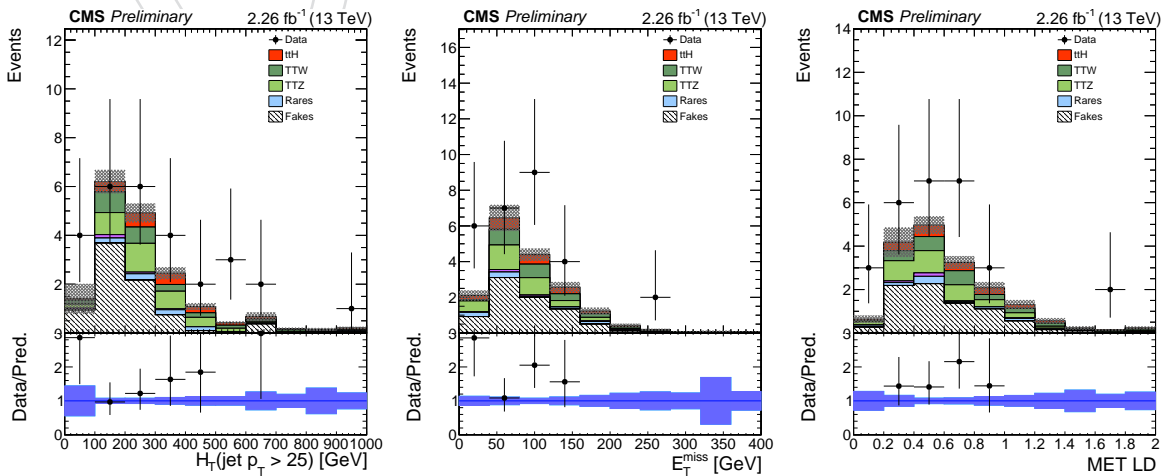


Figure 24:  $H_T$  spectra in the  $2\ell$  ( $\mu\mu$ ,  $ee$ ,  $e\mu$ ) selections.

Figure 25:  $E_T^{\text{miss}}$  spectra in the  $2\ell$  ( $\mu\mu$ ,  $ee$ ,  $e\mu$ ) selections.Figure 26:  $E_T^{\text{miss}} \text{LD}$  spectra in the  $2\ell$  ( $\mu\mu$ ,  $ee$ ,  $e\mu$ ) selections.Figure 27: Number and charge of leptons passing the fakeable object requirements and  $\tau_h$  leptons passing the requirements described in Section 3.5 in the  $3\ell$  selection.

Figure 28: Lepton transverse momentum spectra in the  $3\ell$  selection.Figure 29: Jet multiplicities (all jets, jets passing the loose working point of the CSV tagger, jets passing the medium working point of the CSV tagger) in the the  $3\ell$  selection.Figure 30:  $H_T$ ,  $E_T^{\text{miss}}$  and  $E_T^{\text{miss}} \text{LD}$  distributions in the  $3\ell$  selection.

## 405 5 Signal extraction

406 The number of events that pass the selection described in the previous section is not sufficient  
 407 to ascertain the presence of ttH signal solely from their multiplicity, as the total yields are still  
 408 dominated by the background. The approach adopted in this search is to split the selected  
 409 events into several mutually exclusive categories with different signal to background ratios. In  
 410 each of these categories the signal is extracted from the distribution of a suitable discriminating  
 411 variable.

412 In order to exploit the topological characteristics and specificities of the ttH signal with respect  
 413 to the most dominant backgrounds, the output of the boosted decision tree (BDT), trained using  
 414 a selection of kinematic variables, is taken as discriminating variable for the signal extraction.

415 Both final states with two same sign leptons (2lss) and at least three leptons ( $\geq 3l$ ) have dom-  
 416 inant backgrounds originating from the ttbar and ttV ( $V=W/Z$ ) processes. In order to have  
 417 an efficient discrimination against both of these processes, a two-dimensional (2D) BDT ap-  
 418 proach is introduced. For each of the 2lss and  $\geq 3l$  final states, the BDT is separately trained  
 419 against the ttbar and ttV, selecting in each training a set of kinematic variables that provide a  
 420 largest separation. The BDT outputs of the training against these two processes are used to  
 421 construct the 2D space, effectively as a scatter plot of the two discriminators. The consequent  
 422 2D distribution is then partitioned to rectangular sectors and ttH signal and background con-  
 423 tributions of each sector are summed and folded to the one-dimensional histogram in which  
 424 the bins are sorted by increasing background. With a convenient partitioning of the 2D space,  
 425 the resulting difference of the signal and background shapes is enhanced with respect to the  
 426 one-dimensional case, for example against the ttbar, and that is provided by the training of the  
 427 additional BDT, against the ttV process.

428 In the two same sign lepton category and for the training against the ttbar background, the  
 429 input variables are the following: the maximum absolute pseudorapidity of the two leading  
 430 leptons, the multiplicity of hadronic jets, the minimum distance between the leading lepton and  
 431 closest jet, the minimum distance of the trailing lepton and closest jet, the missing transverse  
 432 energy, the average separation between the two jets and the transverse mass of the leading  
 433 lepton and missing transverse energy. The training against the ttV process relies of the folowing  
 434 variables: the maximum absolute pseudorapidity of the two leading leptons, the transverse  
 435 mass of the leading lepton and missing transverse energy, the multiplicity of hadronic jets,  
 436 the minimum distance between the leading lepton and closest jet, the minimum distance of  
 437 the trailing lepton and closest jet, the leading lepton transverse momentum and the trailing  
 438 lepton transverse momentum. The training is performed using a relaxed event selection, that  
 439 require at least two preselected same sign leptons with leading and trailing lepton transverse  
 440 momentum larger than 20 and 10 GeV, respectively, then either two loose selected b-jets or  
 441 one medium b-tagged jet and also at least four jets in the event. Figures 31 and 32 show a  
 442 comparison of the simulated signal (ttH) and background (ttbar or ttV) processes for each of  
 443 the input variables to the BDT discriminator.

444 The at least three leptons category has the following variables for the training against the ttbar  
 445 background: the maximum absolute pseudorapidity of the two leading leptons, the transverse  
 446 mass of the leading lepton and missing transverse energy, the multiplicity of hadronic jets,  
 447 the missing HT, the average distance of the two jets, the minimum distance between the lead-  
 448 ing lepton and closest jet and the minimum distance of the trailing lepton and closest jet. For  
 449 the training against the ttV background, the input variables are: the maximum absolute pseu-  
 450 dorapidity of the two leading leptons, the transverse mass of the leading lepton and missing  
 451 transverse energy, the multiplicity of hadronic jets, the minimum distance between the leading

lepton and closest jet, the minimum distance of the trailing lepton and closest jet, the leading lepton transverse momentum and the third lepton transverse momentum.

Because the currently available Monte-Carlo statistics prevent us from training with the full event selection, a relaxed selection has been applied instead for training. This relaxed selection requires at least three preselected leptons where neither lepton pair has an invariant mass within 10 GeV of the mass of the Z boson, the leading, trailing and sub-trailing lepton transverse momentum larger than 20, 10 and 10 GeV, respectively, the MET LD requirement applied and at least two loose selected b-jets in the event. In the Figures 33 and 34, a comparison of the simulated signal (ttH) and background (ttbar or ttV) processes for each of the input variables to the BDT discriminator is presented.

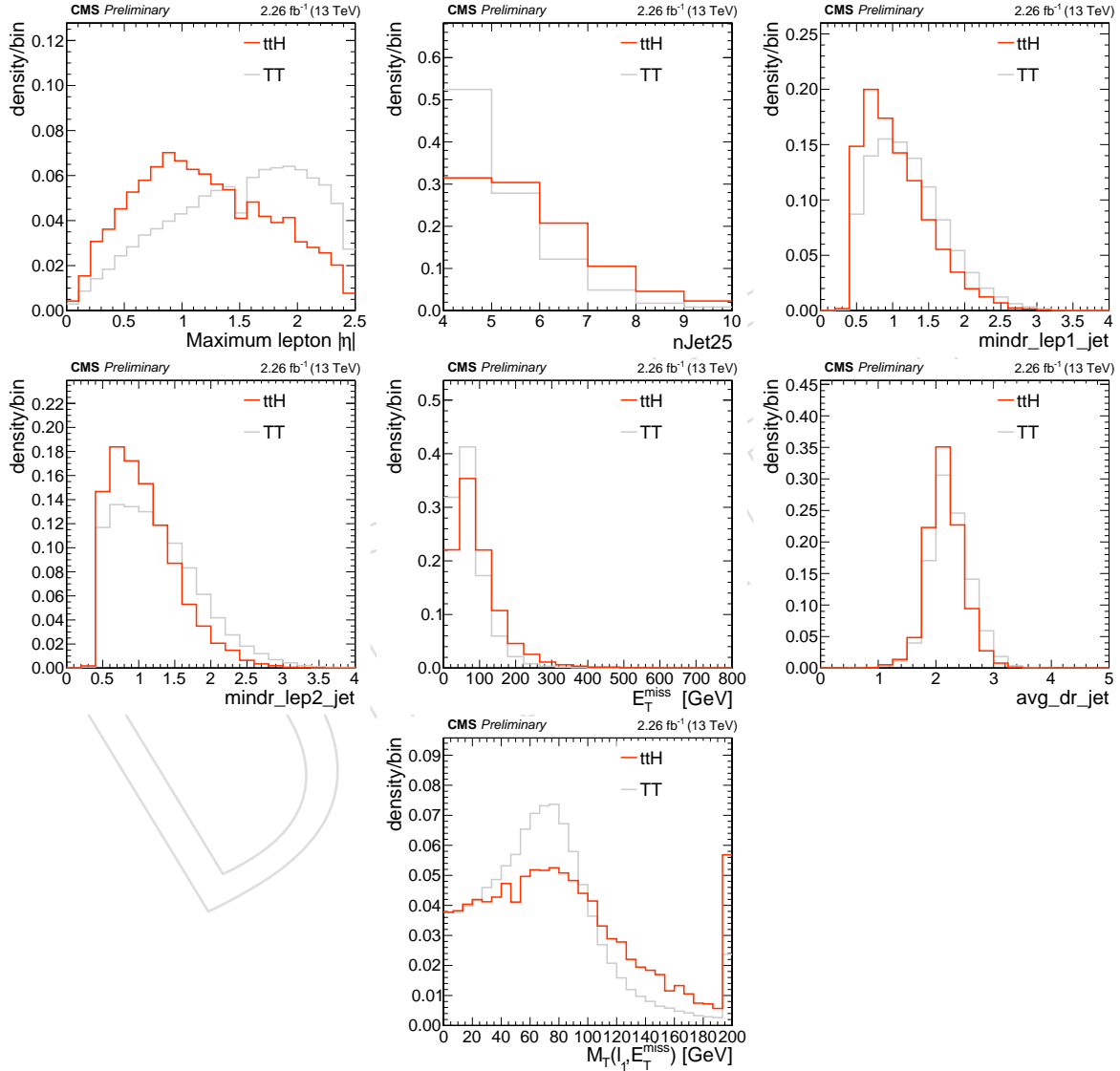


Figure 31: The separation power of the variables used for BDT training against the ttbar background, in the two same sign leptons channel.

The correlation matrices for signal and background processes, given in Figures 35 and 36, show generally low correlation between the input variables for each of the two same sign and three lepton channels.

Figures 37 and 38 show the separation power of each of the BDT discriminators, while Fig-

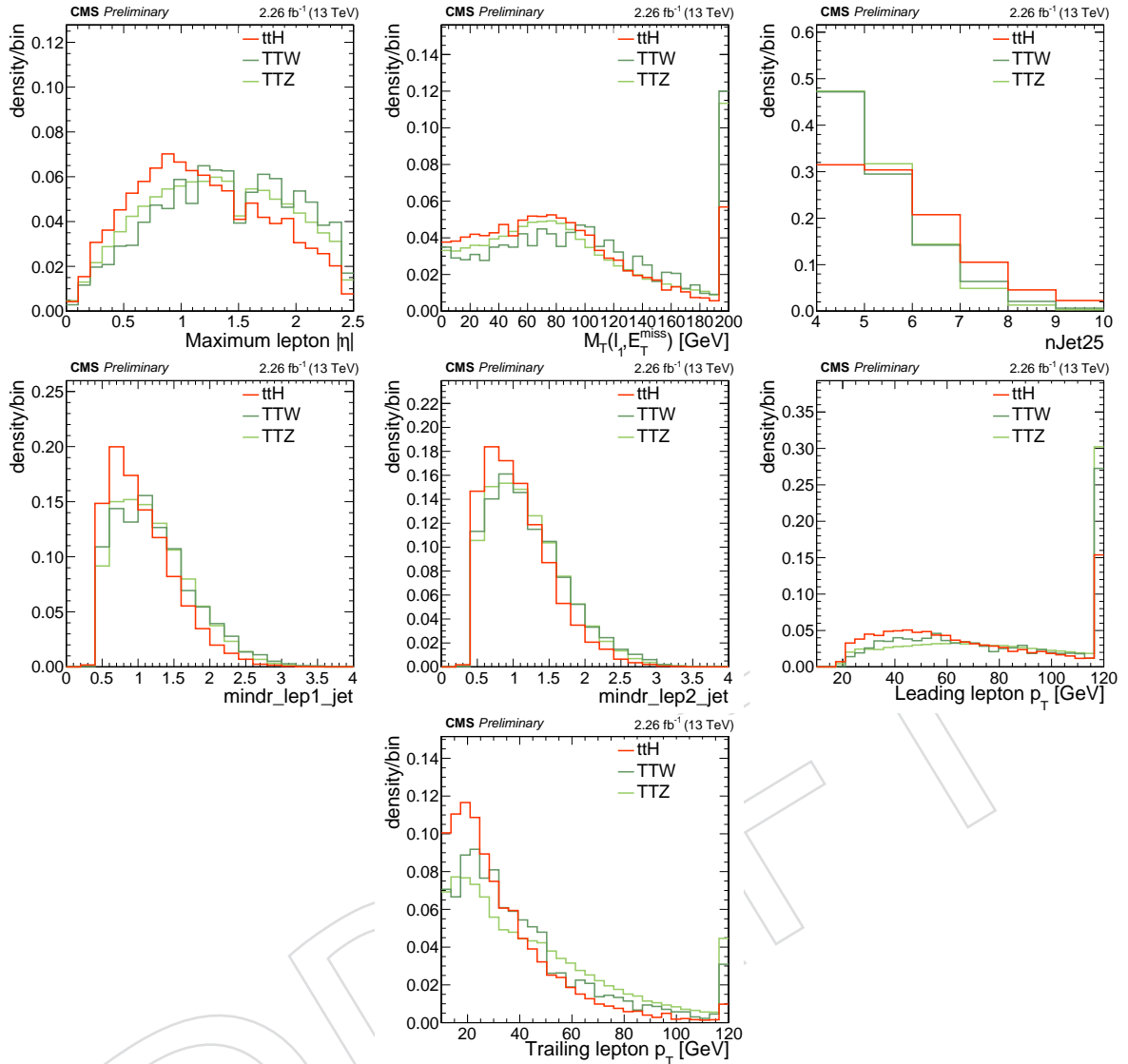


Figure 32: The separation power of the variables used for BDT training against the ttV background, in the two same sign leptons channel.

466 ures 39 and 40 show the distributions of these discriminators in MC events.

467 The 2D plane spanned by the output of the two discriminators is binned in order to maximize  
468 the analysis sensitivity with the available statistics. Partitioning the 2D plane in six bins such  
469 that in each bin there is an approximately equal number of signal events, results with a flattened  
470 signal distribution in the resulting one-dimensional histogram, as shown in Figure 41. This  
471 implies that the shape of the background distribution is substantially different from the signal  
472 shape and that is dominantly due to the bin 6 that is selected to have a highest occupancy. A  
473 further extension of the bin 6 in the 2D plane, while still keeping the signal shape relatively  
474 flat, maximizes the shape difference with this approach and improves the signal sensitivity in  
475 terms of the expected limits, as it will be shown in Chapter 8. The binning of the 2D plane is  
476 specified in the Table 16.

477 Figure 41 shows the event yield as a function of the bins defined above.

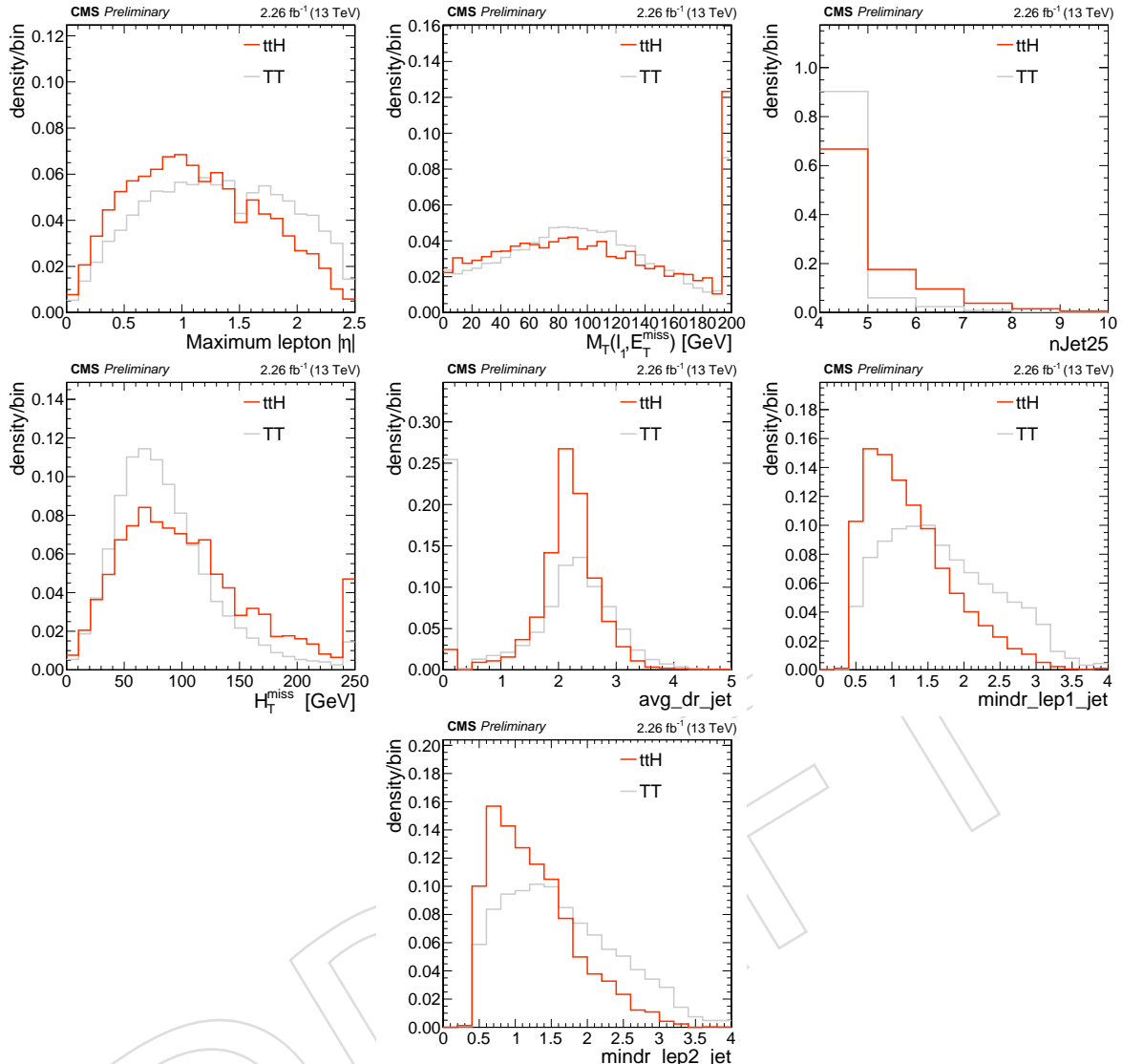


Figure 33: The separation power of the variables used for BDT training against the  $t\bar{t}$  background, in the three lepton channel.

## 478 5.1 Event subcategories

- 479 The two same sign lepton events are further divided into categories with zero or at least one  
 480 hadronic taus, as described in Section 3.3. The category with zero taus is split into lepton  
 481 flavours: two electrons, two muons and electron and muon. These three categories, except  
 482 the two electrons, are further divided according to the presence (or absence) of two medium  
 483 tagged b-jets, the b-tight (b-loose) categories. Due to a low expected yield, the events with at  
 484 least one hadronic taus are not split by flavour or b-tag and are considered inclusively.  
 485 The events with at least three leptons are taken inclusively in terms of the requirement on the  
 486 presence of hadronic taus and are only separated into the b-tight and b-loose categories.  
 487 At last, events in each of the categories are separated by positive or negative sum of charges  
 488 of the leptons. In this way, the charge asymmetry present in several backgrounds ( $t\bar{t}W$ ,  $WZ$ ,  
 489 single top and  $W+jets$ ) with respect to the ttH signal process is taken into account.

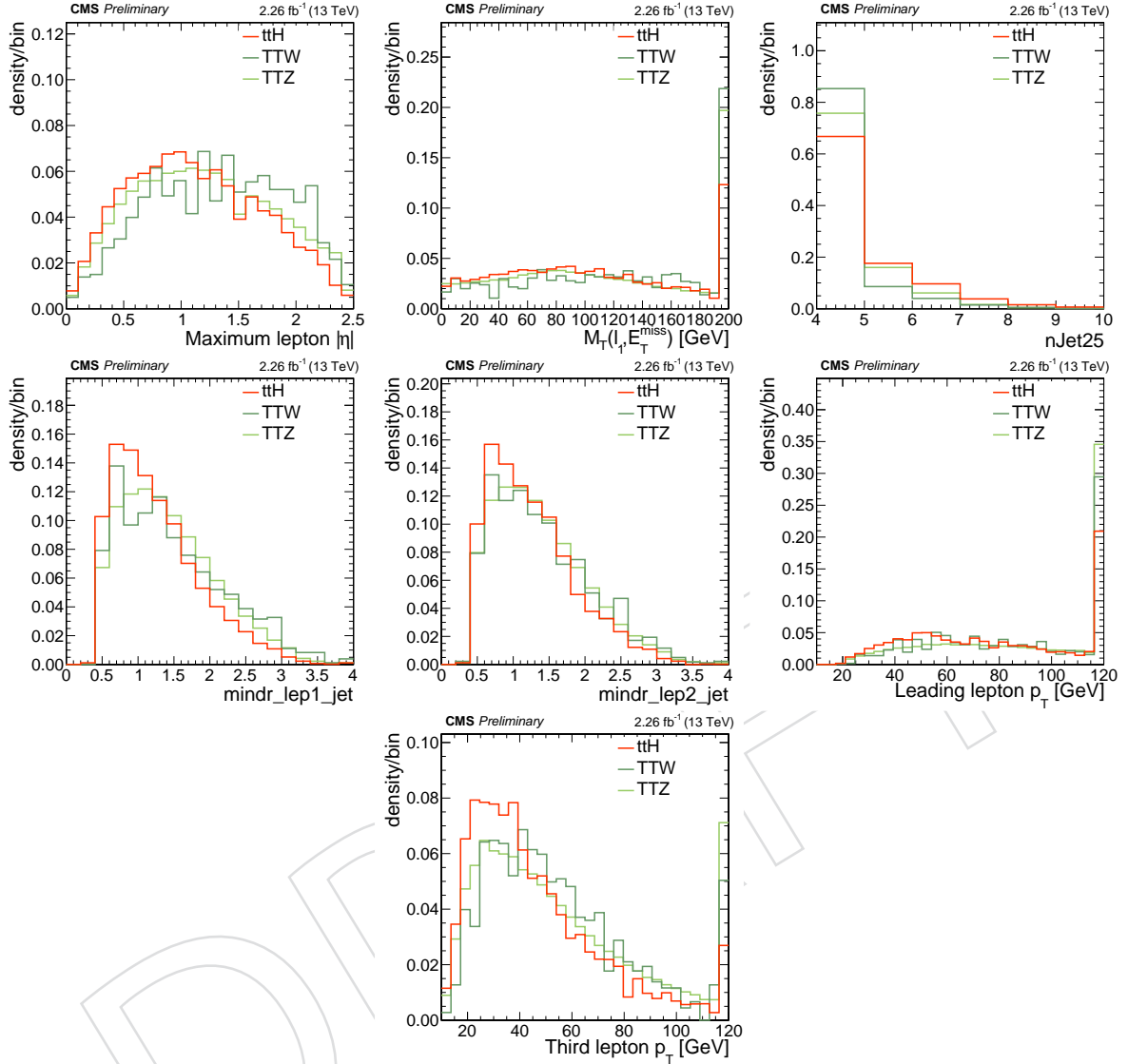


Figure 34: The separation power of the variables used for BDT training against the ttV background, in the three lepton channel.

Table 16: Coordinates of the bins that represent the partitioning of the 2D BDT plane.

|                | bin 1        | bin 2        | bin 3        | bin 4       | bin 5        | bin 6       |
|----------------|--------------|--------------|--------------|-------------|--------------|-------------|
| $2lss(ttbar)$  | (-1.0, -0.2] | (-1.0, -0.2] | (-0.2, 0.3]  | (-0.2, 0.3] | (0.3, 1.0]   | (0.3, 1.0]  |
| $2lss(ttV)$    | (-1.0, -0.1] | (-0.1, 1.0]  | (-1.0, -0.1] | (-0.1, 1.0] | (-1.0, -0.1] | (-0.1, 1.0] |
| $3\ell(ttbar)$ | (-1.0, 0.3]  | rest         |              | (0.3, 1.0]  |              |             |
| $3\ell(ttV)$   | (-1.0, -0.1] | rest         |              | (-0.1, 1.0] |              |             |

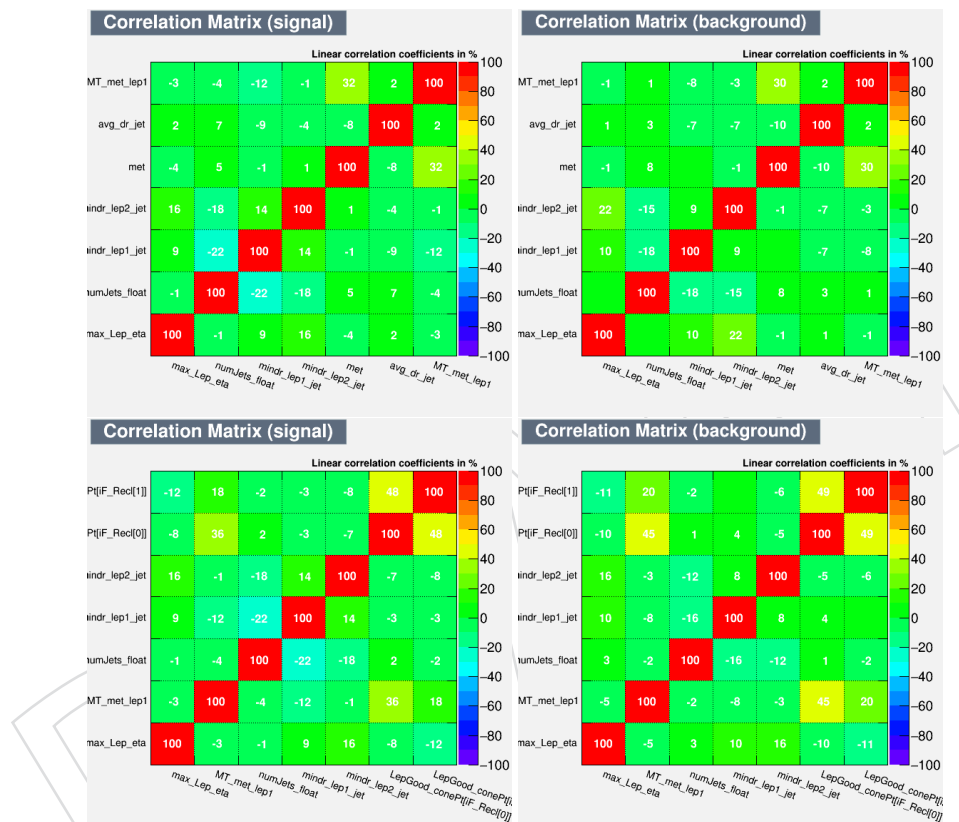


Figure 35: The correlations between the input variables in the two same sign lepton channel, given for signal (left) and background (right) in the case of training against the ttbar (upper) and ttV (lower) processes.

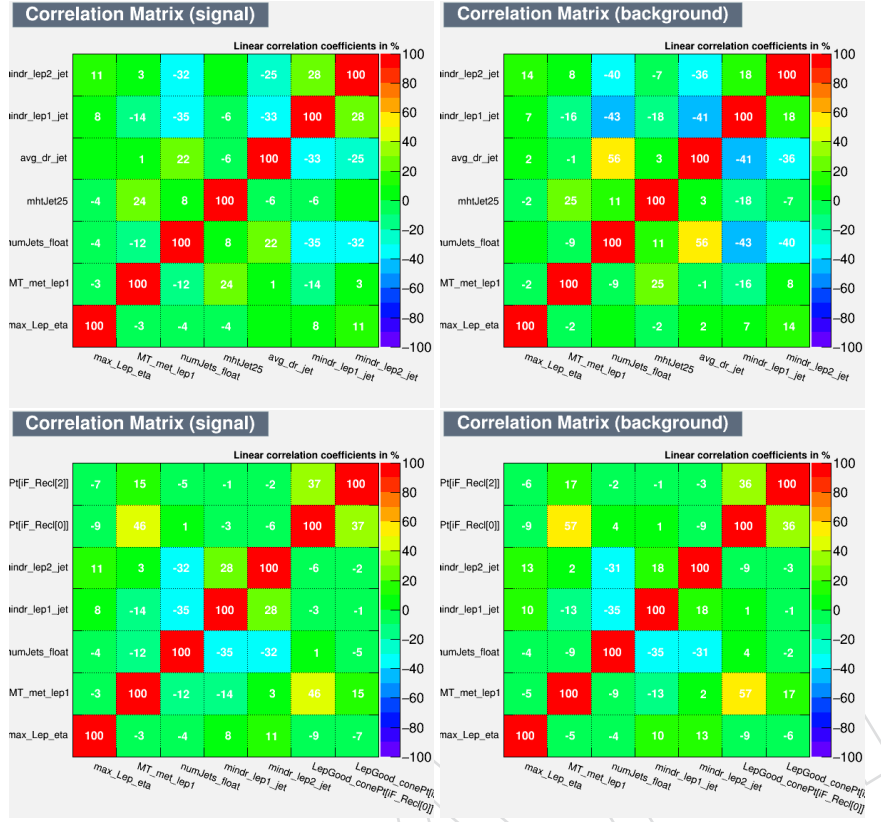


Figure 36: The correlations between the input variables in the three lepton channel, given for signal (left) and background (right) in the case of training against the ttbar (upper) and ttV (lower) processes.

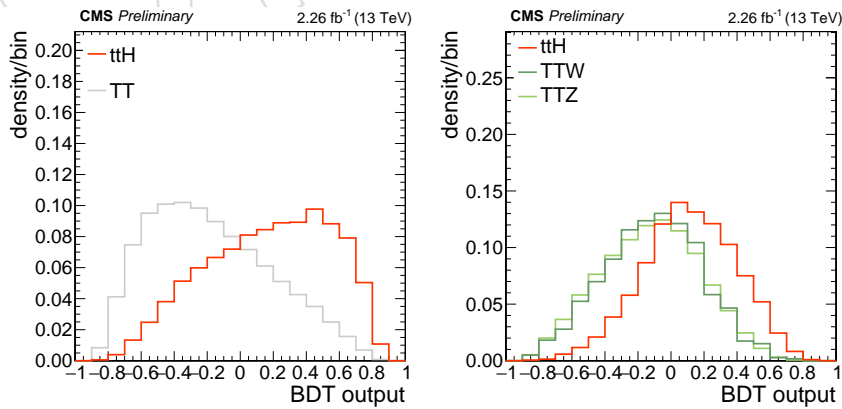


Figure 37: The separation power of the BDT output against the ttbar (left) and ttV (right) background, in the two same sign leptons channel.

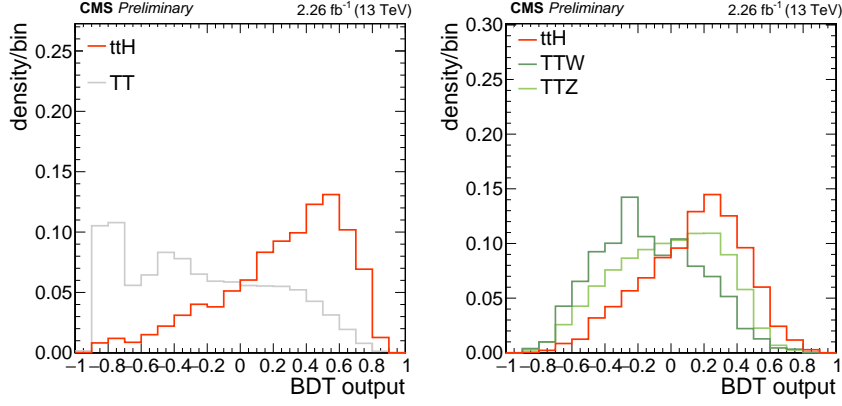


Figure 38: The separation power of the BDT output against the ttbar (left) and ttV (right) background, in the three lepton channel.

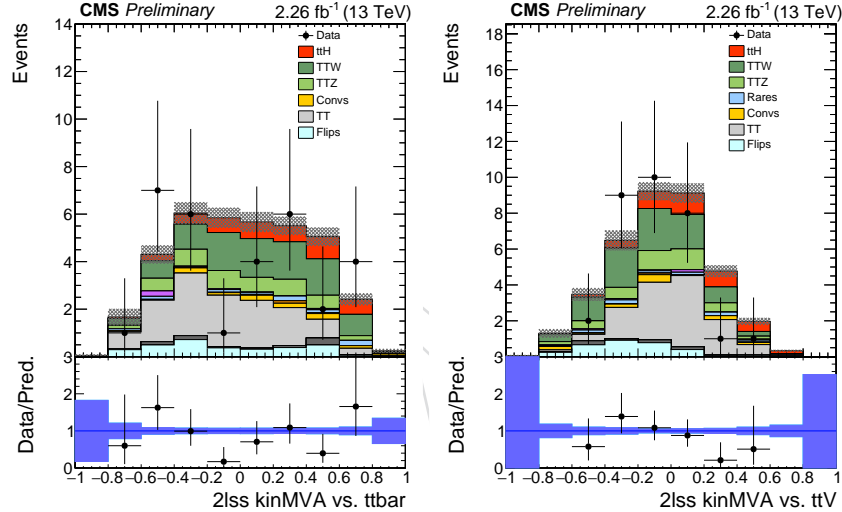


Figure 39: Distribution of the discriminator against the ttbar (left) and ttV (right) backgrounds, in the two same sign leptons channel.

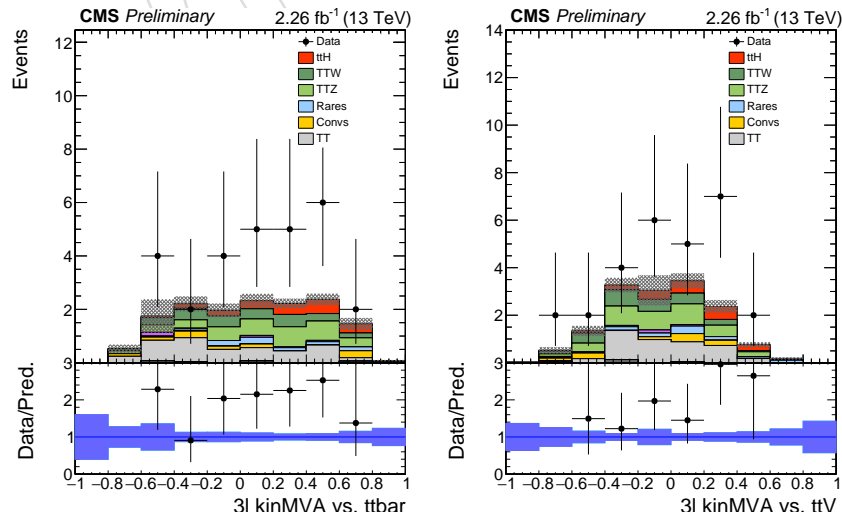


Figure 40: Distribution of the discriminator against the ttbar (left) and ttV (right) backgrounds, in the three lepton channel.

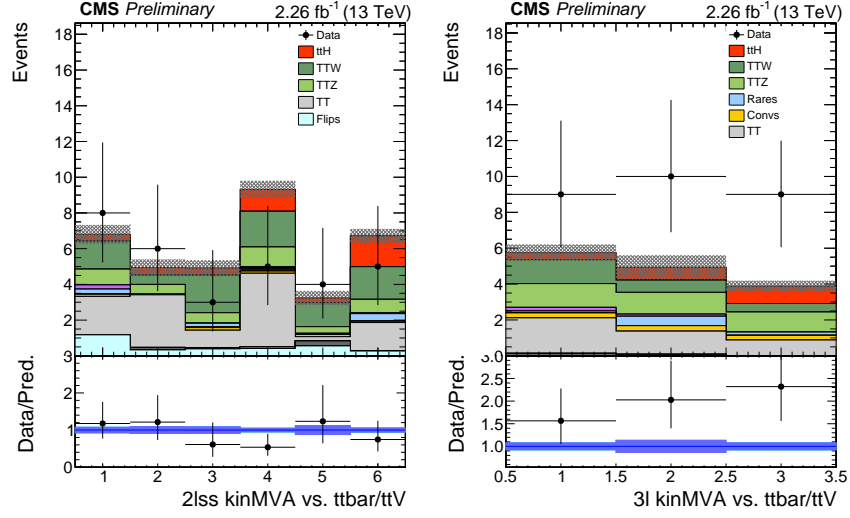


Figure 41: Binned distributions of the pair of discriminators against the  $t\bar{t}\bar{b}$  (left) and  $t\bar{t}V$  (right) backgrounds.

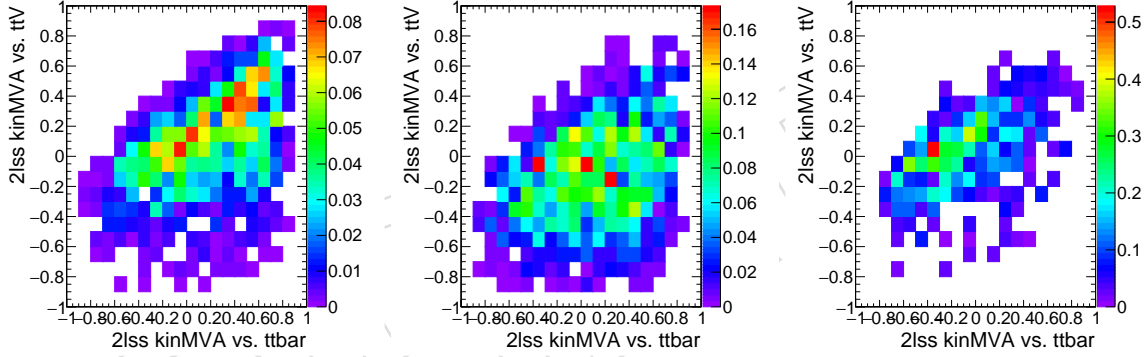


Figure 42: Unbinned distributions of the pair of discriminators for  $t\bar{t}H$  (left),  $t\bar{t}W$  (center),  $t\bar{t}bar$  (right) in  $2lss$ .

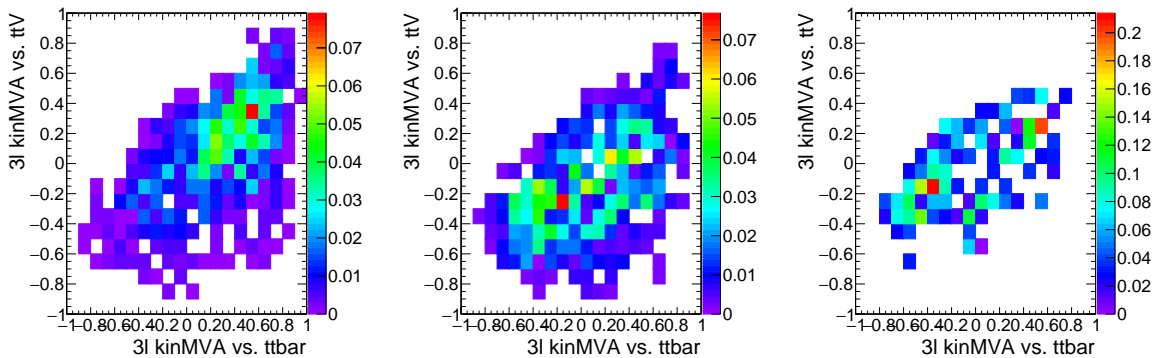


Figure 43: Unbinned distributions of the pair of discriminators for  $t\bar{t}H$  (left),  $t\bar{t}W$  (center),  $t\bar{t}bar$  (right) in  $3l$ .

## 490 6 Signal modeling

491 The signal is modelled using simulated events. The simulation has two different sources of  
 492 systematic uncertainty. The first source of uncertainty is correction factors applied to the simula-  
 493 tion in order to better reproduce the detector conditions and performance in data. The second  
 494 source is assumptions made in the theoretical models that were used to produce the simulation.  
 495 We account for uncertainties from both sources.

### 496 6.1 Correction factors and experimental uncertainties

497 As discussed in Section 3, we use scale factors to correct for differences in lepton performance  
 498 between data and simulation. The scale factors account for the differences in the trigger, lepton  
 499 Loose and Tight selections. Each of these scale factors has an uncertainty associated with it as  
 500 discussed in that section, and it's propagated in the final uncertainties on signal yields.

501

502 The corrections that we apply to jet energies in simulation have uncertainties associated with  
 503 them [19]. The uncertainties are parameterised as a function of  $p_T$ ,  $\eta$ . We assess the impact of  
 504 the uncertainties by shifting the jet energy correction factors for each jet up and down by  $\pm 1\sigma$   
 505 and re-calculating all kinematic quantities. The effect on the shape of the BDT discriminators  
 506 used in the signal extraction is shown in Fig. 44. Systematics effect both on normalization and  
 507 shape are taken into account in extracting the results.

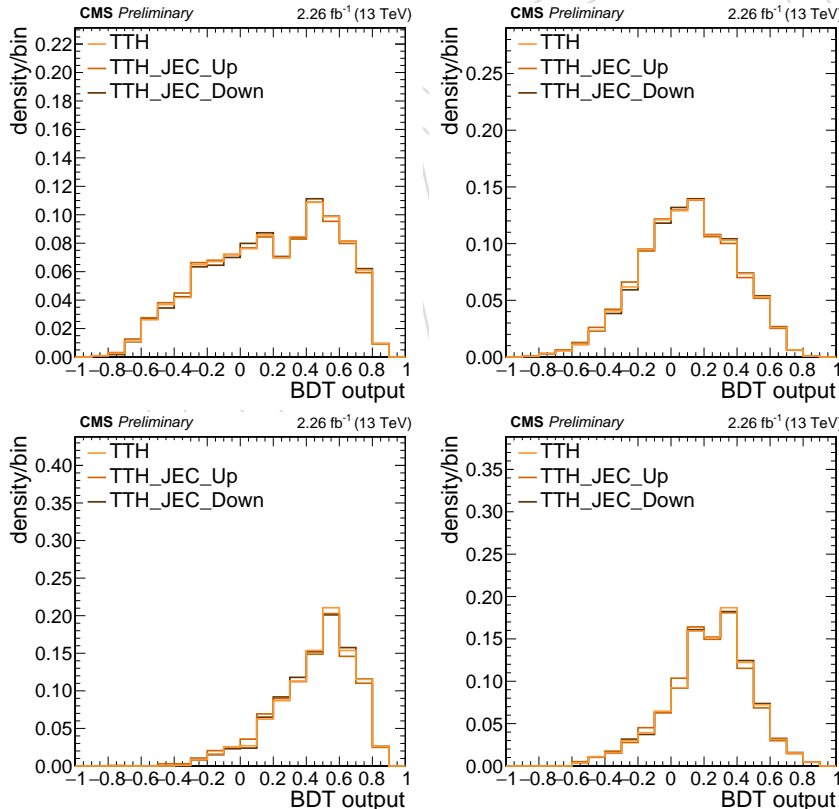


Figure 44: The BDT output distribution of the ttH signal, shown for the training against  $t\bar{t}b\bar{b}$  (left) and  $t\bar{t}V$  (right) in the two same sign leptons (upper) and three lepton (lower) final state, with the jet energy scale variations of one standard deviation included in order to estimate the shape uncertainties.

508 In the RunI analysis we found that the uncertainty from the jet energy resolution plays a negli-

509 gible role in this analysis.

510 The uncertainties on the correction for the data/sim differences in the b-tagging performance  
 511 described in 3 are parameterised as a function of  $p_T$ ,  $\eta$ , and flavor of the jet. We assess their  
 512 effect on the analysis by shifting the weight of each jet up and down by  $\pm 1\sigma$  of the appropriate  
 513 uncertainty and we recalculate the overall event weight.

## 514 6.2 Theoretical uncertainties

515 The theoretical uncertainties on the NLO prediction for the inclusive  $t\bar{t}H$  production cross sec-  
 516 tion amount to  $+5.8\text{--}9.2\%$  from unknown higher orders in the perturbative series and  $3.6\%$   
 517 from the knowledge of the parton distribution functions (PDFs) and  $\alpha_s$  [29]. These uncertain-  
 518 ties are propagated to the final normalization of the signal yields.

519 In addition to the overall normalisation, systematic uncertainties of theoretical origin on the  
 520 distribution of the events in the final discriminating variables are considered, estimated con-  
 521 ventionally by varying the normalisation and factorisation scales up and down by a factor two  
 522 and matching threshold between matrix element and parton shower (Fig. 45). In the current  
 523 version of the results the shape uncertainties on the BDTs output are of the order of 2% to 3%.

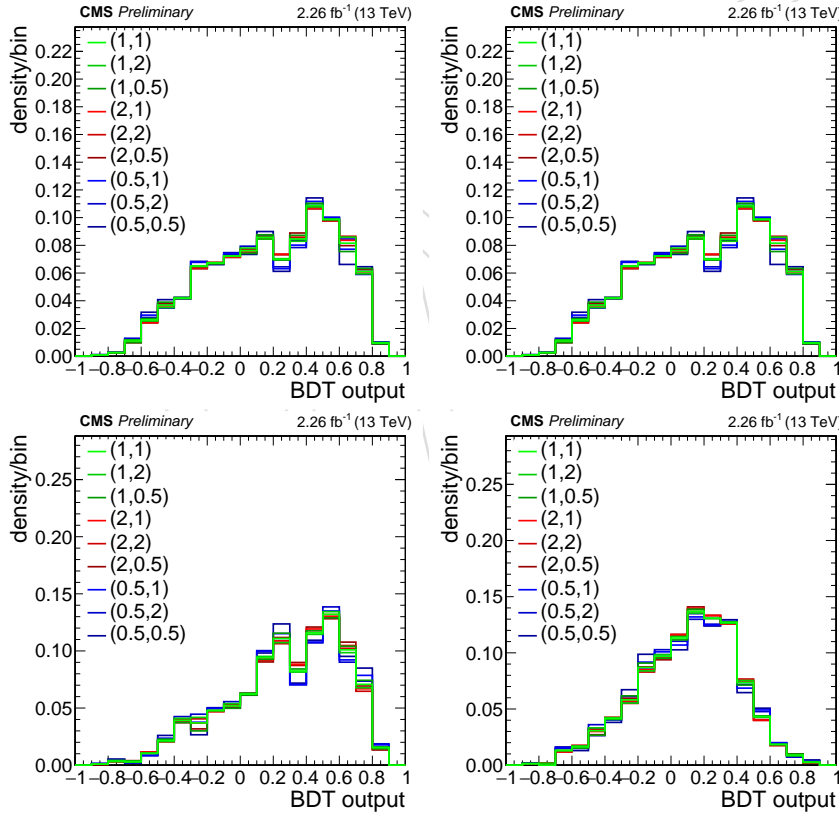


Figure 45: The BDT output distribution of the  $ttH$  signal, shown for the training against  $tt\bar{b}$   
 (left) and  $ttV$  (right) in the two same sign leptons (upper) and three lepton (lower) final state,  
 with variations of the renormalization and factorization scale included in order to estimate the  
 shape uncertainties.

## 524 7 Background predictions

### 525 7.1 Irreducible backgrounds

526 Irreducible backgrounds from  $t\bar{t}W$ ,  $t\bar{t}Z$  and  $t\bar{t}WW$ , are estimated from simulated events. Just  
 527 like for the signal, corrections are applied for the different performance the individual physics  
 528 objects between data and simulation measured in control regions in data. The effect of the JEC  
 529 uncertainties on the final discriminator shapes is shown for  $t\bar{t}W$ ,  $t\bar{t}Z$  in Fig. 46 and Fig. 47.

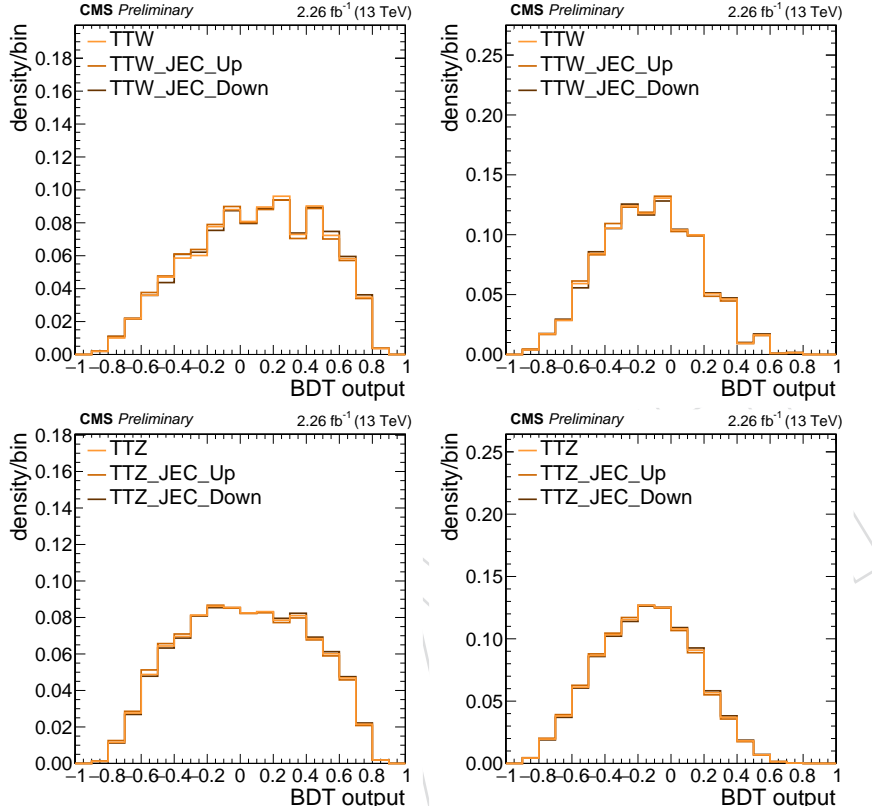


Figure 46: The BDT output distribution of the  $t\bar{t}W$  and  $t\bar{t}Z$ , shown for the training against  $t\bar{t}b\bar{b}$  (left) and  $t\bar{t}V$  (right) in the two same sign leptons final state, with the jet energy scale variations of one standard deviation included in order to estimate the shape uncertainties.

530 In the RunI analysis, the contribution of the  $t\bar{t}WW$  process was found to be at least an order of  
 531 magnitude smaller than  $t\bar{t}W$  and  $t\bar{t}Z$ . At 13 TeV, NLO (arXiv 1405.0301 table 6), the cross section  
 532 is a factor 5 higher than what we had at 8 TeV (partially because of the  $k$  factor as at 8 TeV we  
 533 only had LO, and 13 TeV NLO/LO 1.5). Therefore if it was negligible at 8 TeV it still is.

534 The inclusive production cross sections for the  $t\bar{t}W$  and  $t\bar{t}Z$  processes are taken from the latest  
 535 NLO computation, with theoretical uncertainties from unknown higher orders of 12% and 10%  
 536 respectively, and uncertainties from the knowledge of the parton density functions and  $\alpha_s$  of  
 537 2% and 3% respectively [29].

538 In addition to the overall normalisation, systematic uncertainties of theoretical origin on the  
 539 distribution of the events in the final discriminating variables are considered, estimated con-  
 540 ventionally by varying the normalisation and factorisation scales up and down by a factor two  
 541 and matching threshold between matrix element and parton shower. These results are shown  
 542 both for  $t\bar{t}W$  and  $t\bar{t}Z$  in Fig. 48 and 49. In the current version of the results the shape uncertain-  
 543 ties on the BDTs output are of the order of 2% to 4%.

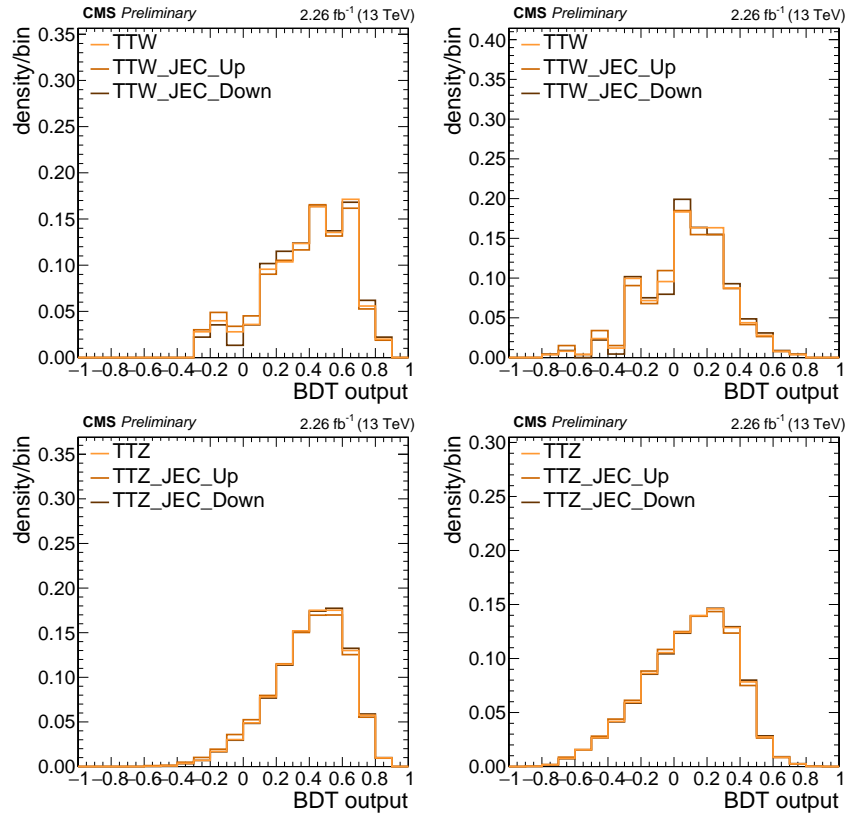


Figure 47: The BDT output distribution of the ttW and ttZ, shown for the training against ttbar (left) and ttV (right) in the three lepton final state, with the jet energy scale variations of one standard deviation included in order to estimate the shape uncertainties.

544 The cross section for the  $t\bar{t}\gamma^*$  process with  $\gamma^* \rightarrow \ell^+\ell^-$  process becomes large for decreasing  
 545 virtuality of the  $\gamma^*$ , i.e. for small invariant masses of the dilepton pair. While in the analysis  
 546 we reject events with low mass dileptons, the  $t\bar{t}\gamma^*$  process can still contribute as a background  
 547 when one of the two leptons is not reconstructed; this in particular can happen in kinematic  
 548 configurations where the conversion is very asymmetric and one of the two leptons has trans-  
 549 verse momentum below the acceptance.

550 Since the nominal ttZ MC sample is generated with the requirement  $m_{\ell^+\ell^-} > 10$  GeV, to es-  
 551 timate this background we rely on an additional  $t\bar{t}\gamma^*$  MC sample generated in the remaining  
 552 part of the phase space. This additional sample is generated with LO MADGRAPH, and the  
 553 details of the generation and normalization can be find here [30].

554 In the case of electrons, in addition to the  $t\bar{t}\gamma^*$  background there is a similar topology of events  
 555 from  $t\bar{t}\gamma$  production where the photon converts early in the detector material, one conversion  
 556 electron is not reconstructed and the remaining can then be misidentified as prompt electron<sup>1</sup>.  
 557 This background, despite being reducible, is not covered by the reducible background esti-  
 558 mation obtained extrapolating from leptons failing the MVA requirement, described later in  
 559 section 7.4, since the electron arising from the converted photon will be isolated, unlike non-  
 560 prompt electrons from hadron decays or misidentified charged hadrons. We therefore rely on  
 561 simulations normalized to NLO QCD cross section from Madgraph5\_aMC@NLO.  
 562

563 In addition to the experimental uncertainties, we assign a systematical uncertainty of 30% to the

<sup>1</sup>If both electrons are reconstructed, then the conversion veto applied in the electron selection will reject both.

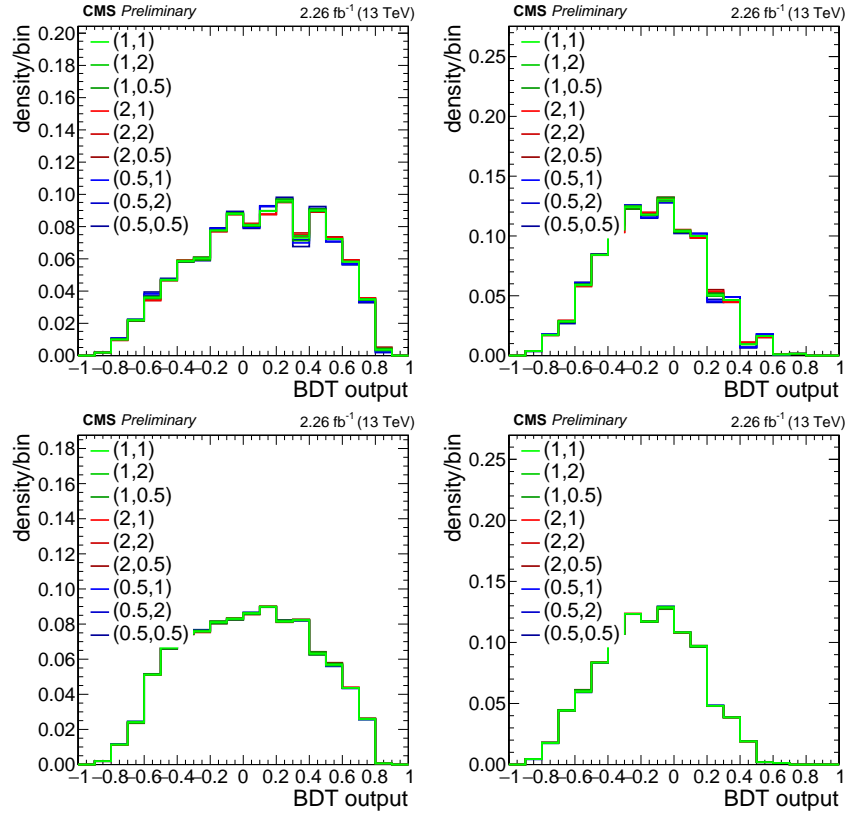


Figure 48: The BDT output distribution of the ttW and ttZ, shown for the training against ttbar (left) and ttV (right) in the two same sign leptons final state, with variations of the renormalization and factorization scale included in order to estimate the shape uncertainties.

564 overall normalization of  $t\bar{t}\gamma$  and a systematical uncertainty of 50% on the overall normalization  
 565 of  $t\bar{t}\gamma^*$ .

## 566 7.2 Di-bosons backgrounds

567 WZ and ZZ production with the gauge boson decaying to electrons, muons or taus can yield  
 568 the same leptonic final states as the signal, if considering also events where not all leptons  
 569 are identified. While the ZZ background is greatly reduced by the cut on MET LD, the WZ  
 570 background remains an important contribution to the three and more leptons signal region.

571 When not requiring additional hadronic jets in the final states, these processes are predicted  
 572 theoretically at NLO accuracy, and the inclusive cross sections have been successfully mea-  
 573 sured at the LHC. However these good agreement does not translate automatically to the signal  
 574 regions used in this search, which always require the presence of at least one b-tagged jet.

575 Since dibosons are preferentially produced in association with jets from light quarks or glu-  
 576 ons, it is possible to isolate a clean control region of WZ plus hadronic jets by inverting the  
 577 b-tagging requirements of the signal region and also inverting the  $Z \rightarrow ll$  veto. The approach  
 578 chosen for estimating the background is therefore to use simulated events but normalizing the  
 579 overall event yields in control regions of WZ plus two not b-tagged jets. This reduces the sys-  
 580 tematic uncertainty on the prediction, since the theoretical uncertainty on the ratio of event  
 581 yields between signal region and control region is much smaller than the uncertainty on the  
 582 production cross section of diboson plus multijet. The majority of events from this background  
 583 in the signal region contain jets from gluons or light quarks mistagged as b-jets, for which the

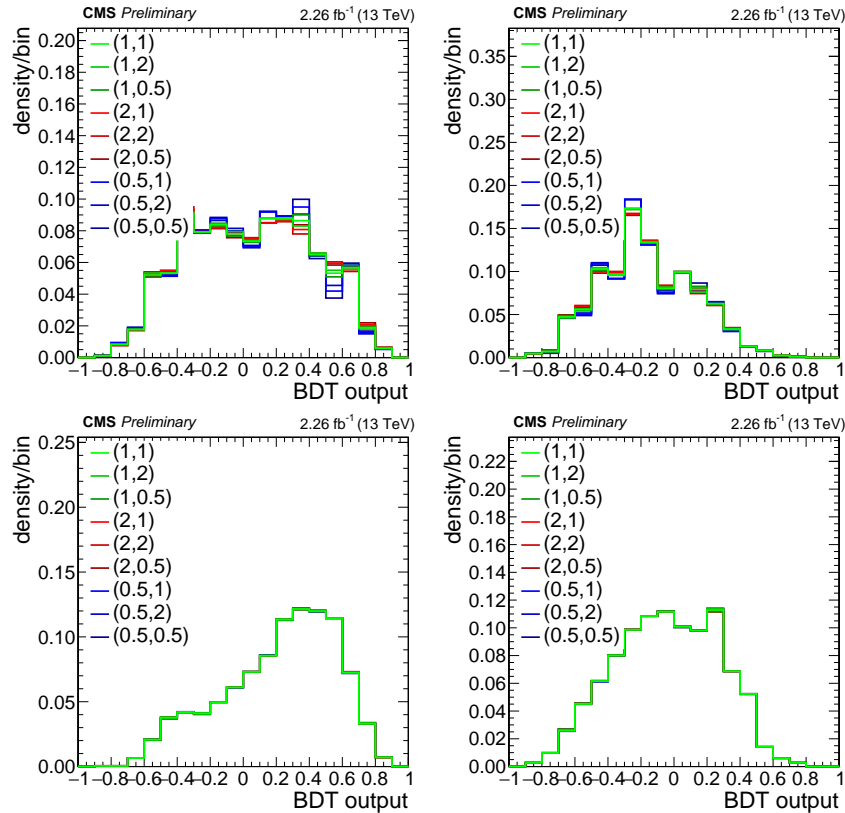


Figure 49: The BDT output distribution of the ttW and ttZ, shown for the training against ttbar (left) and ttV (right) in the three lepton final state, with the variations of the renormalization and factorization scale included in order to estimate the shape uncertainties.

584 extrapolation is affected only by uncertainties of experimental origin.

### 585 7.2.1 Measurement in data from events with no b-jets

586 The extraction of the WZ yield in the control region is performed via a one dimensional neg-  
 587 ative log likelihood fit of the shape of transverse mass of the lepton not associated to the Z  
 588 boson. The shape and normalization of the residual backgrounds are fixed to the expectations  
 589 from simulations. Table 17 shows the number of fitted events. The first uncertainty is from the  
 590 fit whereas the second one is obtained varying residual background contributions by  $\pm 100$   
 591 %.

Table 17: Estimated and observed number of events in the di-bosons control region

| Number of fitted WZ events |
|----------------------------|
| $10 \pm 3 \pm 2$           |

592 Figures 50, 51, 52 and 53 (*we are updating these figures with the results described in the text, ob-*  
 593 *tained with 76X*) show the good agreement observed in the WZ control region for the following  
 594 distributions:

- 595 •  $m_T W(l)$
- 596 •  $E_T^{\text{miss}} \text{ LD}$
- 597 • selected jet multiplicity
- 598 • sum of lepton charges

- 599     • invariant mass of the selected leptons  
 600     • vectorial sum of the transverse momenta of selected leptons  
 601     • reconstructed Z invariant mass  
 602     • transverse momentum of the reconstructed Z boson

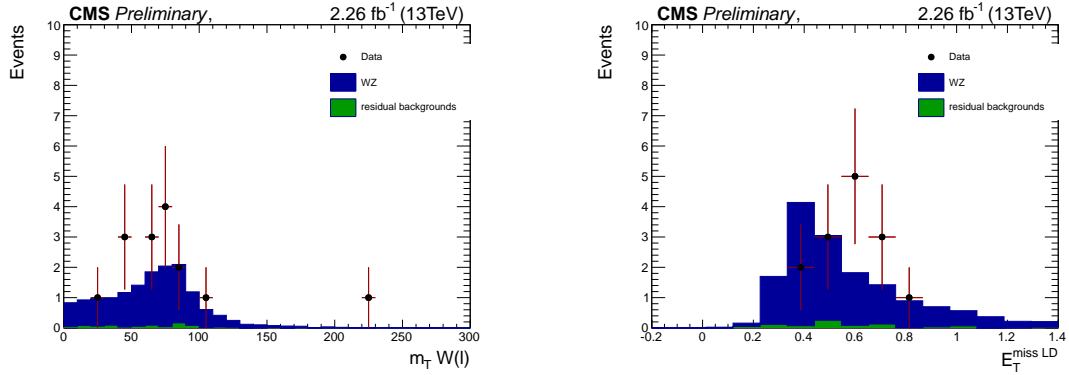


Figure 50: Distribution of the transverse mass of the lepton not associated to the reconstructed Z boson,  $m_T(l)$ , (left) and transverse missing energy,  $met_{LD}$ , (right) after a fit of the WZ and background processes to the data.

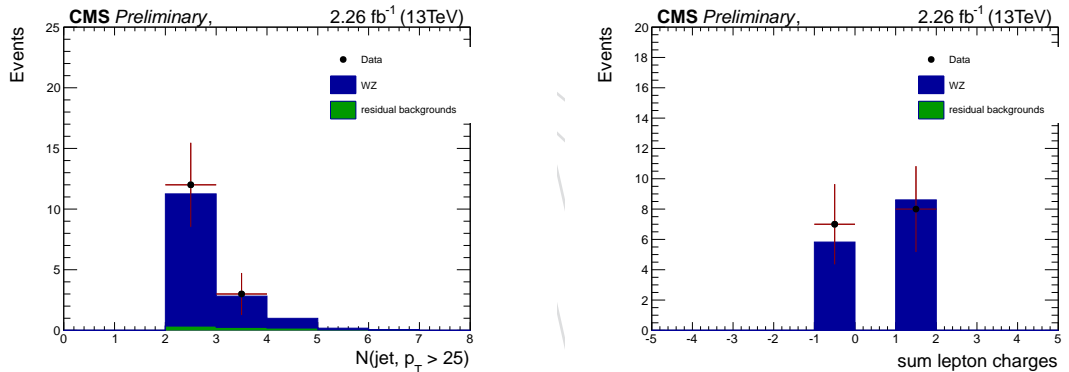


Figure 51: Distribution of the jet multiplicity (left) and sum of the leptons charges (right) after a fit of the WZ and background processes to the data

### 603 7.2.2 Extrapolation to events with b-jets

604 The ratio of the events yields between signal region and control region is measured in the  
 605 simulation. The main systematics are expected to come from the b-tagging scale factors since  
 606 most of the WZ plus two b-jets events are due to mistags:

$$\text{SR-b-loose/CR} : 0.0371 \pm 0.0041 \text{ (b-tagging)} \pm 0.0028 \text{ (theory)}$$

$$\text{SR-b-tight/CR} : 0.0015 \pm 0.0006 \text{ (b-tagging)} \pm 0.0001 \text{ (theory)}$$

607 Theoretical uncertainties arise from the modelling of the heavy flavour content of the jets in  
 608 diboson plus multijet events. The expected flavour composition for WZ events passing the  
 609 b-loose (resp. b-tight) jet selection is approximately 35% (13%) of events with mistagged jets  
 610 from gluons or u,d,s quarks, 47% (50%) of events with a jet from a charm quark or antiquark, and  
 611 the remaining fraction from events with at least one bottom quark or antiquark. Uncertainties

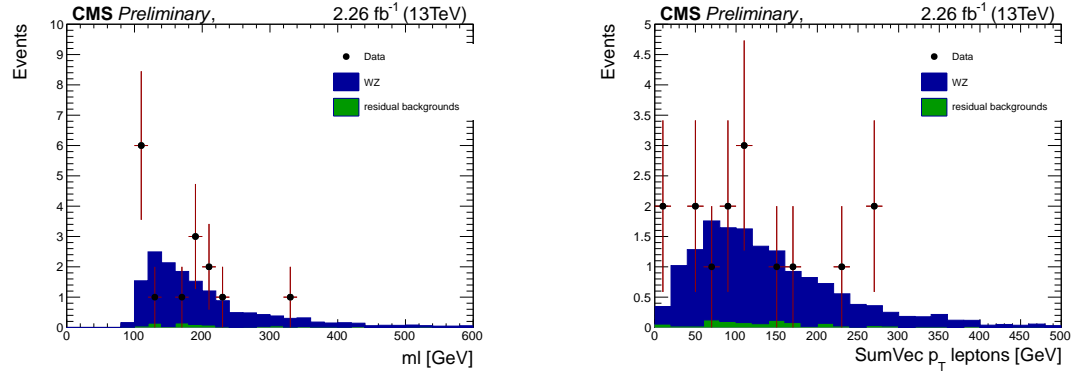


Figure 52: Distribution of the invariant mass of the selected leptons (left) and vectorial sum of the transverse momenta of the leptons (right) after a fit of the WZ and background processes to the data

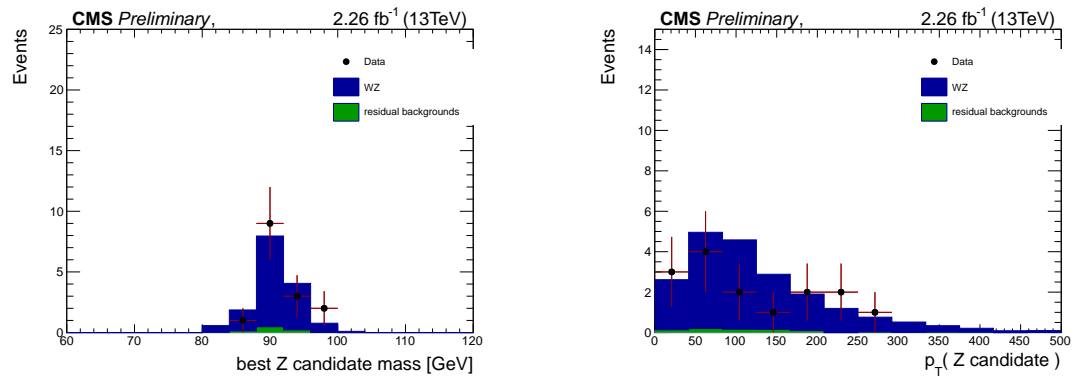


Figure 53: Distribution of the Z candidate invariant mass (left) and transverse momentum (right) after a fit of the WZ and background processes to the data

612 on the extrapolation arising from the parton distribution functions are estimated by simulated  
 613 reweighting of the events to different PDG sets and all their associated eigenvectors or replicas.

614 The overall uncertainty on the normalization of the WZ background is composed by the sta-  
 615 tistical uncertainty in the control region, from the residual backgrounds in the control region,  
 616 from the uncertainties on the b-tagging efficiencies, from the parton distribution functions and  
 617 from the theoretical uncertainties on the extrapolation (dominated by the uncertainty on the  
 618 flavor composition of the final state due to higher-order QCD terms).

### 619 7.3 Charge misassignment background

620 The background from processes with prompt opposite-sign lepton pairs like  $t\bar{t}$  or DY+jets,  
 621 where one of the two leptons has a wrongly assigned charge, is estimated from the measured  
 622 charge misassignment probabilities and the events of a corresponding opposite-sign control re-  
 623 gion. Naturally, this background is only relevant for the same-sign dilepton channels. Studies  
 624 in MC show the charge misassignment probability for muons to be negligible, and we subse-  
 625 quently restrict ourselves to electrons.

#### 626 7.3.1 Measurement of the electron charge misassignment probabilities

627 The charge misassignment probability for electrons can be extracted from the data, in events  
 628 with two same-sign electrons with invariant mass close to the mass of the Z boson. Electron  
 629 pairs in the peak are sure to be from real opposite sign pairs with a wrongly assigned charge  
 630 on one leg. Figure 54 shows the same-sign Z peak for events where exactly two good electrons  
 631 pass the full selection.

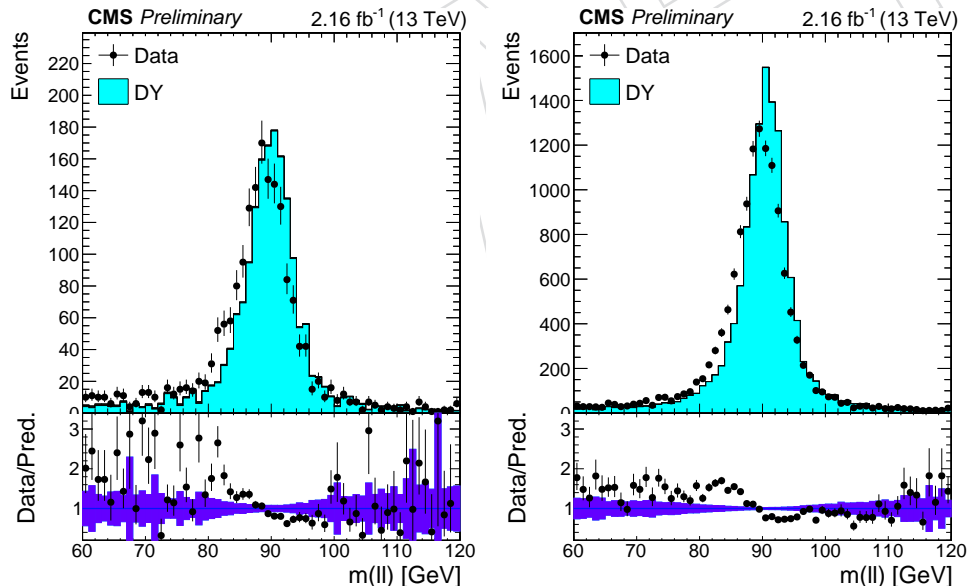


Figure 54: Di-electron invariant mass for same-sign pairs passing the full electron selection, including the triple charge agreement (left), and excluding it (right). Events in the left plot are used to extract the charge misassignment probability.

632 Charge misassignment probabilities are calculated for different bins of electron  $p_T$  and  $\eta$  by  
 633 extracting same-sign and opposite-sign event yields categorized in the kinematics of the two  
 634 lepton legs. In each category, the event yield of electron pairs from Z decays is determined  
 635 from a fit to the invariant mass shape, and depends on the charge misassignment probabilities  
 636 of each leg. The invariant mass shape is modeled with a crystal ball and Breit-Wigner function  
 637 for the signal and an exponentially falling function for the backgrounds.

- 638 Electron kinematics are separated in three  $p_T$  ( $10\text{--}25\text{ GeV}$ ,  $25\text{--}50\text{ GeV}$ , and  $\geq 50\text{ GeV}$ ) and two  
 639  $\eta$  bins ( $0\text{--}1.479$  and  $1.479\text{--}2.5$ ), resulting in a total of 21 distinct categories of electron pairs.  
 640 The six charge misassignment probabilities are then determined in a simultaneous fit to the 21  
 641 same-sign and opposite-sign event yields.  
 642 The resulting misassignment probabilities range between about 0.03% in the barrel and about  
 643 0.4% in the end caps and are shown in Tab. 18 and Fig. 55.

Table 18: Electron charge misassignment probabilities (in percent) as determined in data (top) and Drell–Yan MC (bottom).

| Data                    | $10 \leq p_T < 25\text{ GeV}$ | $25 \leq p_T < 50\text{ GeV}$ | $50\text{ GeV} \leq p_T$ |
|-------------------------|-------------------------------|-------------------------------|--------------------------|
| $0 \leq \eta < 1.479$   | $0.0301 \pm 0.0021$           | $0.0287 \pm 0.0019$           | $0.0293 \pm 0.0054$      |
| $1.479 \leq \eta < 2.5$ | $0.1728 \pm 0.0220$           | $0.1974 \pm 0.0086$           | $0.3457 \pm 0.0256$      |
| <hr/>                   |                               |                               |                          |
| MC                      |                               |                               |                          |
| $0 \leq \eta < 1.479$   | $0.0131 \pm 0.0124$           | $0.0255 \pm 0.0020$           | $0.0340 \pm 0.0050$      |
| $1.479 \leq \eta < 2.5$ | $0.0966 \pm 0.0170$           | $0.2160 \pm 0.0084$           | $0.4170 \pm 0.0208$      |

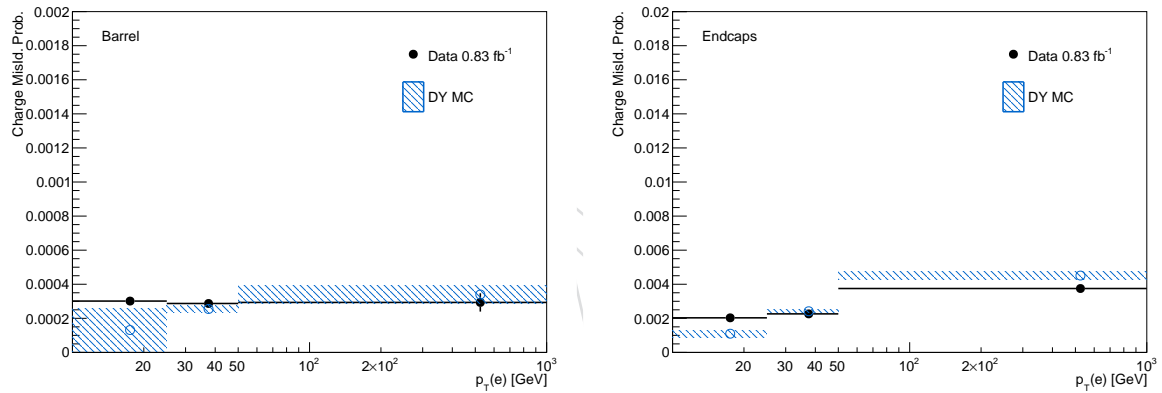


Figure 55: Electron charge misassignment probabilities as a function of  $p_T$  for electrons in the barrel (top) and endcaps (bottom).

### 644 7.3.2 Background estimation

645 Contributions from opposite-sign prompt leptons with charge-misassigned electrons to the  
 646 same-sign dilepton channels with electrons (ee, and e $\mu$ ) are then estimated from the events  
 647 of a control region with identical selection except for the requirement of equal charge of the  
 648 lepton pair. Each event in the control region is assigned a weight of  $P(p_T, \eta)$  for each electron  
 649 with a given  $p_T$  and  $\eta$  in the event (i.e. ee events get a weight of  $P_1 + P_2$  and e $\mu$  events get a  
 650 weight of  $P$ ), where  $P$  is the measured charge misassignment probability.

651 The procedure is tested in two control regions: once using the same events that were used  
 652 to measure the probabilities, dominated by DY events, and once in a selection with at least  
 653 one medium b-tagged jet or two loose b-tagged jet and between 2 and 3 hadronic jets, with a  
 654 significant contribution from t $\bar{t}$  events. Event distributions in the two control regions where the  
 655 background from charge misassigned electrons is estimated as described are shown in Fig. 56  
 656 and 57.

657 From the statistical uncertainty of the measured probabilities and the good agreement of pre-  
 658 dicted charge-flip yields with the observed data distributions in the control regions, we assign  
 659 a generous 30% uncertainty on the predicted event yields from this background.

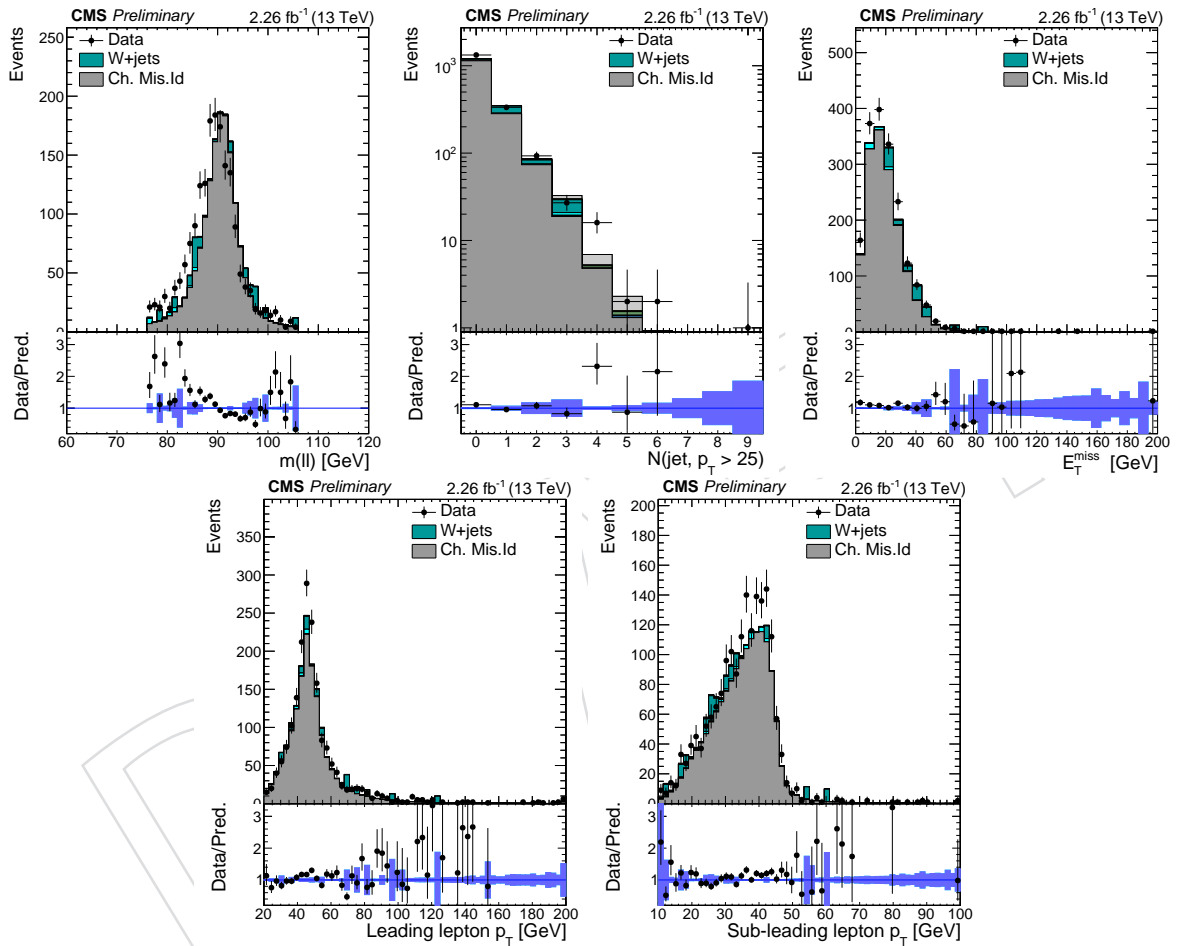


Figure 56: Charge misassignment closure test in DY dominated control region (where the misassignment probabilities are extracted from).

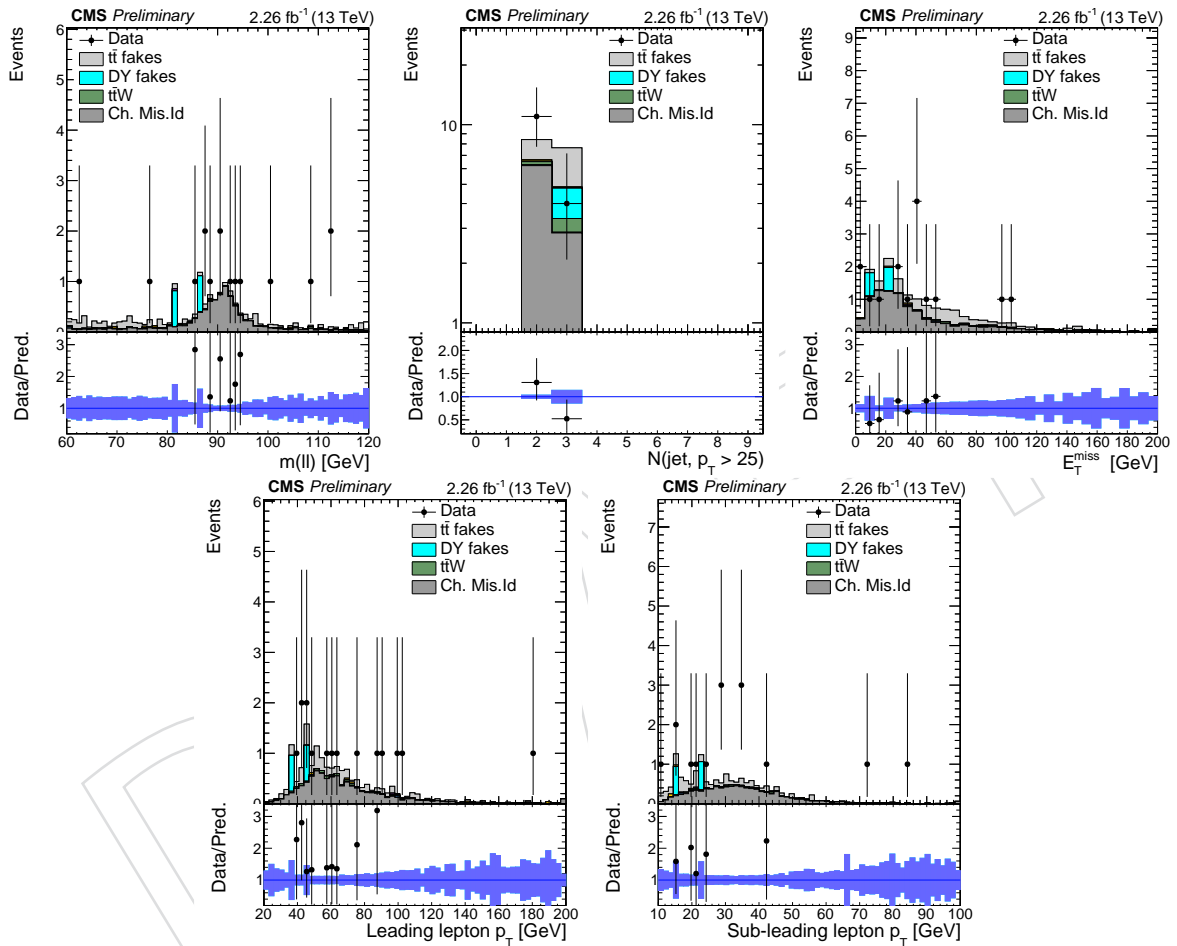


Figure 57: Charge misassignment closure test in a selection of exactly two same-sign electrons passing the full selection, between 2 and 3 hadronic jets, and at least one medium b-tagged jet or two loose b-tagged jets.

## 660 7.4 Fake lepton background

### 661 7.4.1 Fakeable object definition tuning

662 The main control region we use to measure the fake rate is enriched in QCD jet events, and  
 663 is obtained selecting events with one loose lepton and an hadronic jet well separated from the  
 664 lepton ( $\Delta R > 0.7$ ).

665 For muons with  $p_T$  above 20 GeV for muons and electrons with  $p_T$  above 30 GeV, events are  
 666 selected at trigger level requiring a prescaled single lepton trigger (with no isolation require-  
 667 ments), and in the case of electrons, also a particle flow jet with  $p_T$  30 GeV reconstructed at  
 668 HLT. This implies that the fakeable objects in the measurement region all pass the lepton trig-  
 669 ger, while in the application region this is not necessarily the case, as we include also events  
 670 triggered by a single or double lepton trigger. In order to avoid a bias in the background es-  
 671 timate, we therefore need to have a definition of fakeable object so that the fake rate does not  
 672 depend on whether the lepton passes the trigger selection or not.

673 We assess this using non-prompt leptons in simulated lepton-enriched QCD events, where we  
 674 can compare the fake rate with and without requiring the lepton to pass the trigger, for different  
 675 choices of the fakeable object selection. The study reveals two important features: first, the  
 676 trigger turn-on imposes a cut on the reconstructed lepton  $p_T$ , and so it limits the amount of  
 677 sideband available in the extrapolation for given bin in corrected lepton  $p_T$ . Because of this,  
 678 a trigger with a given threshold, can only be used to measure the fake rate for significantly  
 679 larger corrected  $p_T$  value, if we do not want the trigger threshold to bias the result. For example,  
 680 in the muon case the lowest  $p_T$  trigger threshold is 8 GeV, which does not bias the fake rate  
 681 only for corrected  $p_T$  above 20 GeV (Fig. 58, left); the fake rate for softer fakeable objects will be  
 estimated differently as explained in the next section.

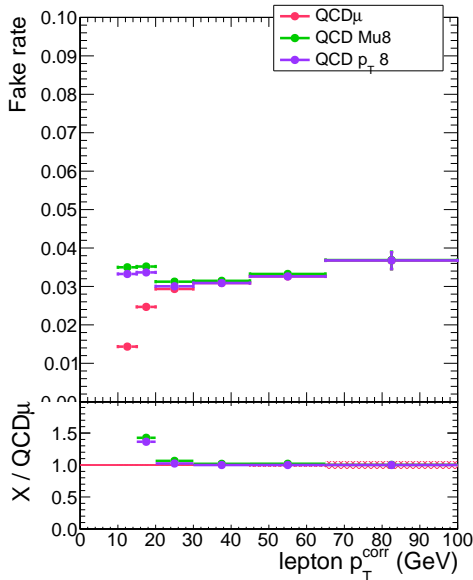


Figure 58: Fake rate for muons in the barrel, from simulated QCD events: with only the loose lepton selection requirement (pink), or after the HLT\_Mu8 trigger (green), or after a requirement of  $p_T > 8$  GeV at reconstruction level (violet, on top of the green). The  $p_T > 8$  GeV requirement and the trigger selection do not bias the fake rate measurement above 20 GeV

682

683 Because of these effectm we measure the fake rate for muons using a combination of the  
 684 HLT\_Mu8 trigger (for corrected  $p_T \in [20, 45]$  GeV) and the HLT\_Mu17 trigger (for corrected  $p_T$

above 45 GeV), and the fake rate for electrons using the HLT\_Ele12\_CaloIdM\_TrackIdM\_PFJet30 trigger (for  $p_T > 30$  GeV). For electrons, triggers with  $p_T$  thresholds of 8 and 23 GeV are also available, but with too large prescale factors to be usable (possibly due to a misconfiguration of the HLT?).

Beyond the impact of the  $p_T$  threshold, the trigger can also bias the fake rate if it has requirements in identification or isolation that are not strictly looser than the selection used at the denominator. For muons, as long as we use triggers with no isolation requirements this is not the case. In the case of electrons, the identification criteria applied at HLT, cut-based, are different from those offline (mva-based), and so we would have a mismatch even for electrons well above the  $p_T$  threshold of the trigger (Fig. 59, left).

We solve this, for electrons with corrected  $p_T > 30$  GeV, by tightening the fakeable object definition including in it also some cut-based electron identification criteria. The selection criteria to emulate the trigger are chosen by comparing electron identification variables for non-prompt electrons in QCD MC events for electrons that pass or fail the trigger. The cuts have to be tight enough that for events passing them the fake rate does not depend strongly on whether the event passes or fails the trigger (Fig. 59, right). However, cuts need to be not too tight less they start causing a loss of signal efficiency, because they use the identification variables in a less optimal way than the mva electron identification. For the criteria we use in this analysis, the loss of efficiency introduced by these cuts for signal MC events that pass the full analysis selection and trigger is about 2% in both the dielectron and electron-muon final states. This is an improvement compared to the version of this AN frozen for the pre-approval, when we used the cut-based electron identification criteria defined for the supersymmetry search in the same-sign dilepton final state, significantly tighter, and which had resulted in a loss of efficiency of 9%(7%) in the ee(e $\mu$ ) final states.

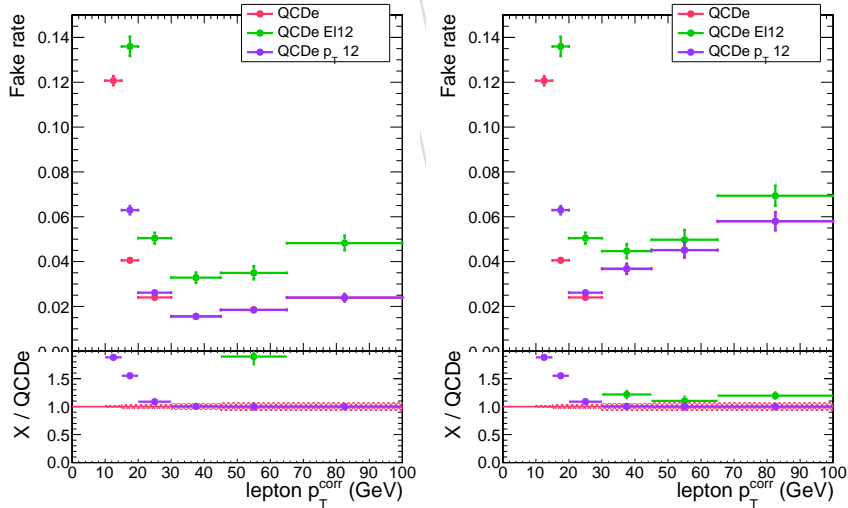


Figure 59: Fake rate for electrons in the barrel, from simulated QCD events: with only the loose lepton selection requirement (pink), after a requirement of  $p_T > 12$  GeV at reconstruction level (violet, on top of the pink above 30 GeV), and after the HLT\_Ele12\_CaloIdM\_TrackIdM\_PFJet30 trigger (green). In the left plot, the loose lepton definition does not include the cut-based electron identification criteria and so the trigger requirement changes the fake rate by a factor 2 or more, while in the right plot the bias is only  $O(15\%)$  in the region of interest ( $p_T > 30$  GeV).

708

The choice of the lepton identification criteria on the fakeable object determine, together with the working point used for the tight lepton definition, the the fake rate for fake leptons, while

they do not affect substantially the fake rate for non-prompt leptons originating from the decay of heavy flavour hadrons. On the other hand, the cut on the b-tagging discriminator of the jet associated to the lepton in the fakeable object definition can alter the fake rate for non-prompt leptons from heavy flavour without affecting fake leptons which are mostly originating from light jets. Thus, we can tune this cut to make the two fake rates more similar, and thus reduce the uncertainties associated to the flavour dependency of the fake rate. The quality of the tuning can be evaluated comparing e.g. the fake rates in  $t\bar{t}$  events in the application region for the b-loose and b-tight category, that have different flavour compositions; the improvement from this tuning is mostly visible for electrons, as in Fig. 60.

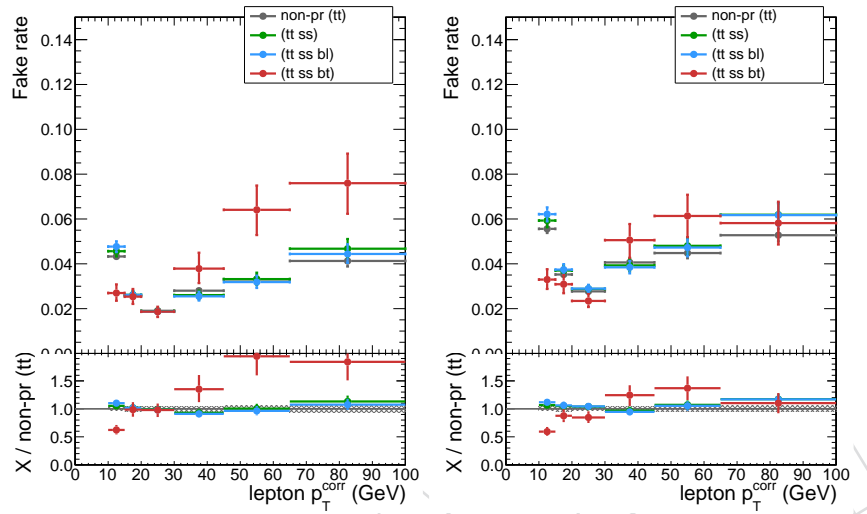


Figure 60: Fake rate for electrons in the barrel, from simulated  $t\bar{t}$  events, inclusively (gray), in same-sign events (green), in same-sign events in the b-loose category (blue), and in same sign-events in the b-tight category (red). Plots in the left column are with the electron trigger emulation cuts and fakeable object definition used in the pre-approval (susy same-sign trigger emulation, CSV cut at 0.89), while plots in the right column are with the new definition (our trigger emulation, CSV cut at 0.605).

719

#### 7.4.2 QCD measurement region definition cuts

For a fixed choice of the fakeable object and numerator, we can then assess how the fake in QCD events agrees with that of  $t\bar{t}$ , and how it depends on the cuts on the tag jet used to select the events. A comparison of fake rates for background leptons in  $t\bar{t}$  and QCD is shown in Fig. 61, both inclusively and selecting only leptons from b-jets. Good agreement between the two MC samples is observed for electrons with  $p_T > 30$  GeV and for muons of any  $p_T$ .

A comparison of fake rates for QCD events as function of the requirements on the recoiling jet in the QCD selection is illustrated in Fig. 62. For both leptons, we observe an excellent stability of the fake rate as function of the recoiling jet  $p_T$ , and only a moderate dependency on the b-tagging requirements of the away jet. So, we decide to define the measurement region requiring only  $p_T > 30$  GeV on the recoiling jet, and no b-tagging, to benefit from the largest event sample and reduce the statistical uncertainties in the measurements. This is an improvement with respect to the version of the AN frozen for pre-approval, where due to a less optimal choice of the fakeable object and trigger emulation the electron fake rate was more strongly dependent on the b-tagging requirement and a good agreement between  $t\bar{t}$  and QCD could be achieved only requiring the recoiling jet to pass the medium WP of the CSV tagger.

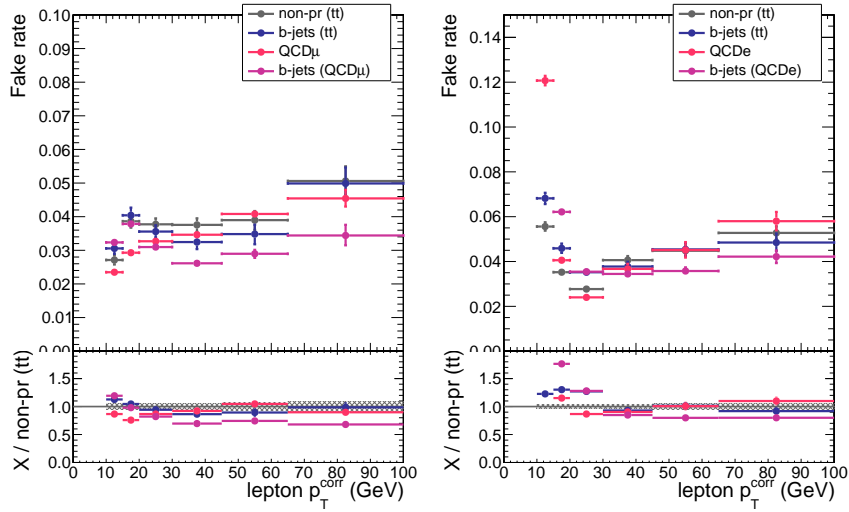


Figure 61: Fake rate for background leptons in the barrel, from simulated  $t\bar{t}$  and QCD events, inclusively or selecting only those from B hadron decays. The left figure is for muons, the right for electrons.

### 7.4.3 QCD measurement: prompt lepton contamination

An important challenge in measuring the fake rate in jet events in data is the contamination of prompt leptons, mostly from W and Z production in association with hadronic jets. In order to suppress the Z contamination, events with more than one loose lepton are vetoed, leaving mostly events with one leptons outside the acceptance or from  $Z \rightarrow \tau_l \tau_h$ . A good discrimination between QCD events and W can be achieved from the transverse mass of the lepton and missing energy in the event,  $M_T(\ell, E_T^{\text{miss}})$ . In the version of the analysis frozen for the pre-approval, a tight cut  $M_T(\ell, E_T^{\text{miss}}) < 15 \text{ GeV}$  was applied, and the residual contamination was subtracted at numerator and denominator in each  $p_T$  bin using simulated W/Z + jets events. The simulation was normalized to the data from a fit to  $M_T(\ell, E_T^{\text{miss}})$ , in the sample of events at the fake rate numerator (i.e. passing the tight requirements), before the cut at 15 GeV.

For this version of the analysis, we implemented two improvements on that procedure. The first improvement is a change in the discriminating variable used: the traditional transverse mass

$$M_T(\ell, E_T^{\text{miss}}) = \sqrt{2p_{T\ell}E_T^{\text{miss}}(1 - \cos \Delta\phi)}$$

is obviously correlated with the lepton  $p_T$ , and so also with the lepton fake rate. To avoid this correlation, which can potentially introduce biases in the subtraction procedure, we define a new variable

$$M_T^{\text{fix}}(\ell, E_T^{\text{miss}}) := \sqrt{2p_{T\text{fix}}E_T^{\text{miss}}(1 - \cos \Delta\phi)}$$

replacing the lepton  $p_T$  with a fixed number (35 GeV), and thus relying only on the lepton direction. This variable still has a good discriminating power against W + jets but is much less correlated with the lepton  $p_T$  and so with the fake rate.

The second improvement compared to the pre-approval is the introduction of two alternative ways to implement the subtraction of the prompt contamination. The first alternative procedure is the one used in the run 1 analysis, and documented in detail in Sec.7.4.2 of AN-13-159, except that we update it to use  $M_T^{\text{fix}}(\ell, E_T^{\text{miss}})$  instead of  $E_T^{\text{miss}}$ . The procedure relies on two measurements of the fake rate in data, one for small  $M_T^{\text{fix}}$  values and one for large and large  $M_T^{\text{fix}}$  values. Assuming the fake rate to be independent from  $M_T^{\text{fix}}$ , and taking from the simulation

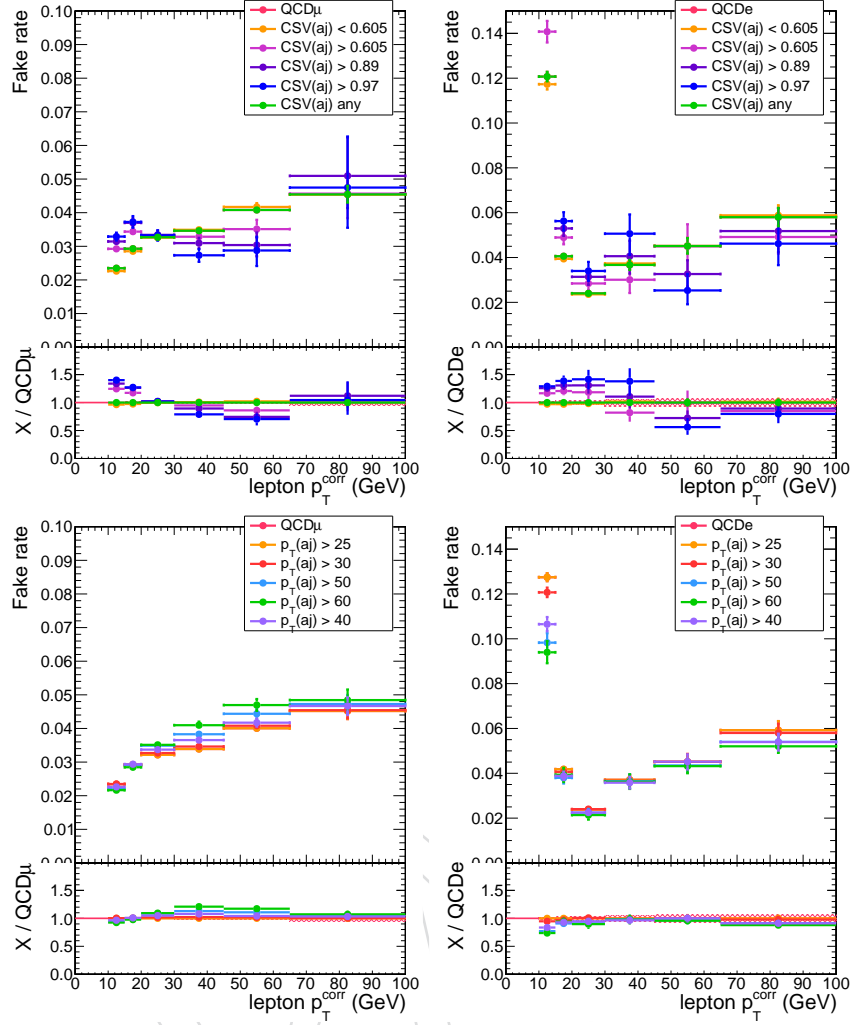


Figure 62: Fake rate for leptons in the barrel in simulated QCD and  $t\bar{t}$  events, as varying the requirement on the recoiling jet. In the top row, different cuts are applied on the b-tagging discriminator of the jet, while in the bottom row different  $p_T$  thresholds are applied. Fake rates in the left column are for muons, those in the right column for electrons.

the ratio of V + jets events expected in the two regions, it is possible to unfold the fake rate for QCD events from the two measurements:

$$f_{\text{QCD}} = \frac{f_S - r_{V+j}^{\text{SL}} f_L}{1 - r_{V+j}^{\text{SL}}} \quad \text{where} \quad r_{V+j}^{\text{SL}} = \left( \frac{N_{V+j}^S}{N_{V+j}^S} \right) / \left( \frac{N_{\text{data}}^S}{N_{\text{data}}^L} \right),$$

where  $f_i$  are the fake rates measured in data for small (S) and large (L) values of  $M_T^{\text{fix}}$ ,  $N_{V+j}^i$  are the expected event yields from V + jets and  $N_{\text{data}}^i$  are the observed events in data in the two regions at the denominator of the fake rate. This procedure can be performed separately in each bin of  $p_T$ ,  $|\eta|$ . In addition to the statistical uncertainties on the fake rate measurement in the two regions and on  $r_{V+j}^{\text{SL}}$ , we also add a systematical uncertainty on  $r_{V+j}^{\text{SL}}$  from the difference in evaluating  $N_{V+j}^S / N_{V+j}^S$  at the denominator and numerator of the fake rate.

A second alternative procedure relies on a simultaneous fit of the  $M_T^{\text{fix}}$  distribution for passing and failing probes, in a very similar way to the method used in the tag and probe method at the Z peak by fitting the invariant mass of the dilepton pair to extract efficiencies for the signal

even in the presence of background . In our case, fit is done using templates from simulation for the QCD and V + jets contributions. In addition to bin-by-bin statistical uncertainties on the templates, we include systematic shape uncertainties on the templates: we allow both a linear deformation of the template and a stretching of the template, as illustrated in Fig. 63. The shape systematics are assumed to be uncorrelated between QCD and V + jets, but totally correlated between passing and failing probes; the size of the deformation has been chosen to approximately cover the data to simulation differences observed across the various bins. The final uncertainty on the fake rate is obtained by profiling the likelihood of the simultaneous fit, and thus includes both the statistical and the systematical uncertainties.

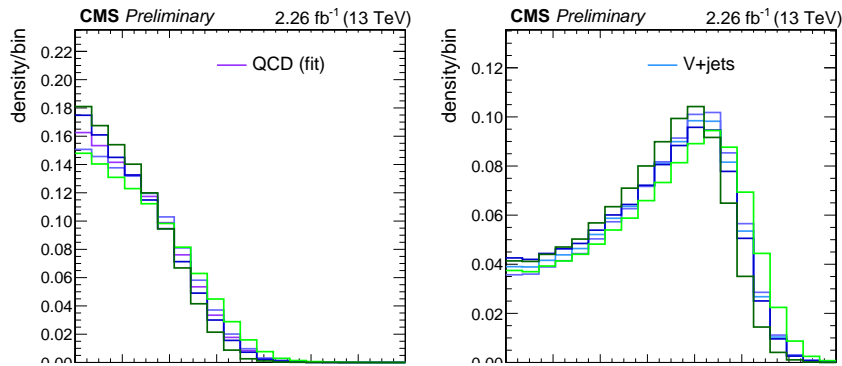


Figure 63: Shape uncertainties on the  $M_T^{\text{fix}}$  templates for muons in the barrel, in the bin of corrected  $p_T$  20–30 GeV, for QCD events (left) and V + jets events (right)

767

Results of the measurement with all three subtraction methods are shown in Fig. 64. For the cut and subtraction method, the error bars include a systematical uncertainty of 10% on the subtraction, which dominates over the statistical uncertainties at larger  $p_T$ . Within uncertainties, the three methods agree among themselves and also with the fake rate in MC. Since we do expect at least some correlation in the uncertainties of the three measurements, we opt for a conservative combination of the three by taking as central value the weighted average and as uncertainty band the envelope of the three uncertainty bands.

#### 775 7.4.4 Low $p_T$ electrons

The fake rate for electrons with  $p_T < 30$  GeV is derived using  $Z + \ell$  events, where the leptons from the  $Z$  boson can be used to trigger the event without biasing the third lepton. This is justified by simulations, where the fake rate for non-prompt electrons  $Z + \ell$  is found to be in good agreement with the one for non-prompt electrons in  $t\bar{t}$  events (Fig. 65, left)

Similarly to the measurement from QCD dijet events, a challenge is posed by the contamination from prompt leptons, in this case from  $WZ$  and  $ZZ$  production. As this control region differs from the QCD one only by the replacement of the tag jet with a  $Z$  boson, it is similarly possible to discriminate between the non-prompt and prompt leptons contributions on the basis of  $M_T^{\text{fix}}$ , and use the same subtraction methods (Fig. 65, right)

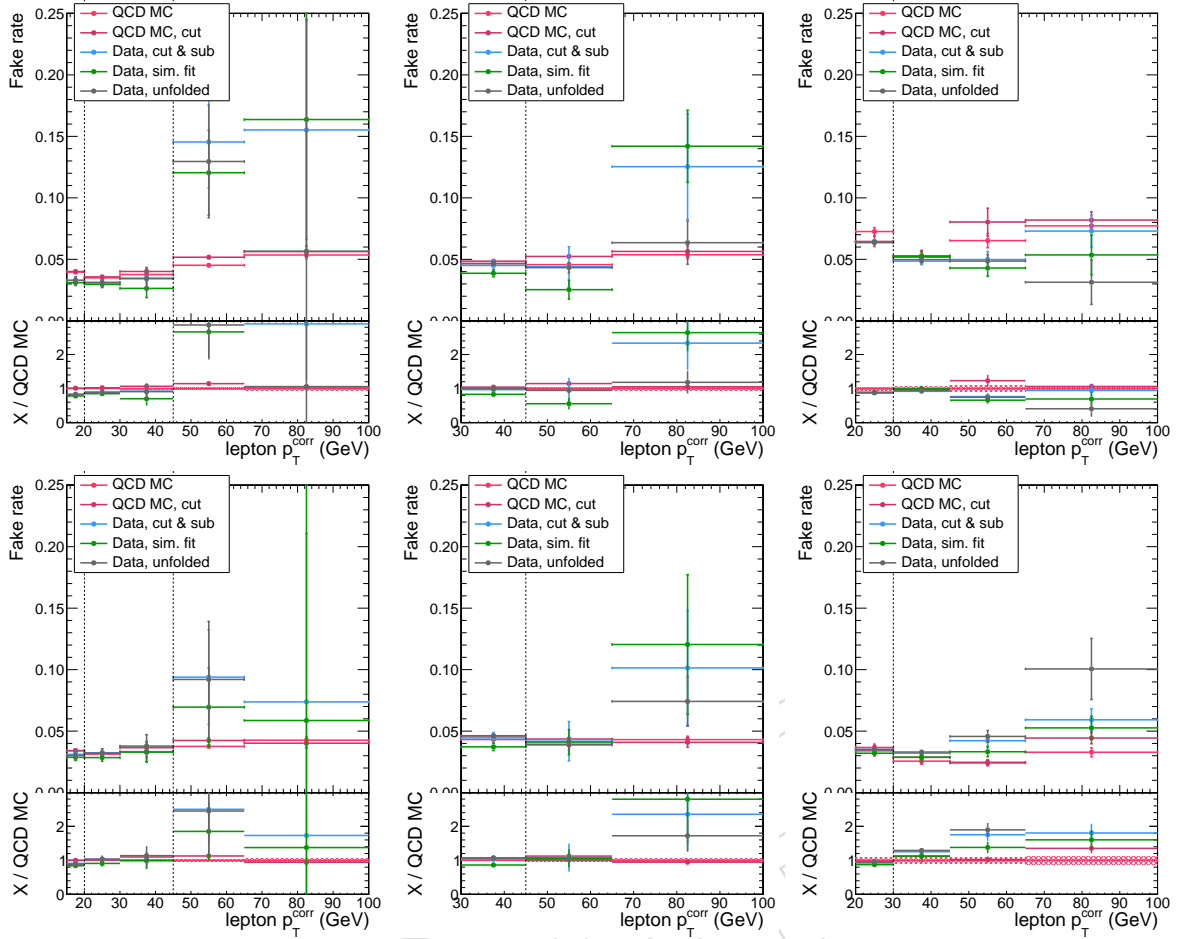


Figure 64: Fake rate measurement in data, for different subtraction methods, and compared with the predictions from simulation for non-prompt leptons from QCD MC. The left column is for muons passing the HLT\_Mu8 trigger, the middle one for muons passing the HLT\_Mu17 trigger, and the right column is for electrons passing the HLT\_Ele12\_CaloIdM\_TrackIdM\_PFJet30 trigger. Plots in the top row are for the barrel, those in the bottom row for the endcaps. For illustration, the plots for each trigger include also  $p_T$  bins whose measurement is not used in the analysis. For this plot alone, the cut-based electron id requirements are included in the loose lepton definition also below 30 GeV, so that the fake rate is continuous.

#### 785 7.4.5 Low $p_T$ muons

786 For the tight lepton MVA working point now used, it is not possible to derive fake rates for  
 787 muons from  $Z + \ell$  events since the expected yield of background leptons at the numerator is  
 788 too small (this was already quite challenging for the looser working point that was used in  
 789 the version of the analysis frozen for pre-approval). We thus decide to rely on QCD events,  
 790 since muon triggers with thresholds of 5 GeV or lower are not available in the 2015 dataset we  
 791 have to rely on prescaled jet triggers. We decide to rely on the logical OR of the HLT\_PFJet60  
 792 and HLT\_PFJet80 triggers, since the HLT\_PFJet40 has a too large prescale to be usable. Having  
 793 verified on QCD MC that the higher threshold on the jet does not bias the fake rate significantly,  
 794 we thus perform the measurement in an identical way as what done for higher  $p_T$  muons.  
 795 Within the large uncertainties driven by the small event yield at the numerator, we observe  
 796 a reasonable agreement between different prompt contamination subtractions and between  
 797 data and simulations (Fig. 66).

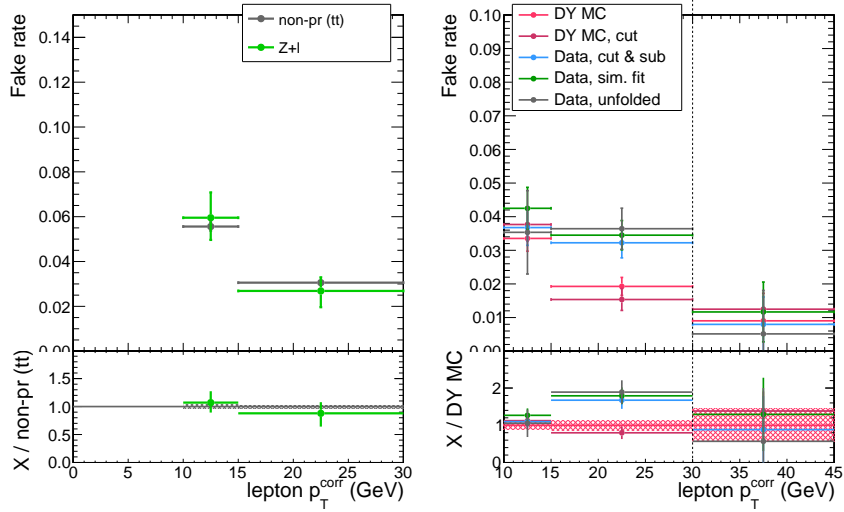


Figure 65: Left: comparison of fake rates for electrons in the barrel between simulated  $Z + \ell$  and  $t\bar{t}$  events. Right: measurements of the fake rate in data for electrons in the barrel, with different subtractions for the prompt contamination.

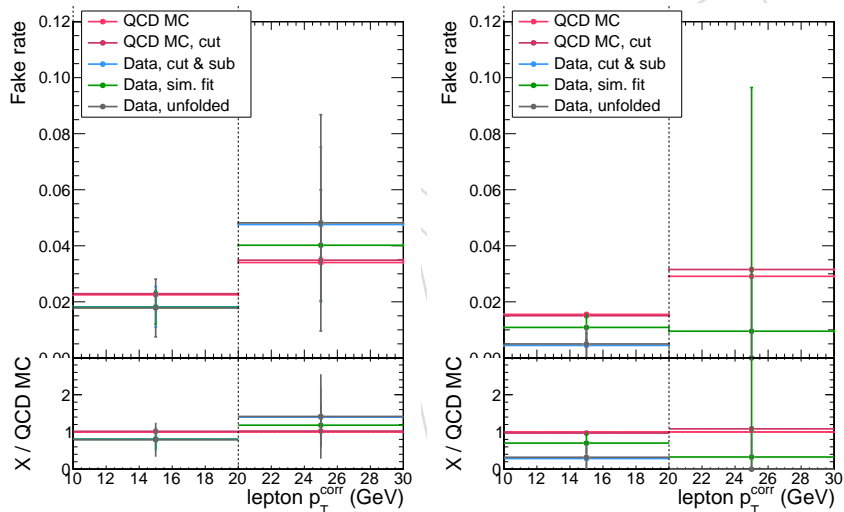


Figure 66: Measurements of the fake rate in data for low  $p_T$  muons using QCD events collected from prescaled jet triggers, in the barrel (left) and in the endcaps (right)

#### 7.4.6 Results

The final fake rates for electrons and muons are shown in Fig. 67. Overall, a good agreement between data and predictions from simulations is observed. Uncertainties are larger for very low  $p_T$ , driven by statistical uncertainties, and at very high  $p_T$ , driven by the uncertainties on the subtraction of the prompt lepton contamination.

#### 7.4.7 Fake rate application

The application of the fake rates follows the same principles already used for the analysis that was performed on the 8 TeV dataset.

In summary, a control region enriched in events with fake leptons, denoted as *application region* in the following, is selected by requiring that at least one of the selected leptons fails the tight lepton requirements.

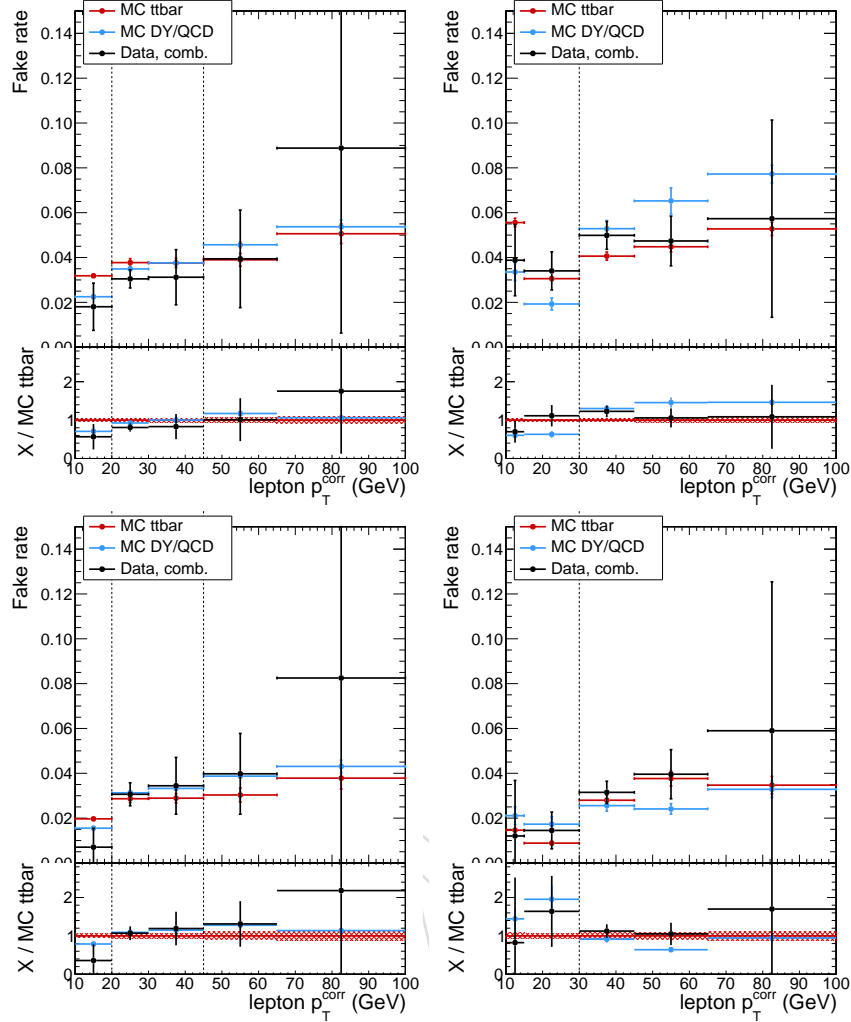


Figure 67: Summary of the fake rate measurement in events in data, compared with the predictions from simulated events in the measurement region (blue) and from non-prompt leptons in  $t\bar{t}$  (red). Plots in the left column are for muons, those in the right column for electrons; the top row is for the barrel, the bottom for the endcaps. Measurements and expectations are derived from QCD events using different triggers, except for the electrons below 30 GeV for electrons which are derived from  $Z + \ell$  events. The data values and uncertainties are the weighted average and envelope of the different prompt contamination subtraction algorithms.

809 The extrapolation from this control region to the signal region is performed by expressing the  
 810 yields of events where  $k$  leptons pass the full selection and  $n - k$  fail it in terms of the yields  
 811 of events with  $n$  leptons among prompt and non-prompt ones, efficiencies and fake rates, for  
 812  $n = 2$  or  $3$  and all possible values of  $k$ .

813

814 In two lepton events ( $n = 2$ ), the background contribution in the signal region can be expressed  
 815 as:

$$N_{pp}^{\text{bkg}} = \frac{f_1}{1-f_1} N_{pf} + \frac{f_2}{1-f_2} N_{pf} - \frac{f_1 f_2}{(1-f_1)(1-f_2)} N_{ff}$$

816 under the approximation that the contribution of prompt leptons failing the selection can be

neglected with respect to the contributions of non-prompt leptons. It is worth noting that the event yield observed in the signal region does not affect the background prediction.

819

Following the same logic, the background prediction in the three lepton category is obtained by weighting the events in the application region according to the following prescription:

- events with only one failing lepton are weighted by  $f/(1-f)$ , where  $f$  is the fake rate evaluated on the kinematic quantities of the failing lepton;
- events with two failing leptons ( $i, j$ ) are weighted by  $-f_i f_j / ((1-f_i)(1-f_j))$ ;
- events with all three failing leptons are weighted by  $f_1 f_2 f_3 / ((1-f_1)(1-f_2)(1-f_3))$ .

A proof of the results presented above can be found in [31].

#### 7.4.8 Closure tests on simulated events

Closure tests are performed on simulated events in order to confirm that the methods described in the present Section are well suited to predict the reducible background after the event selection requirements.

A fake rate extracted from non-prompt leptons in QCD MC, selected inclusively, is first applied to 2lss semi-leptonic  $t\bar{t}$  simulated events where at least one of the two selected candidates fails the tight lepton requirements. Moreover, an alternative fake rate from non-prompt leptons in  $t\bar{t}$  MC, selected inclusively as well, is applied to the same 2lss sample.

The test described above is performed in different event selections (separately for lepton flavors and analysis category). The difference in normalization between the two predictions, as well as their difference in the shape of the two kinematic discriminators against the  $t\bar{t}$  and  $t\bar{t}V$  backgrounds, are propagated as a systematic uncertainty to the fit used to extract the signal.

An example of the distributions can be found in Fig. 68.

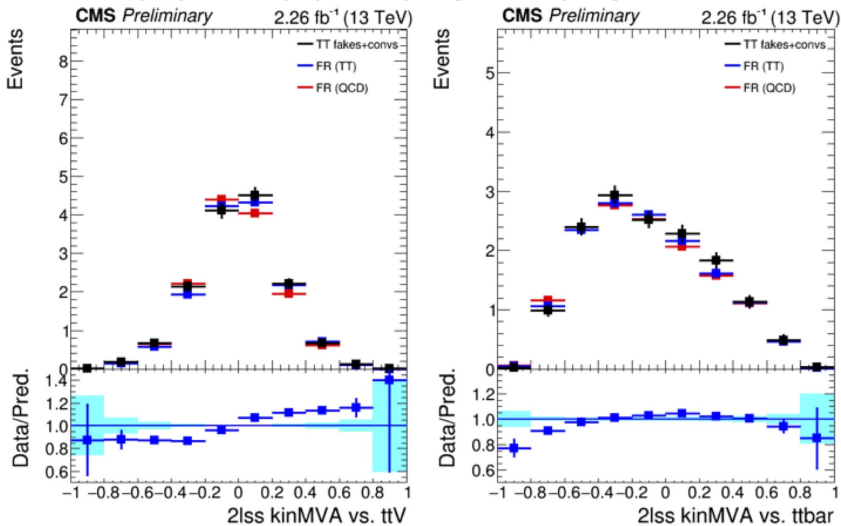


Figure 68: Shape of kinematic discriminators for semi-leptonic  $t\bar{t}$  events, and for background predictions obtained in simulation using fake rates extracted in QCD and  $t\bar{t}$  events.

Moreover, the uncertainty in the fake rate measurement is propagated to the final fit studying both the difference in background normalization from a coherent shift in the fake rate map (Fig. 69), and the effect on the shape of the kinematic discriminators arising from possible

843 trends in the fake rate map as a function of the lepton  $p_T$  and  $|\eta|$  within the fake rate map  
 844 uncertainty (Fig. 70).

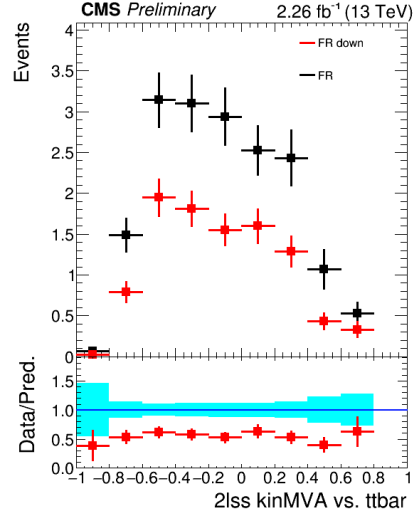


Figure 69: Example of the difference in background normalization arising from a coherent downwards shift of the fake rate map.

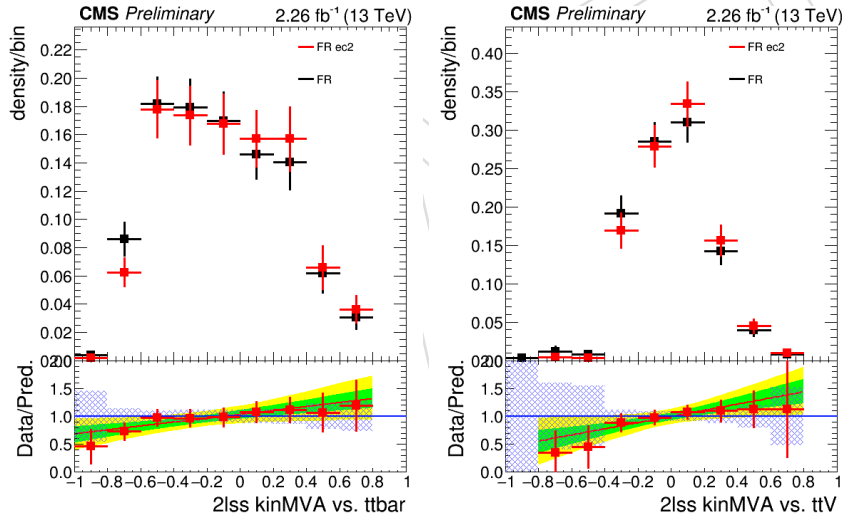


Figure 70: Example of the difference induced on the shape of kinematic discriminators for semi-leptonic  $t\bar{t}$  events, arising from trends in the fake rate map as a function of the lepton  $p_T$  and  $|\eta|$ .

## 8 Results

The results are interpreted by comparing the observed yields with the expectation from background and a 125 GeV SM Higgs boson. We introduce a signal strength parameter  $\mu = \sigma/\sigma_{\text{SM}}$ , and we scale by that value the expected yields from  $t\bar{t}H$  without altering the branching fractions or the kinematics of the events.

Results in terms of the asymptotic 95% CL upper limit on  $\mu$  are presented in Table 19. The median observed (expected) upper limit from the combination of all decay modes is 3.5 (2.6).

The best fit signal strength is presented in Table 20.

| Category            | Observed limit | Expected limit $\pm 1\sigma$ |
|---------------------|----------------|------------------------------|
| same-sign di-lepton | 2.3            | 2.8 (+1.4) (-0.9)            |
| tri-lepton          | 12.1           | 5.5 (+3.0) (-1.8)            |
| combined            | 3.5            | 2.6 (+1.3) (-0.8)            |

Table 19: Expected asymptotic 95% CL upper limits on  $\mu$  under the background-only hypothesis.

| Category            | $\mu$ best fit $\pm 1\sigma$ |
|---------------------|------------------------------|
| same-sign di-lepton | -0.41 (+1.05) (-0.75)        |
| three lepton        | 6.05 (+3.36) (-2.75)         |
| combined            | 0.83 (-1.15) (+1.41)         |

Table 20: Expected best fit of the signal strength parameter under the SM Higgs production hypothesis.

Figures 71 and 72 show the post-fit values of the nuisances and their correlation with the fitted signal strength.

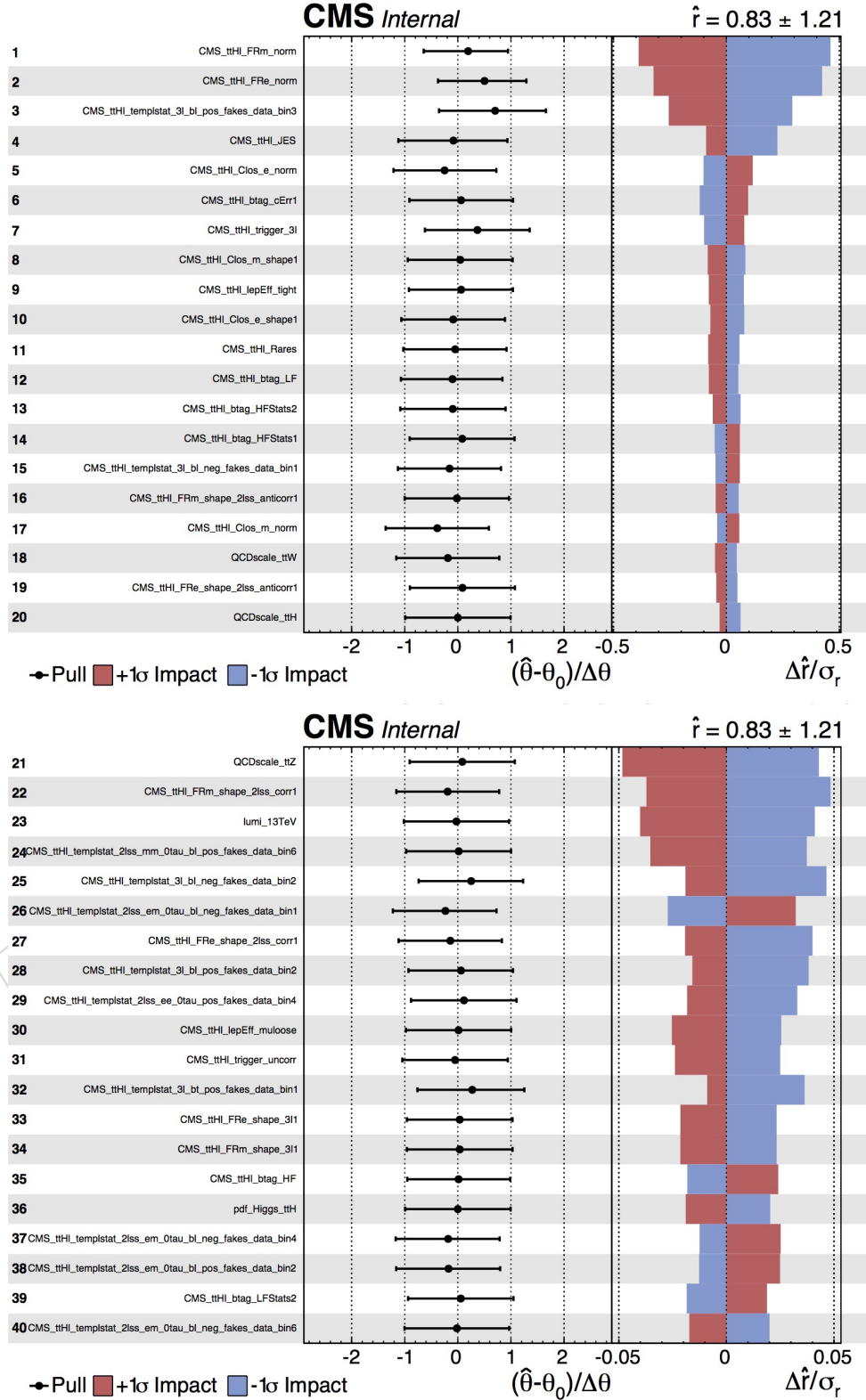


Figure 71: Impact plot showing the correlation between the nuisances and the best fit signal strength.

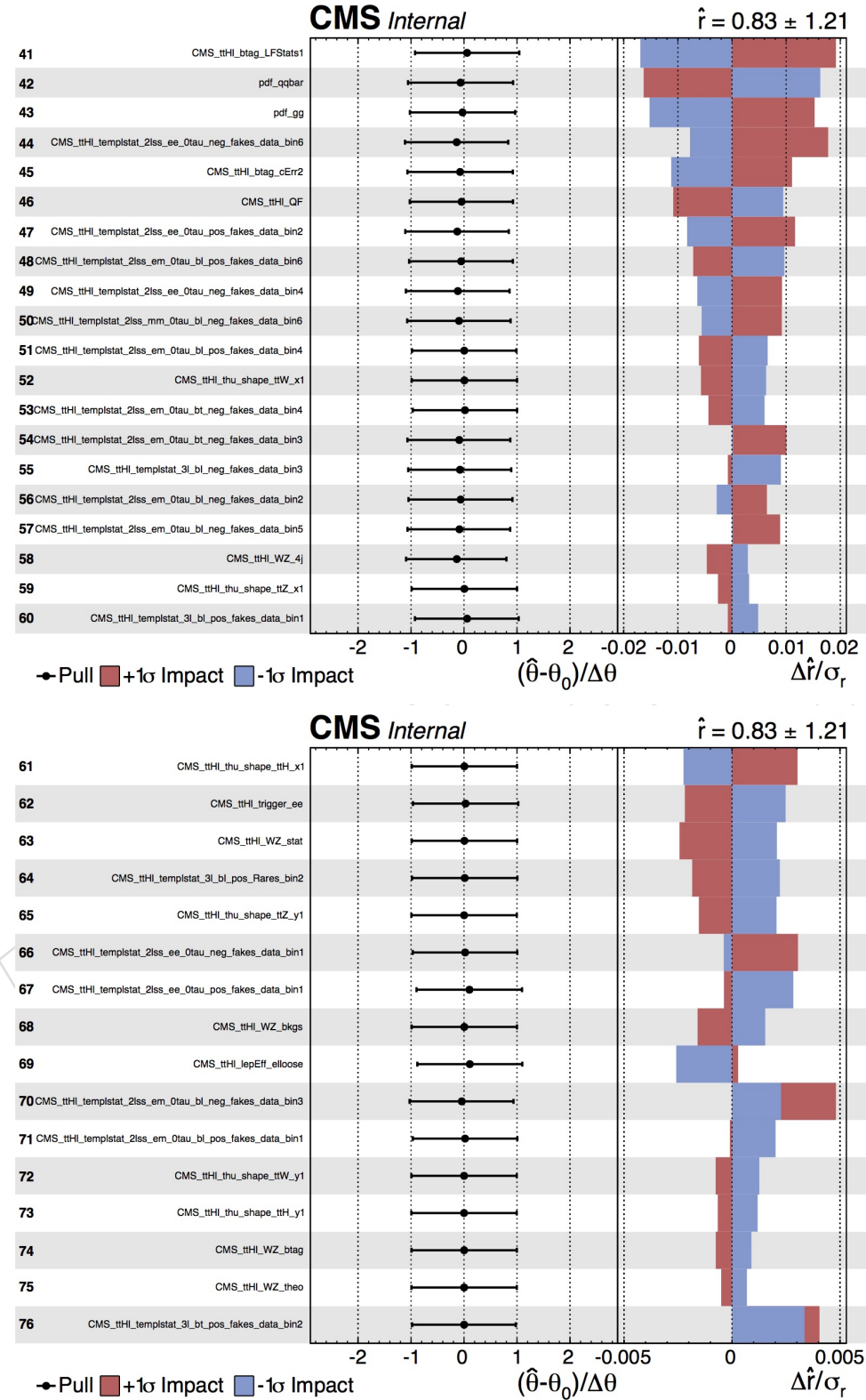


Figure 72: Impact plot showing the correlation between the nuisances and the best fit signal strength.

## 855 A Control region plots

### 856 A.1 Lepton MVA sideband region

857 The 2lss selection is modified by requiring that only one of the two selected leptons fails the  
 858 tight lepton requirements, but still passes those for the fakeable object. In this way, we select a  
 859 region enriched in  $t\bar{t}$  events, where the lepton that fails the tight requirement is a fake lepton.

860 No scale factors for efficiency or b-tag requirements are applied in the following plots (Fig-  
 861 ures 73 and 74). It is worth noting that the contamination from QCD events, estimated to be  
 862 not larger than a few percent of the total yield, is not taken into account by the simulation. We  
 863 observe a good agreement between simulation and data, both in overall normalization and in  
 864 terms of the shape of observables used for the selection and as inputs to the BDT discriminators.  
 865 The latter variables are shown in Fig. 75.

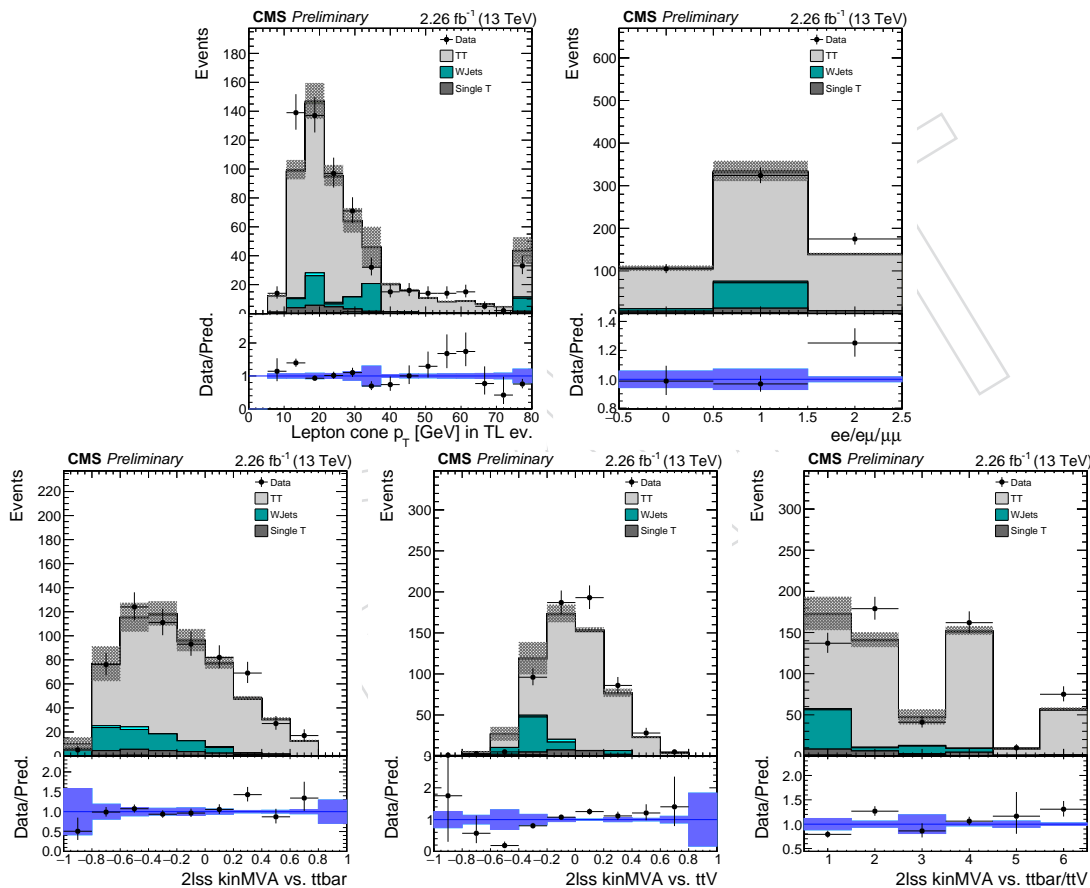


Figure 73: Data and simulation distributions in the 2lss control region with exactly one fakeable lepton failing the tight selection requirements. From top left to bottom right: the cone-corrected  $p_T$  of the failing lepton, the flavor of the lepton pair, the signal BDT discriminators against  $t\bar{t}$  and  $t\bar{t}V$  including the 2D-binned version as described in Section 5. Uncertainties are statistical only.

866 When further relaxing the selection to allow one or both leptons to fail the tight lepton re-  
 867 quirements, the relative QCD contribution increases, as can be inferred by the plots shown in  
 868 Fig. 76.

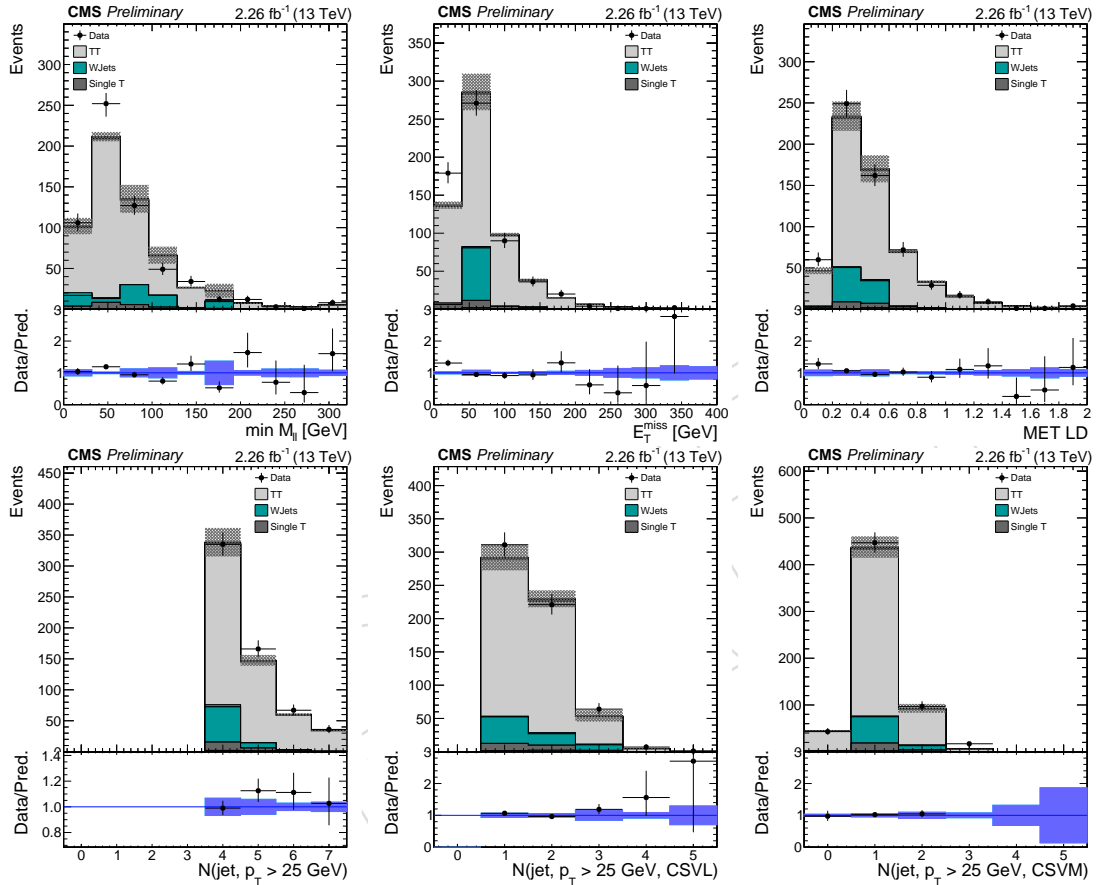


Figure 74: Data and simulation distributions in the 2lss control region with exactly one fakeable lepton failing the tight selection requirements. From top left to bottom right: the minimum invariant mass of loose di-lepton pairs,  $E_T^{\text{miss}}$ ,  $E_T^{\text{miss}}LD$ , multiplicity of inclusive and b-tagged jets. cone-corrected  $p_T$  of the failing lepton, the flavor of the lepton pair, the signal BDT discriminators against tt and ttV. Uncertainties are statistical only.

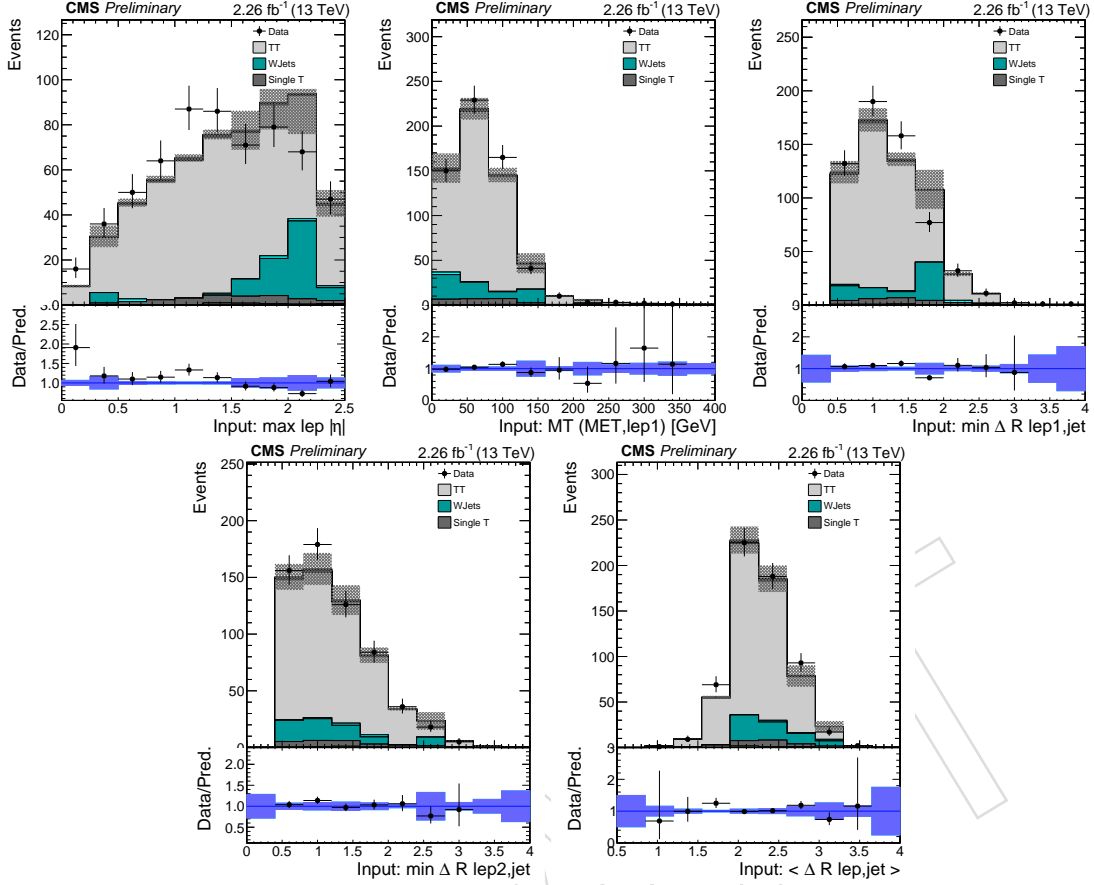


Figure 75: Distributions of several BDT input variables in the 2lss control region with exactly one fakeable lepton failing the tight selection requirements. Uncertainties are statistical only.

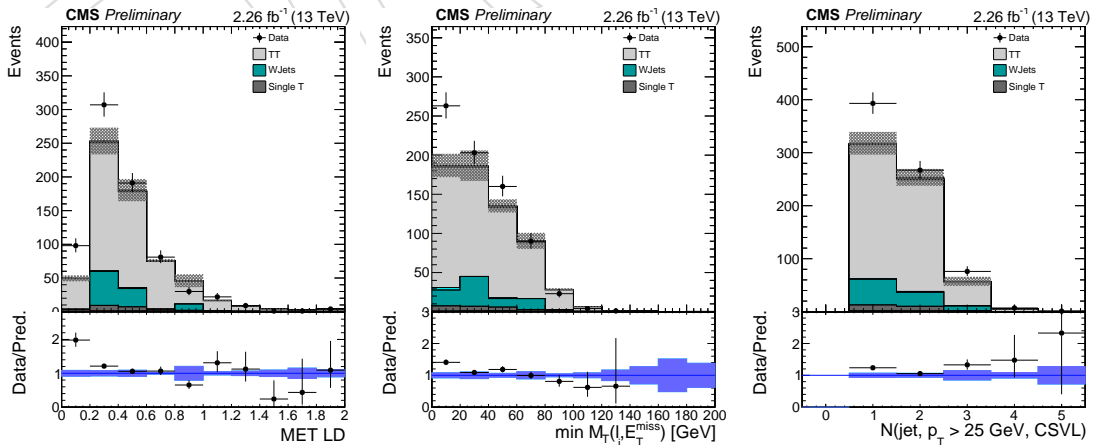


Figure 76: Distributions and simulation distributions in the 2lss control region where at least one fakeable lepton fails the tight selection requirements. Uncertainties are statistical only. The data show an excess over the  $t\bar{t}$  prediction, due to the presence of QCD multi-jet events that are not included among the simulated physics processes here.

## 869 A.2 Jet multiplicity sideband region

870 This 2lss control region is enriched in fakes from  $t\bar{t}$ . It is obtained by requiring exactly three  
 871 reconstructed jets in the final state, in the place of the requirement of at least four that is applied  
 872 in the standard 2lss selection.

873 No efficiency scale factors are applied. Fakes from W+jets are estimated by the fake rate method  
 874 described in Section 7.4, applied on MC events, while all other processes are predicted by the  
 875 simulation. Distributions of event observables are shown in Fig. 77-79.

876 Estimating instead the background from fake leptons and charge mis-assignment from data, as  
 877 described in Section 7.4, we obtain the distributions shown in Fig. 80-82. In all cases we observe  
 878 a satisfactory data/MC agreement, within the statistics currently available.

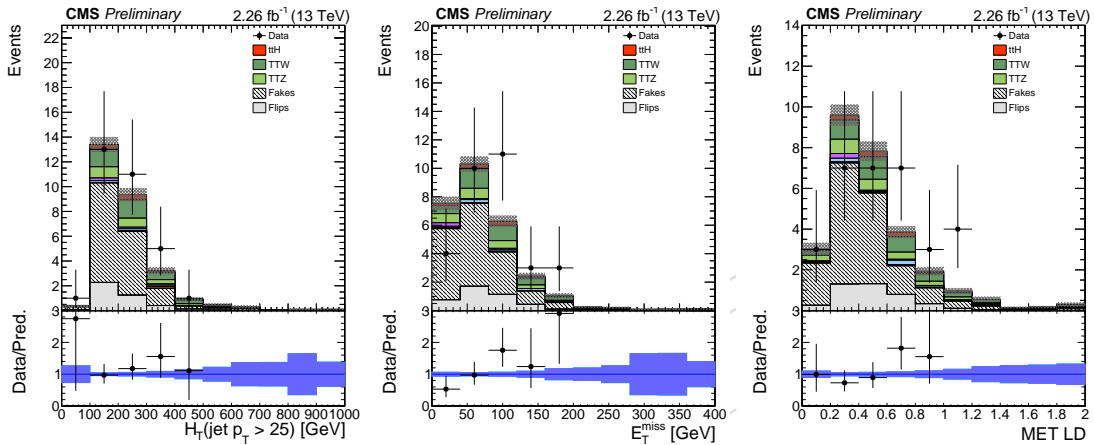


Figure 77: Data and simulation distributions in the 2lss control region with exactly three jets in the final state. From left to right: the  $H_T$ , the  $E_T^{\text{miss}}$ , the  $E_T^{\text{miss}} \text{LD}$ . Uncertainties are statistical only.

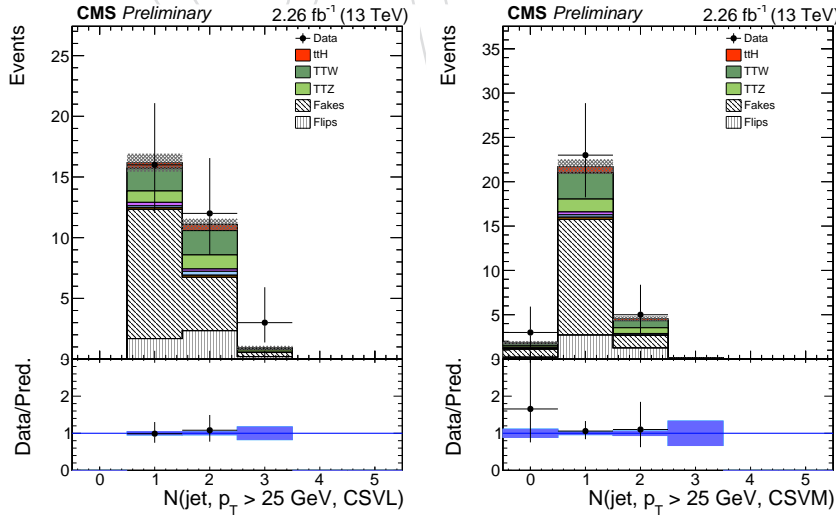


Figure 78: Data and simulation distributions for the number of jets passing the loose and medium working points of the CSV b-tagger, in the 2lss control region with exactly three jets in the final state. Uncertainties are statistical only.

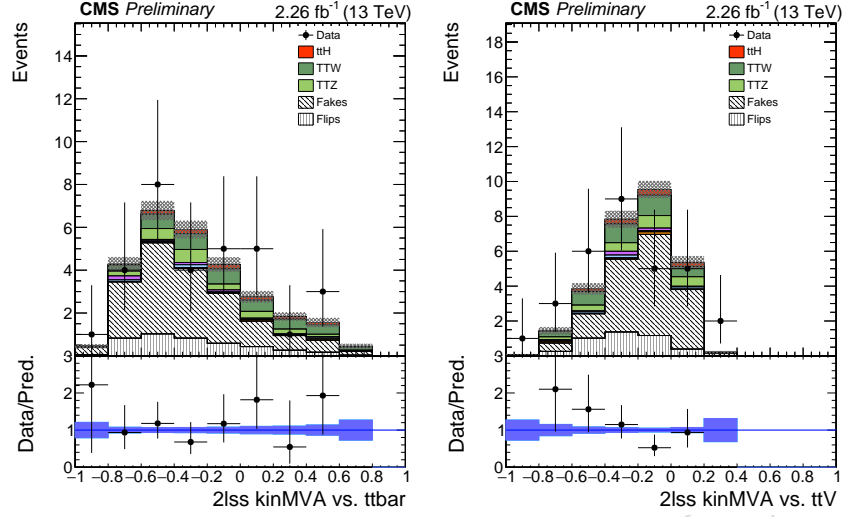


Figure 79: Data and simulation distributions of the discriminators against  $t\bar{t}$  and  $t\bar{t}V$  in the 2lss control region with exactly three jets in the final state. Uncertainties are statistical only.

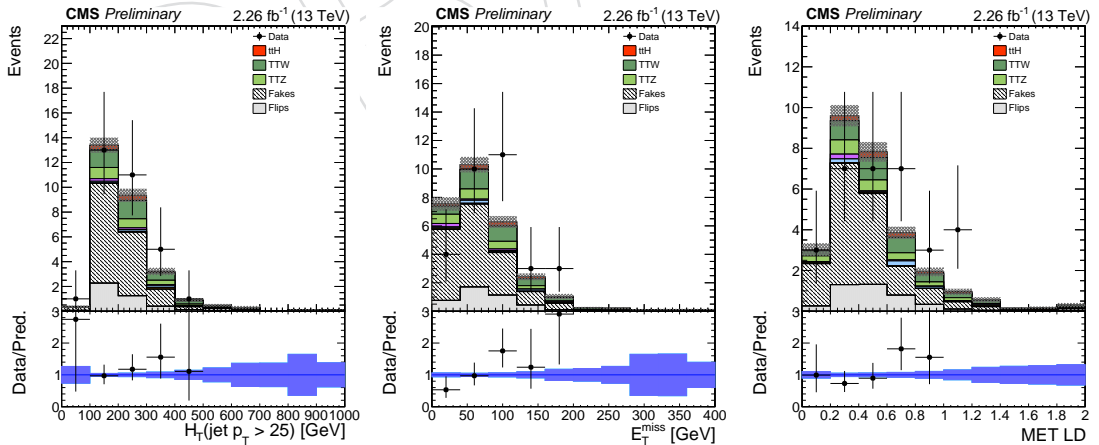


Figure 80: Data and simulation distributions in the 2lss control region with exactly three jets in the final state, with data-driven techniques applied to estimate the background from fake leptons and charge mis-assignment. From left to right: the  $H_T$ , the  $E_T^{\text{miss}}$ , the  $E_T^{\text{miss}} \text{LD}$ .

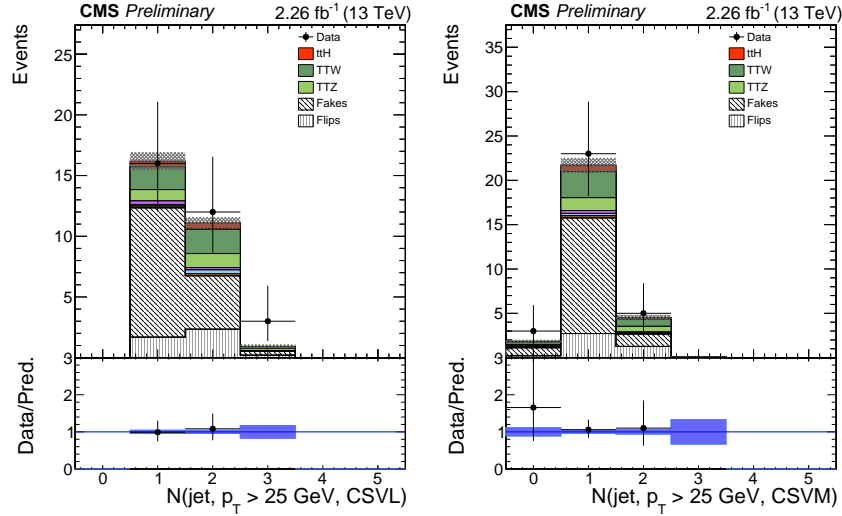


Figure 81: Data and simulation distributions for the number of jets passing the loose and medium working points of the CSV b-tagger in the 2lss control region with exactly three jets in the final state, with data-driven techniques applied to estimate the background from fake leptons and charge mis-assignment.

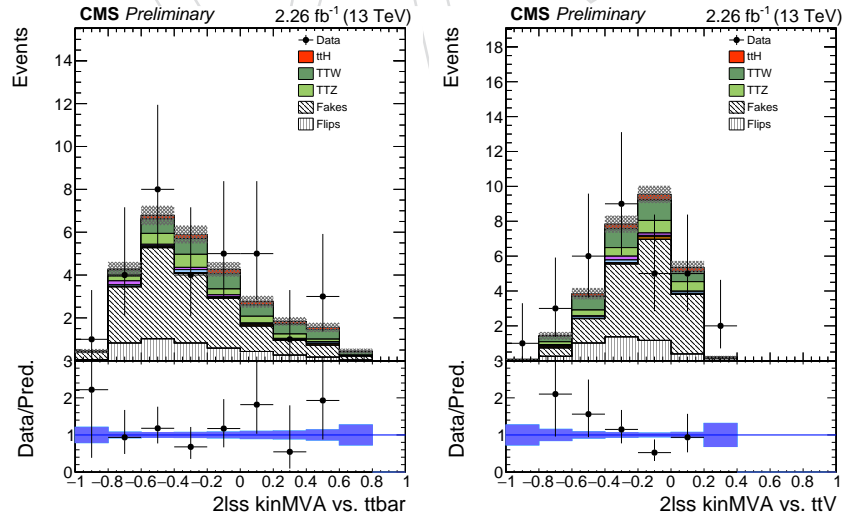


Figure 82: Data and simulation distributions of the discriminators against  $t\bar{t}$  and  $t\bar{t}V$  in the 2lss control region with exactly three jets in the final state, with data-driven techniques applied to estimate the background from fake leptons and charge mis-assignment.

879 **A.3  $t\bar{t} \rightarrow e^\pm \mu^\mp b\bar{b} \nu\bar{\nu}$**

880 This control region is enriched in  $t\bar{t}$  events, and aims at validating the jet-related observables  
 881 used in the analysis. The selection we apply is the same as in the 2lss category of the analysis,  
 882 with the following modifications:

883

- 884 • the two selected leptons are required to be of opposite sign and flavor (one electron  
 885 and one muon);  
 886 • the requirement on the number of jets is relaxed to  $\geq 2$ ;  
 887 • the requirements on the number of b-jets is relaxed to at least one jet passing the  
 888 medium working point of the CSV tagger;

889 No efficiency scale factors are applied. Distributions of some event observables are shown in  
 890 Fig. 83.<sup>2</sup>

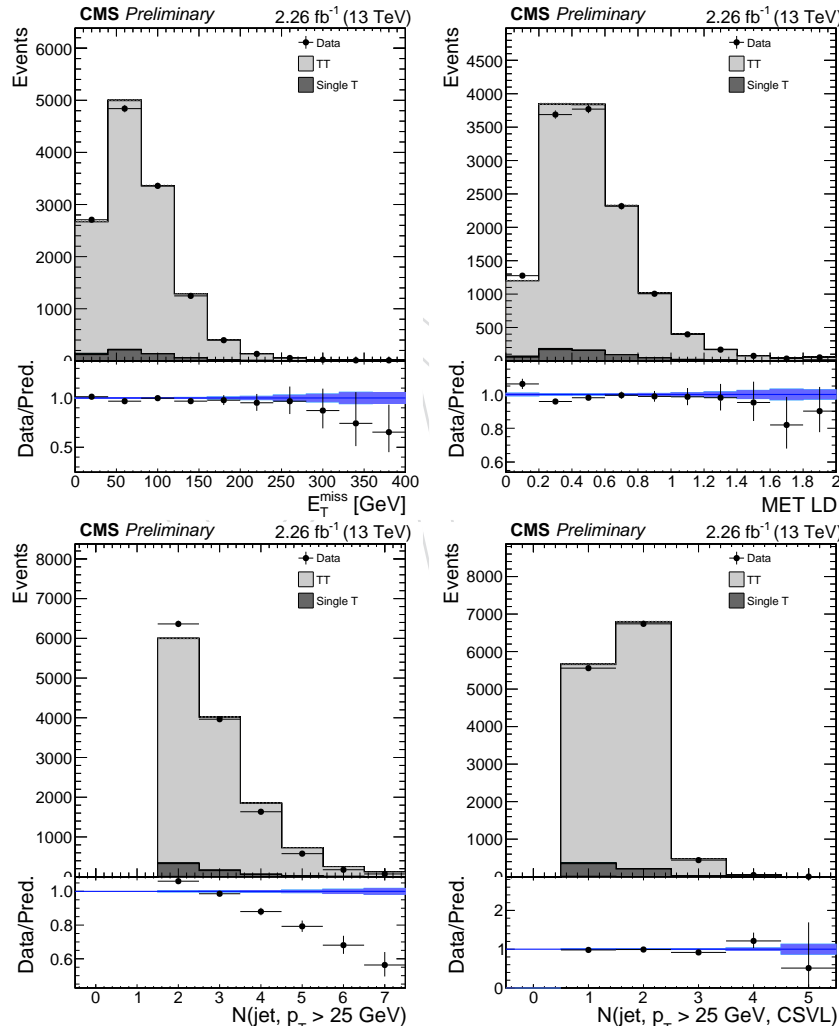


Figure 83: Data and simulation distributions in the  $t\bar{t} \rightarrow e^\pm \mu^\mp b\bar{b} \nu\bar{\nu}$  control region. From top left to bottom right: the  $E_T^{\text{miss}}$ , the  $E_T^{\text{miss}} \text{LD}$ , the jet multiplicity and the number of jets passing the loose working point of the CSV tagger. Uncertainties are statistical only.

<sup>2</sup>The disagreement observed especially in the distribution of the jet multiplicity is under investigation.

#### 891 A.4 $WZ \rightarrow 3\ell$

892 With this control region we want to validate our objects (signal leptons,  $E_T^{miss} LD$ , jets) in the  
 893 three lepton final state. A sample enriched in  $WZ \rightarrow 3\ell$  events is selected modifying the 31  
 894 selection in the following way:

- 895 • the Z veto is inverted, i.e. we require the presence of a pair of loose opposite-sign  
 896 same-flavor leptons whose invariant mass is within 10 GeV from the nominal Z bo-  
 897 son mass;
  - 898 • we require that no selected jets satisfy the medium working point of the CSV b-  
 899 tagging discriminator
- 900 No efficiency scale factors are applied. Some distributions are shown in Fig. 84.

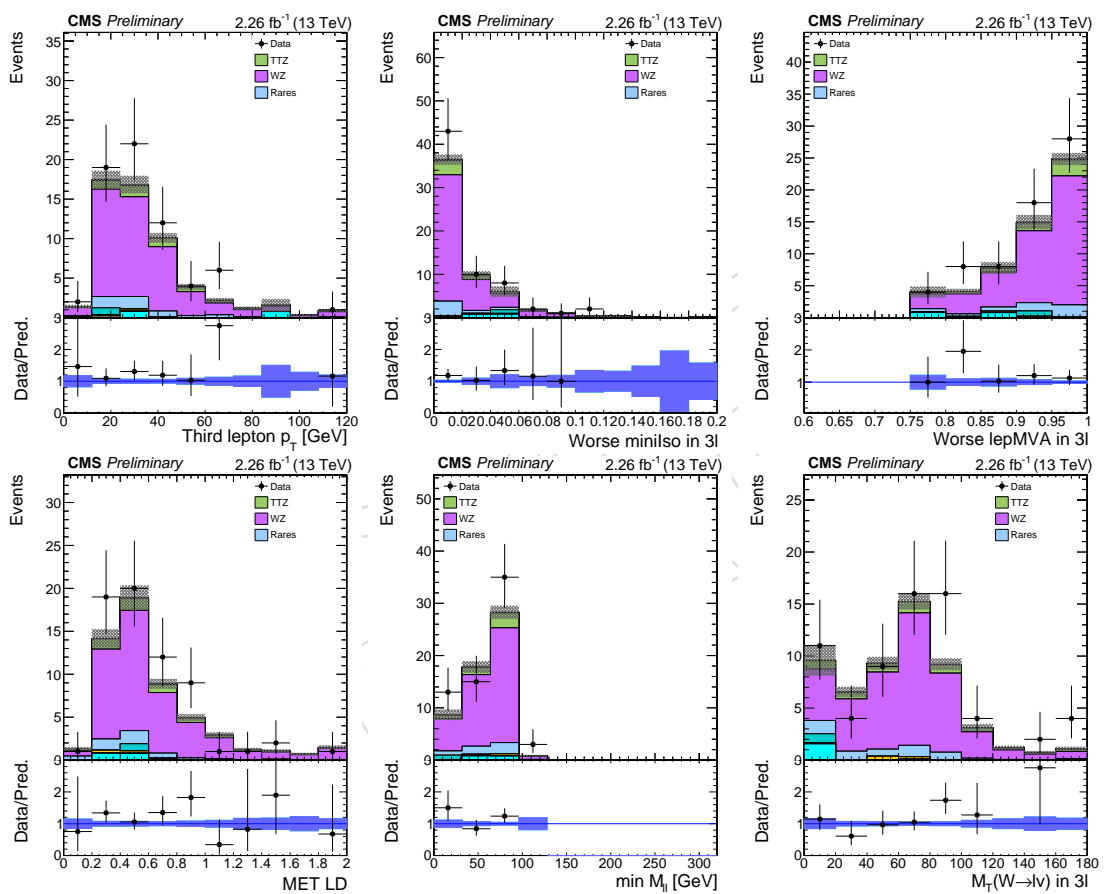


Figure 84: Data and simulation distributions in the  $WZ \rightarrow 3\ell$  control region. From top left to bottom right: the  $p_T$  of the trailing lepton, mini isolation for the worse isolated lepton, worse lepton MVA value, the  $E_T^{miss} LD$ , the minimum invariant mass of any  $\ell\ell$  couples,  $M_T$  of the W boson candidate.

### 901 A.5 $t\bar{t}Z \rightarrow 3\ell$

902 The prediction for the  $t\bar{t}Z$  process is tested directly in a trilepton control region requiring two  
 903 of the leptons to have the same flavour, opposite electrical charge and the invariant mass pair  
 904 of the pair to be within 10 GeV of the nominal Z boson mass.

905 The definition of the control region differs from the one used for the 3l category of the analysis  
 906 in the following points:

- 907 • the Z veto requirement is inverted, as described above;
- 908 • the cut on the multiplicity b-tagged jets is tightened, requiring at least two loose and  
 909 one medium b-tagged jets

910 No efficiency scale factors are applied. The background from non-prompt leptons is estimated  
 911 from data. Some distributions are shown in Fig. 85.

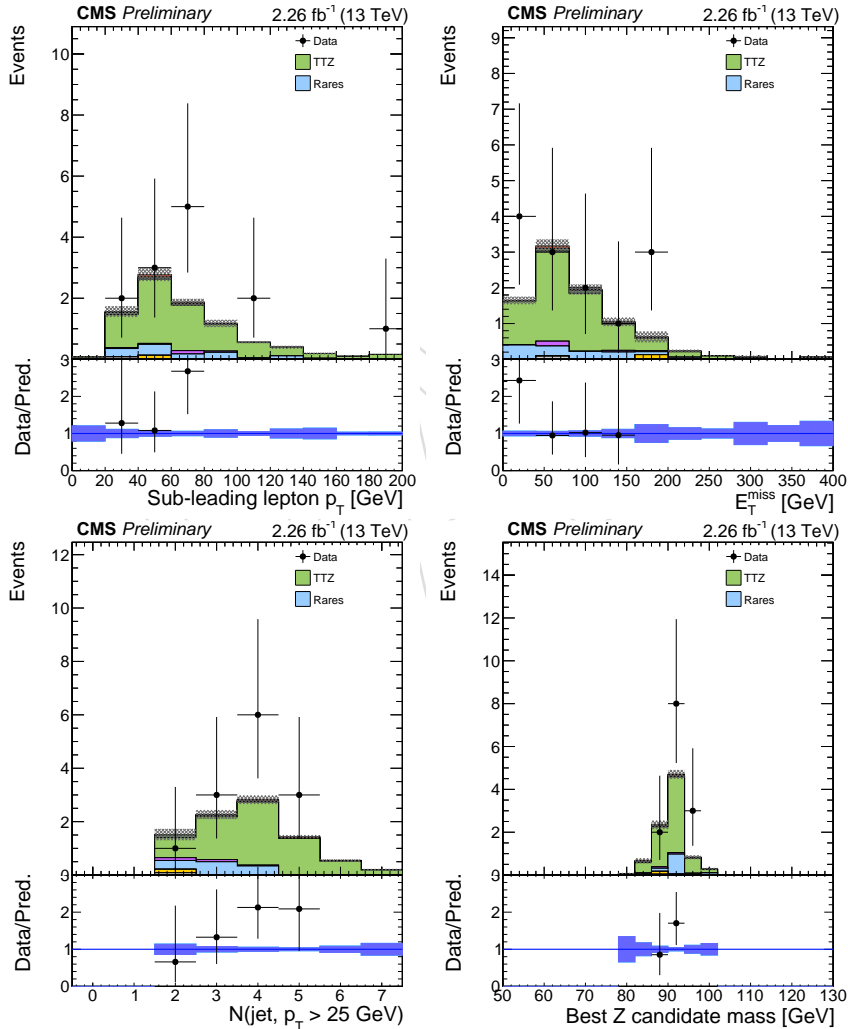


Figure 85: Data and simulation distributions in the  $t\bar{t}Z \rightarrow 3\ell$  control region. From left to right: the  $p_T$  distribution of the second lepton ordered in  $p_T$ , the  $E_T^{\text{miss}}$ , the number of central jets with  $p_T > 25$  GeV, the invariant mass of the best Z candidate.

912 When requiring also the presence of at least four selected jets, as expected for a fully recon-  
 913 structed  $t\bar{t}Z$  event, the control region becomes more pure in selecting  $t\bar{t}Z$  events. This can  
 914 be seen in the distributions in Fig. 86.

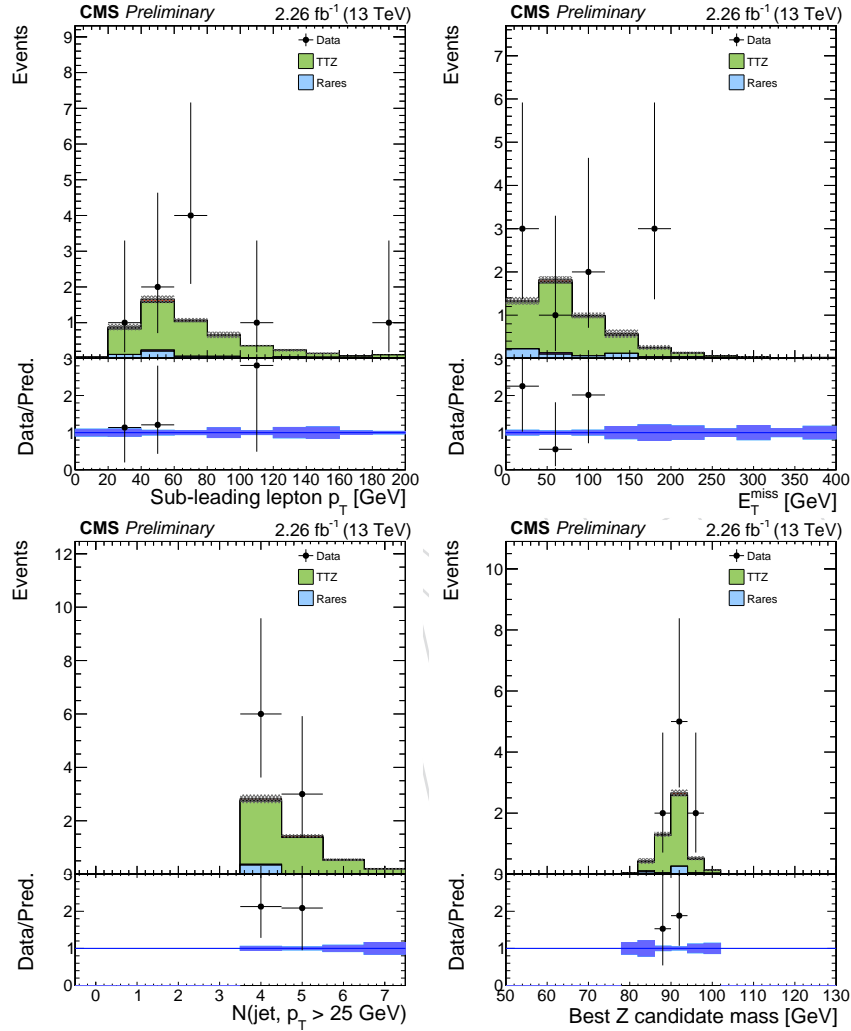


Figure 86: Data and simulation distributions in the  $t\bar{t}Z \rightarrow 3\ell$  control region, with the additional requirement of at least four reconstructed jets. From left to right: the  $p_T$  distribution of the second lepton ordered in  $p_T$ , the  $E_T^{\text{miss}}$ , the number of central jets with  $p_T > 25$  GeV, the invariant mass of the best Z candidate.

## 915 B Post-fit distributions

916 We compare the distributions of the binned kinematic discriminators for the following choice  
 917 of nuisance parameters:

- 918 • Left: pre-fit;
- 919 • Center: post-fit, under the hypothesis of background plus SM signal ( $\mu = 1$ );
- 920 • Right: post-fit, with floating signal strength modifier.

### 921 2lss

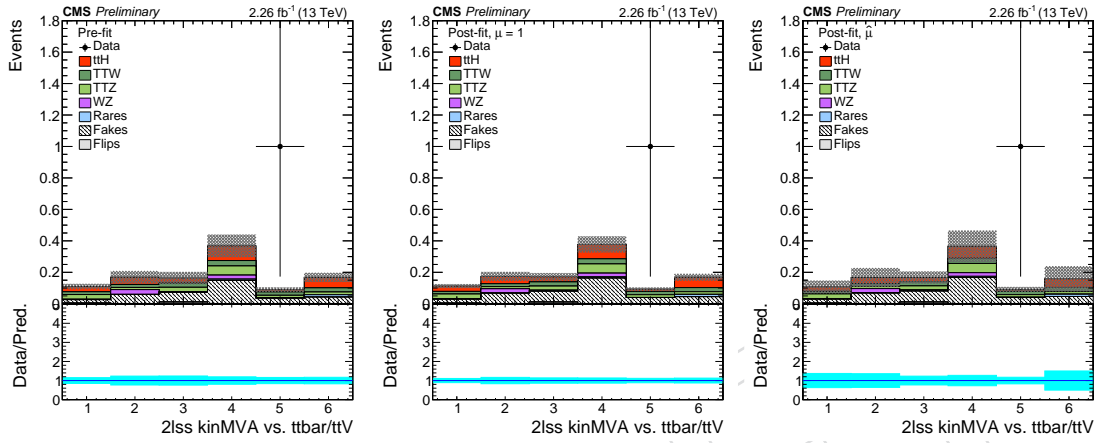


Figure 87: Comparison of data and background distributions with pre-fit, post-fit with fixed  $\mu = 1$ , and post-fit with freely floating  $\mu$  in category 2lss\_1tau. The uncertainties are obtained by sampling the full covariance matrix of the fit.

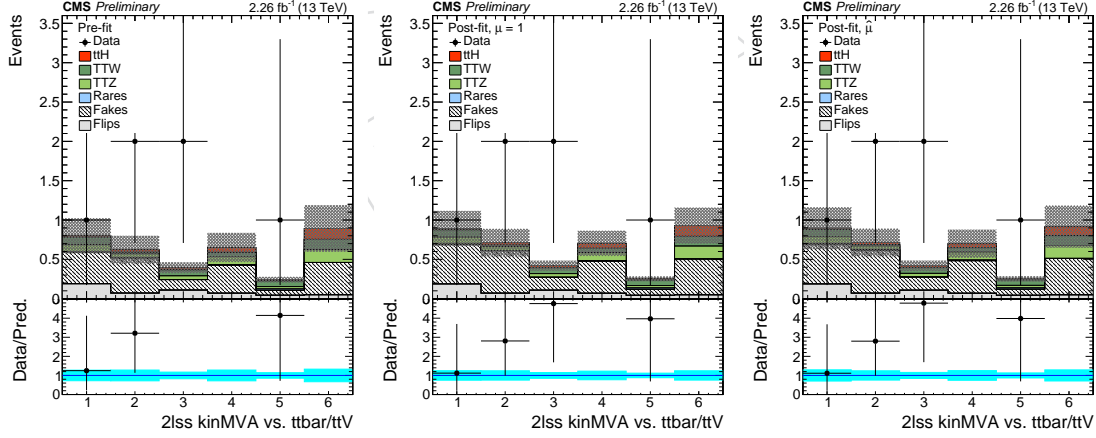


Figure 88: Comparison of data and background distributions with pre-fit, post-fit with fixed  $\mu = 1$ , and post-fit with freely floating  $\mu$  in category 2lss\_ee\_0tau\_neg. The uncertainties are obtained by sampling the full covariance matrix of the fit.

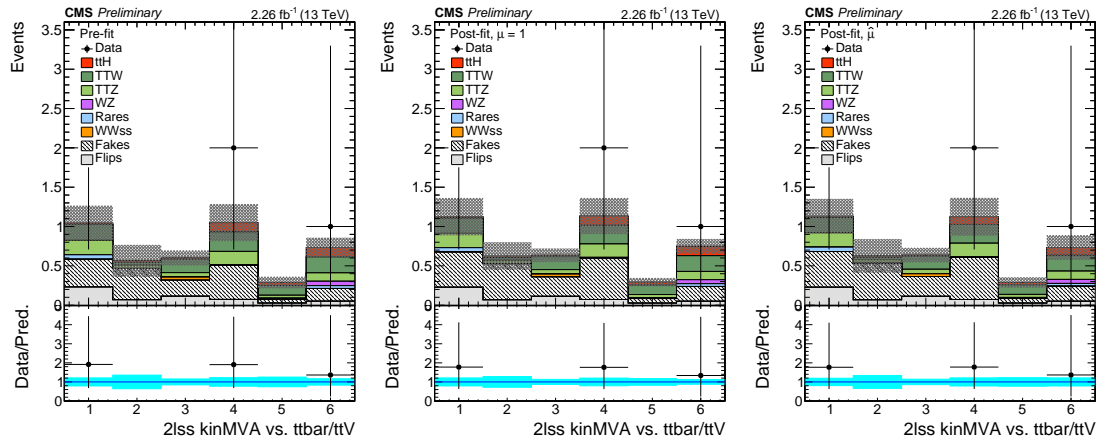


Figure 89: Comparison of data and background distributions with pre-fit, post-fit with fixed  $\mu = 1$ , and post-fit with freely floating  $\mu$  in category 2lss\_ee\_0tau\_pos. The uncertainties are obtained by sampling the full covariance matrix of the fit.

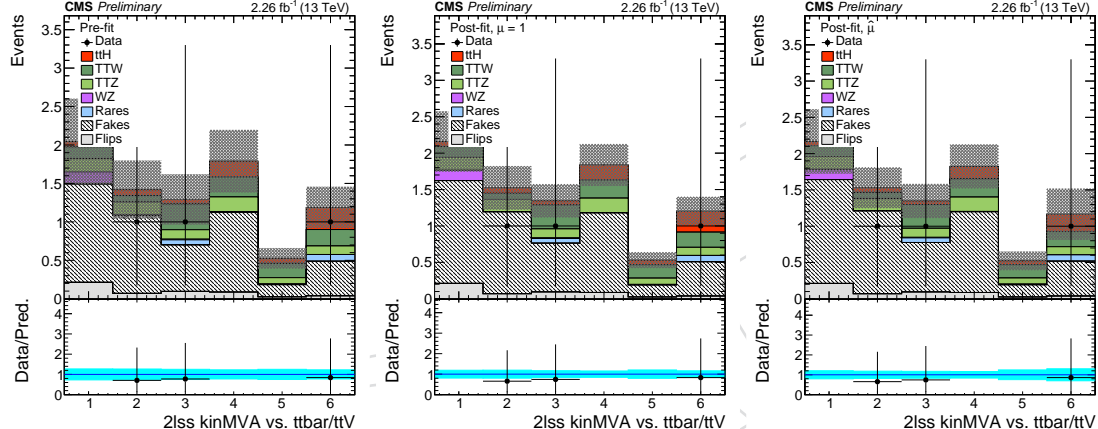


Figure 90: Comparison of data and background distributions with pre-fit, post-fit with fixed  $\mu = 1$ , and post-fit with freely floating  $\mu$  in category 2lss\_em\_0tau\_bl\_neg. The uncertainties are obtained by sampling the full covariance matrix of the fit.

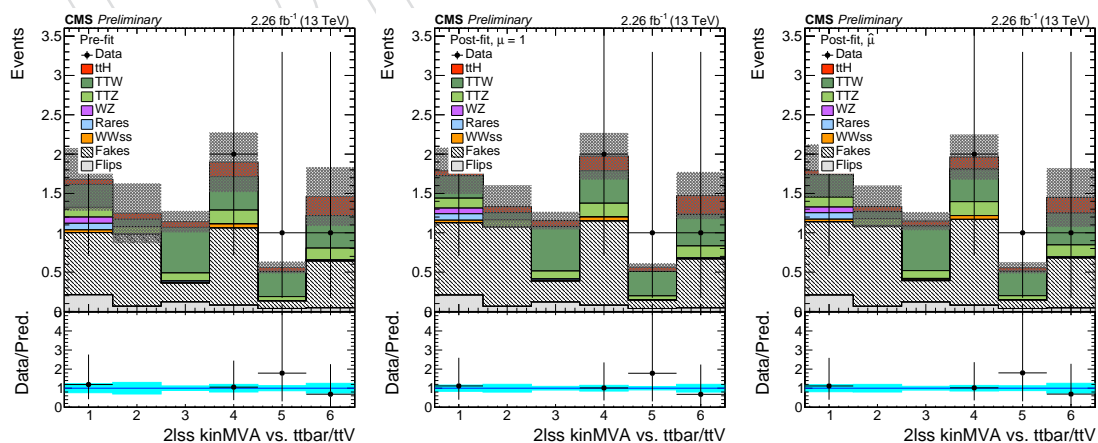


Figure 91: Comparison of data and background distributions with pre-fit, post-fit with fixed  $\mu = 1$ , and post-fit with freely floating  $\mu$  in category 2lss\_em\_0tau\_bl\_pos. The uncertainties are obtained by sampling the full covariance matrix of the fit.

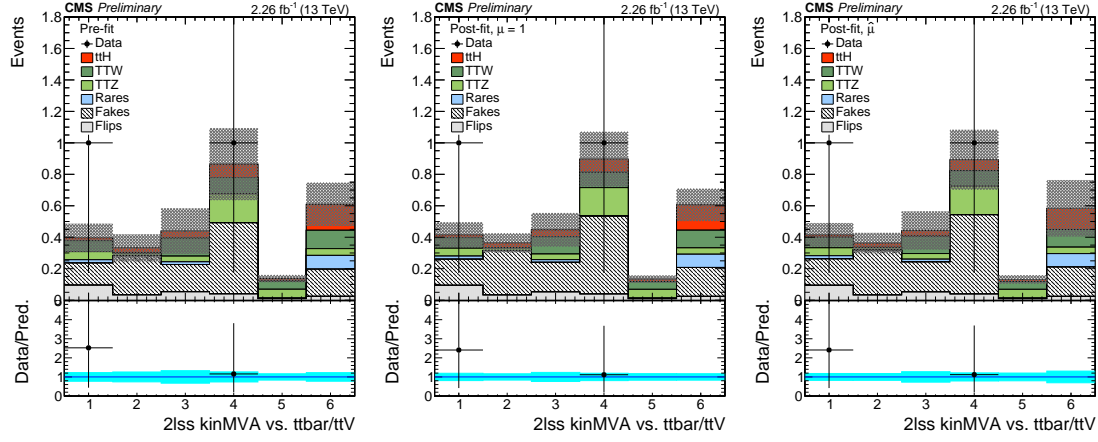


Figure 92: Comparison of data and background distributions with pre-fit, post-fit with fixed  $\mu = 1$ , and post-fit with freely floating  $\mu$  in category 2lss\_em\_0tau\_bt\_neg. The uncertainties are obtained by sampling the full covariance matrix of the fit.

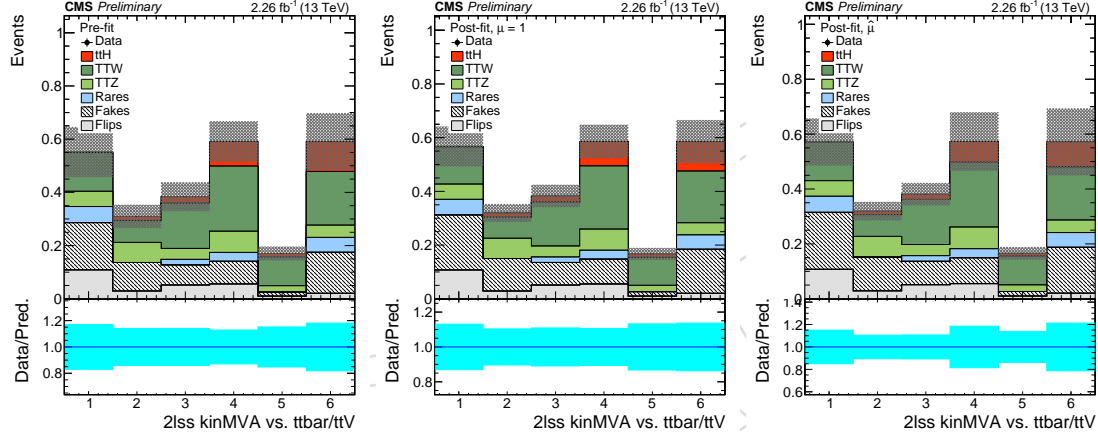


Figure 93: Comparison of data and background distributions with pre-fit, post-fit with fixed  $\mu = 1$ , and post-fit with freely floating  $\mu$  in category 2lss\_em\_0tau\_bt\_pos. The uncertainties are obtained by sampling the full covariance matrix of the fit.

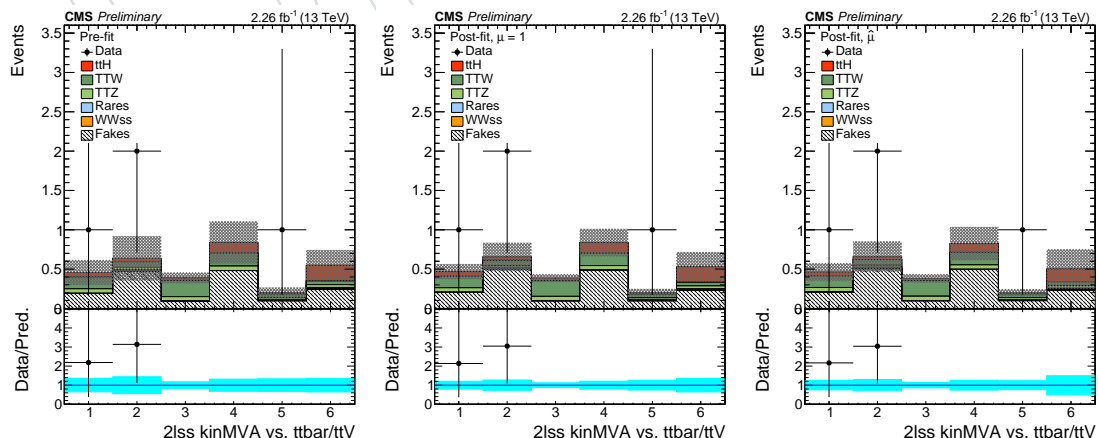


Figure 94: Comparison of data and background distributions with pre-fit, post-fit with fixed  $\mu = 1$ , and post-fit with freely floating  $\mu$  in category 2lss\_mm\_0tau\_bt\_neg. The uncertainties are obtained by sampling the full covariance matrix of the fit.

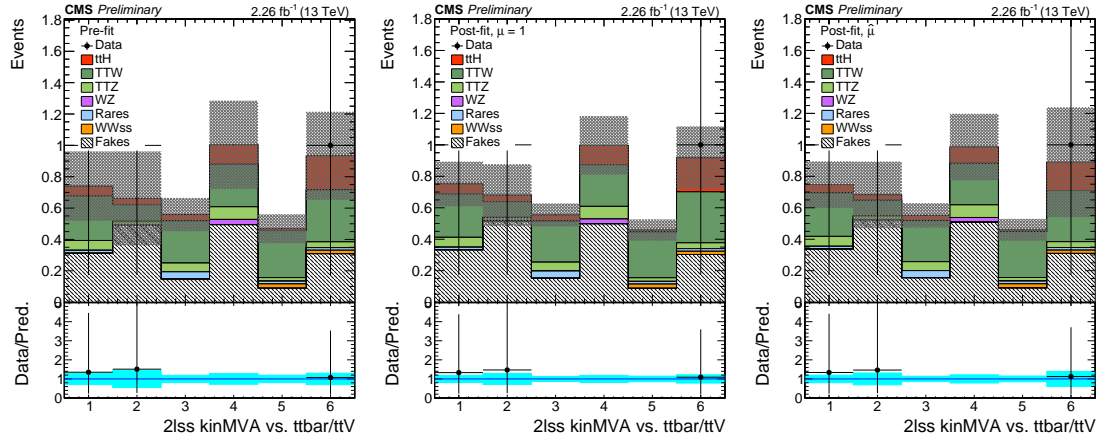


Figure 95: Comparison of data and background distributions with pre-fit, post-fit with fixed  $\mu = 1$ , and post-fit with freely floating  $\mu$  in category 2lss\_mm\_0tau\_bt\_pos. The uncertainties are obtained by sampling the full covariance matrix of the fit.

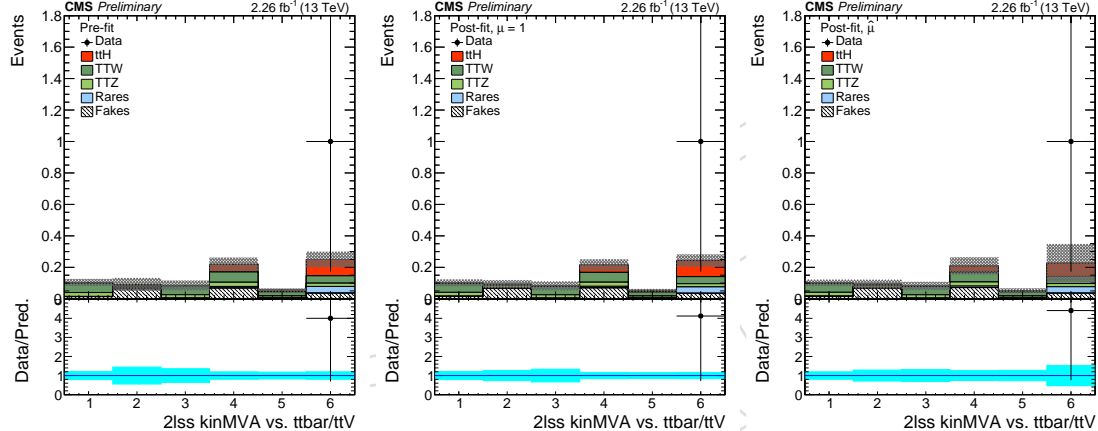


Figure 96: Comparison of data and background distributions with pre-fit, post-fit with fixed  $\mu = 1$ , and post-fit with freely floating  $\mu$  in category 2lss\_mm\_0tau\_bt\_neg. The uncertainties are obtained by sampling the full covariance matrix of the fit.

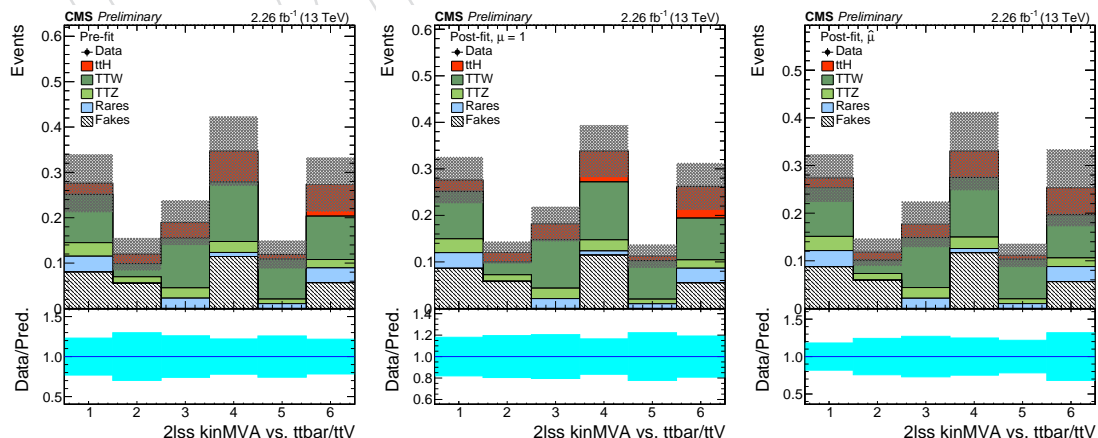


Figure 97: Comparison of data and background distributions with pre-fit, post-fit with fixed  $\mu = 1$ , and post-fit with freely floating  $\mu$  in category 2lss\_mm\_0tau\_bt\_pos. The uncertainties are obtained by sampling the full covariance matrix of the fit.

922 3I

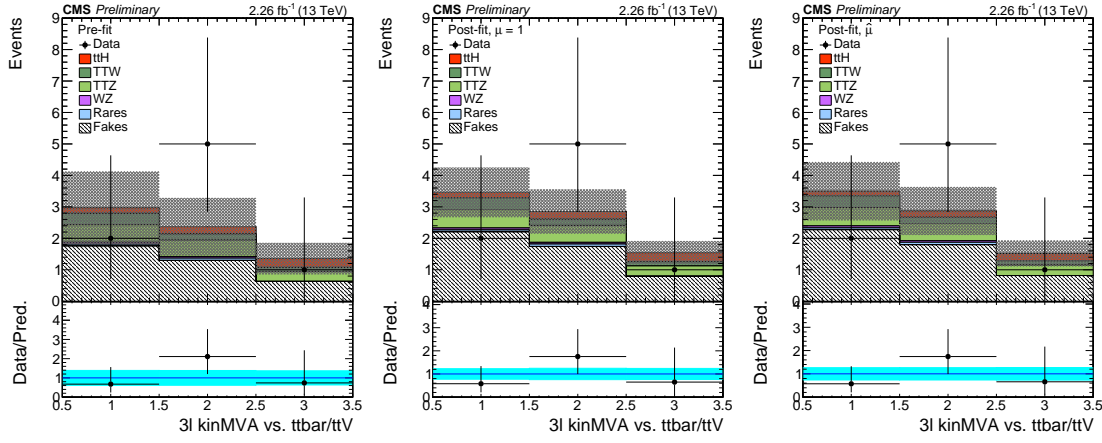


Figure 98: Comparison of data and background distributions with pre-fit, post-fit with fixed  $\mu = 1$ , and post-fit with freely floating  $\mu$  in category 3l.bl.neg. The uncertainties are obtained by sampling the full covariance matrix of the fit.

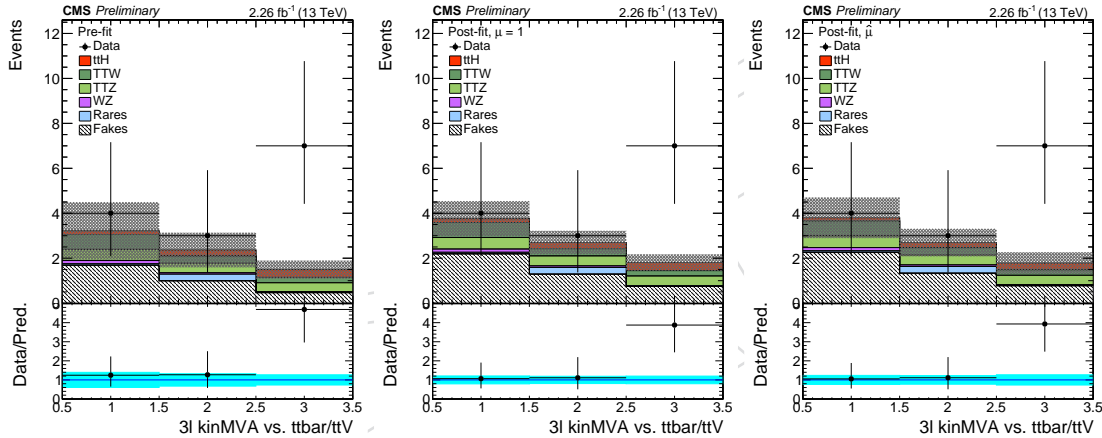


Figure 99: Comparison of data and background distributions with pre-fit, post-fit with fixed  $\mu = 1$ , and post-fit with freely floating  $\mu$  in category 3l.bl.pos. The uncertainties are obtained by sampling the full covariance matrix of the fit.

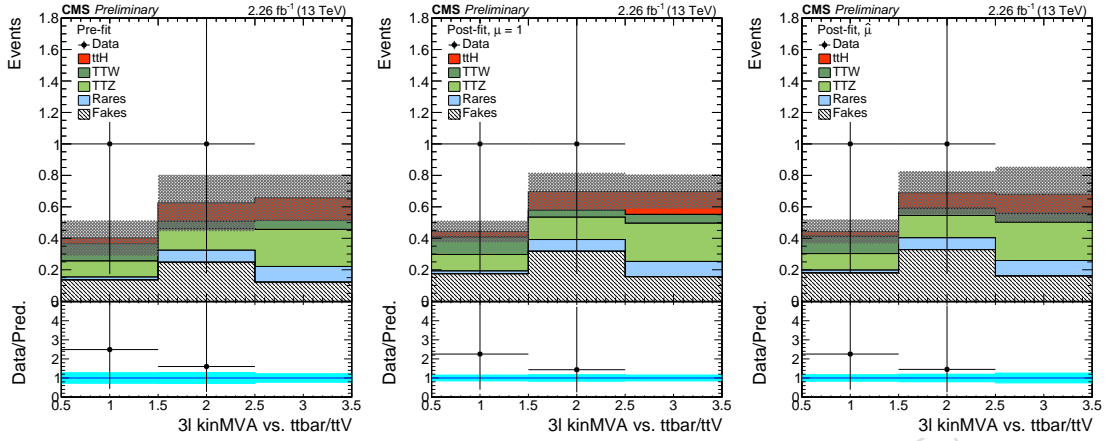


Figure 100: Comparison of data and background distributions with pre-fit, post-fit with fixed  $\mu = 1$ , and post-fit with freely floating  $\mu$  in category 3l\_bt\_neg. The uncertainties are obtained by sampling the full covariance matrix of the fit.

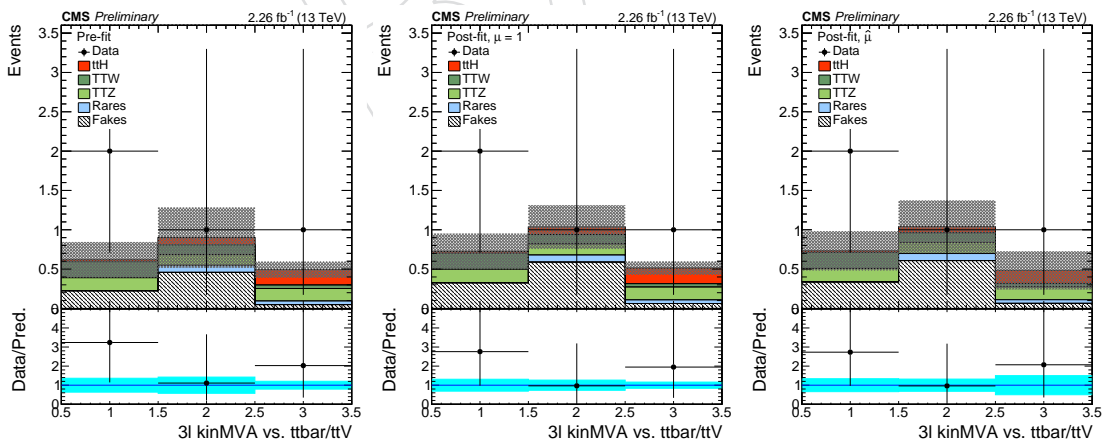


Figure 101: Comparison of data and background distributions with pre-fit, post-fit with fixed  $\mu = 1$ , and post-fit with freely floating  $\mu$  in category 3l\_bt\_pos. The uncertainties are obtained by sampling the full covariance matrix of the fit.

923 **C Cross checks on the fit**

924 **C.1 Alternative fit: separately for 2lss and 3l**

925 Results of fits performed separately in the 2lss or 3l categories are reported in the following.

926 **2lss**

| Category       | Observed              | Expected $\pm 1\sigma$ |
|----------------|-----------------------|------------------------|
| 95% CL limit   | 2.3                   | 2.8 (+1.4) (-0.9)      |
| best fit $\mu$ | -0.41 (+1.05) (-0.75) |                        |

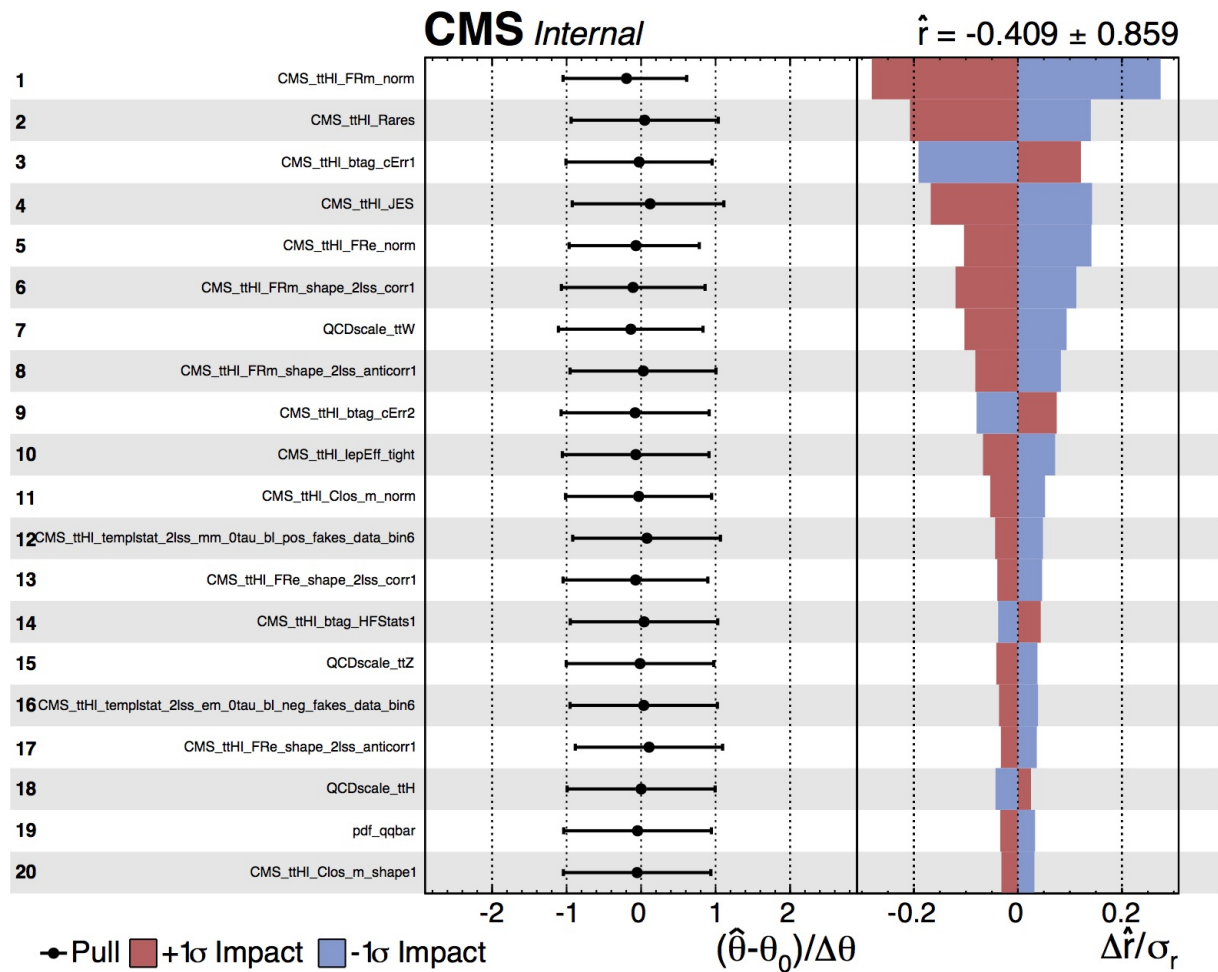


Figure 102: Impact plot showing the correlation between the most important nuisances and the best fit signal strength for the 2lss-only fit.

928 **3l**

929

| Category       | Observed             | Expected $\pm 1\sigma$ |
|----------------|----------------------|------------------------|
| 95% CL limit   | 12.1                 | 5.5 (+3.0) (-1.8)      |
| best fit $\mu$ | 6.05 (+3.36) (-2.75) |                        |

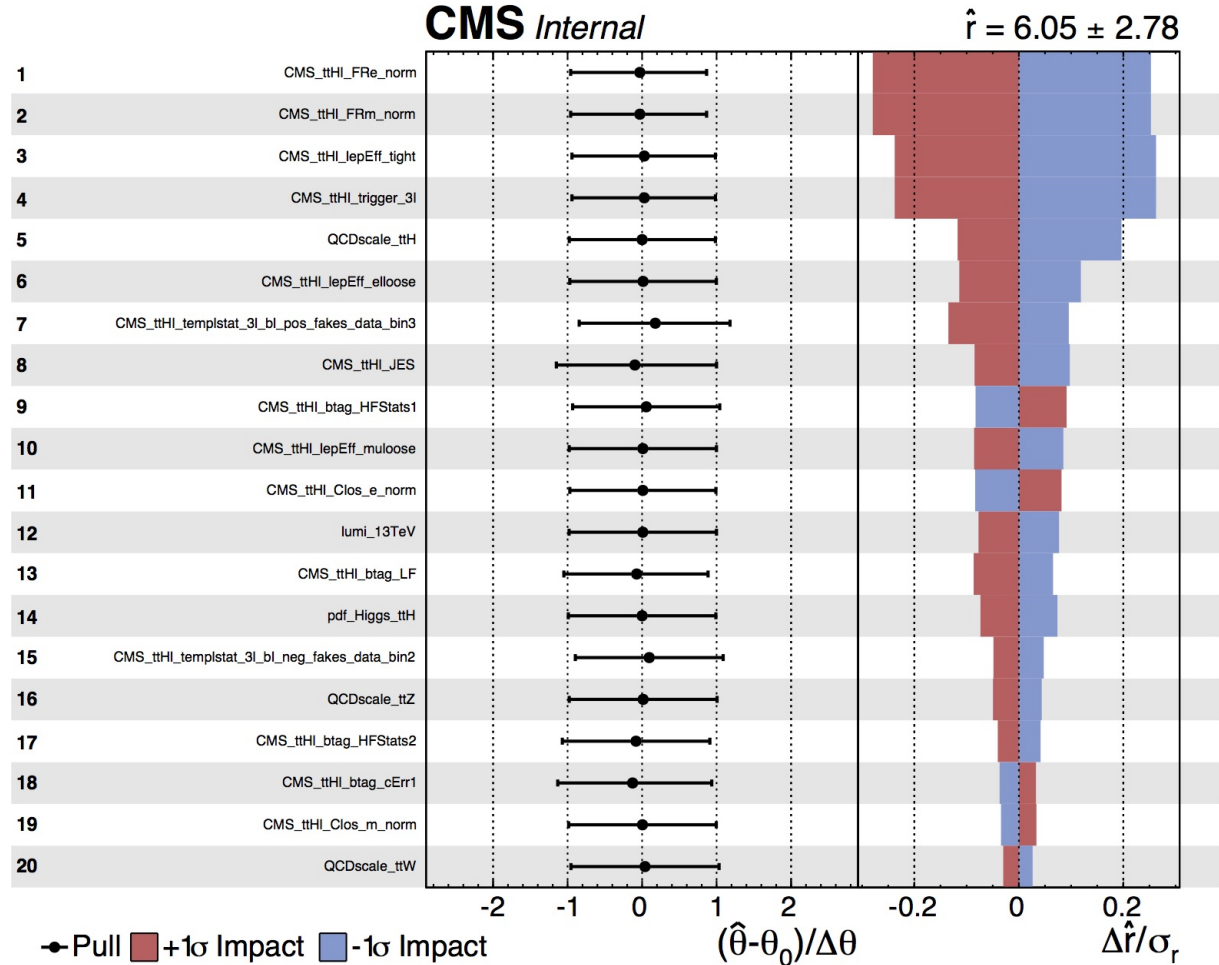


Figure 103: Impact plot showing the correlation between the most important nuisances and the best fit signal strength for the 3l-only fit.

## 930 References

- [1] CMS Collaboration, "Observation of a new boson at a mass of 125 GeV with the CMS experiment at the LHC", *Phys. Lett. B* **716** (2012) 30, doi:10.1016/j.physletb.2012.08.021.
- [2] ATLAS Collaboration, "Observation of a new particle in the search for the Standard Model Higgs boson with the ATLAS detector at the LHC", *Phys. Lett. B* **716** (2012) 1, doi:10.1016/j.physletb.2012.08.020.
- [3] ATLAS and CMS Collaboration, "Combined measurement of the Higgs boson mass in pp collisions at  $\sqrt{7}$  and 8 TeV with the ATLAS and CMS experiments", *Phys. Rev. Letter* **114** (2015) 45, doi:<http://dx.doi.org/10.1103/PhysRevLett.114.191803>.
- [4] ATLAS and CMS Collaboration, "Combined measurement of the Higgs boson mass in pp collisions at  $\sqrt{7}$  and 8 TeV with the ATLAS and CMS experiments", *Eur. Phys. J. C* **76** (2015) 64, doi:10.1140/epjc/s10052-015-3769-y.
- [5] CMS Collaboration, "Precise determination of the mass of the Higgs boson and tests of compatibility of its couplings with the standard model predictions using proton collisions at 7 and 8 TeV", *Eur. Phys. J. C* **75** (2015) 212, doi:10.1140/epjc/s10052-015-3351-7.
- [6] LHC Higgs Cross Section Working Group et al., "Handbook of LHC Higgs Cross Sections: 1. Inclusive Observables", CERN-2011-002 (CERN, Geneva, 2011) arXiv:1101.0593.
- [7] CMS Collaboration, "Search for the associated production of the Higgs boson with a top-quark pair", *JHEP* **09** (2015) doi:10.1007/JHEP09(2014)087.
- [8] CMS Collaboration, "Search for the SM Higgs boson produced in association with top quarks in multilepton final states", CMS Physics Analysis Summary CMS-PAS-HIG-13-020, 2013.
- [9] C. Collaboration, "JSON files for 25ns data (CMS Hypernews)", 2015. <https://hypernews.cern.ch/HyperNews/CMS/get/physics-validation/2577.html>.
- [10] C. Collaboration, "PdmV 2015 Analysis Recipes". <https://twiki.cern.ch/twiki/bin/view/CMS/PdmV2015Analysis>.
- [11] J. Alwall et al., "The automated computation of tree-level and next-to-leading order differential cross sections, and their matching to parton shower simulations", 2014. arXiv:1405.0301.
- [12] T. Sjöstrand, S. Mrenna, and P. Skands, "A brief introduction to PYTHIA 8.1", *Comp. Phys. Comm.* **178** (2008) 852, doi:10.1016/j.cpc.2008.01.036, arXiv:0710.3820.
- [13] S. Alioli, P. Nason, C. Oleari, and E. Re, "A general framework for implementing NLO calculations in shower Monte Carlo programs: the POWHEG BOX", *JHEP* **06** (2010) 043, doi:10.1007/JHEP06(2010)043, arXiv:1002.2581.
- [14] CMS Collaboration, "Dilepton trigger and lepton identification efficiencies for the top quark pair production cross section measurement at 8 TeV in the dilepton decay channel.", CMS AN AN-12-389, 2012.

- 971 [15] CMS Collaboration, "Particle-Flow Event Reconstruction in CMS and Performance for  
972 Jets, Taus, and MET", CMS Physics Analysis Summary CMS-PAS-PFT-09-001, 2009.
- 973 [16] CMS Collaboration, "Commissioning of the Particle-Flow reconstruction in  
974 Minimum-Bias and Jet Events from  $pp$  Collisions at 7 TeV", CMS Physics Analysis  
975 Summary CMS-PAS-PFT-10-002, 2010.
- 976 [17] M. Cacciari, G. P. Salam, G. Soyez, "FastJet user manual", (2011).  
977 arXiv:hep-ph/1111.6097v1.
- 978 [18] M. Cacciari, G. P. Salam, "Dispelling the  $N^3$  myth for the  $k_t$  jet-finder", *Phys. Lett. B* **641**  
979 (2006) 57, doi:10.1016/j.physletb.2006.08.037, arXiv:hep-ph/0512210.
- 980 [19] CMS Collaboration, "Determination of Jet Energy Calibration and Transverse Momentum  
981 Resolution in CMS", *JINST* **6** (2011) 11002, doi:10.1088/1748-0221/6/11/P11002.
- 982 [20] CMS Collaboration Collaboration, "Identification of b-quark jets with the CMS  
983 experiment", *JINST* **8** (2013) P04013, doi:10.1088/1748-0221/8/04/P04013,  
984 arXiv:1211.4462.
- 985 [21] CMS Collaboration, "Performance of CMS muon reconstruction in pp collision events at  
986  $\sqrt{s} = 7$  TeV", *JINST* **7** (2012) P10002, doi:10.1088/1748-0221/7/10/P10002,  
987 arXiv:1206.4071.
- 988 [22] G. Abbiendi et al., "Baseline muon selections", October, 2014. [https://twiki.cern.ch/twiki/bin/view/CMS/CMSPublic/SWGuideMuonId#Tight\\_Muon](https://twiki.cern.ch/twiki/bin/view/CMS/CMSPublic/SWGuideMuonId#Tight_Muon).
- 989 [23] G. Petrucciani and C. Botta, "Two step prompt muon identification", January, 2015.  
990 <https://indico.cern.ch/event/368007/contribution/2/material/slides/0.pdf>.
- 991 [24] H. Brun and C. Ochando, "Updated Results on MVA eID with 13 TeV samples", October,  
992 2014. <https://indico.cern.ch/event/367861/contribution/1/material/slides/0.pdf>.
- 993 [25] CMS Collaboration, "Studies of Tracker Material", *CDS Record* **1279138** (2010).
- 994 [26] S. L. S. F. W. Group, "Lepton SF", December, 2015.  
995 <https://twiki.cern.ch/twiki/bin/view/CMS/SUSLeptonSF>.
- 996 [27] CMS Collaboration, "Reconstruction and identification of  $\tau$  lepton decays to hadrons and  
997  $\nu_\tau$  at CMS", arXiv:1510.07488.
- 998 [28] A. Nayak et al., "Multivariate  $\tau$ -identification algorithms for 13 TeV data", CMS Analysis  
999 Note CMS AN-15-310, 2015.
- 1000 [29] Y. R. . in preparation. <http://indico.cern.ch/event/407347/session/3/contribution/10/attachments/1211342/1766869/hxswg16.pdf>.
- 1001 [30] P. production of low  $m_{ll}$  ttZ sample.  
1002 <https://www.dropbox.com/s/fni1334aaa9cbfn/ttzlowmll.pdf?dl=0>.
- 1003 [31] C. Botta et al., "Search for the standard model Higgs boson produced in association with  
1004 top quarks and decaying to leptons", CMS Analysis Note CMS AN-13-159, 2013.